Stability and control of flow past elliptic cylinders

A thesis submitted
in partial fulfillment of the requirements
for the degree of

Doctor of Philosophy

by

Deepak Kumar

Department of Mechanical Engineering
Indian Institute of Technology Guwahati
Guwahati 781039
July 2022

TH-2822_166103027

CERTIFICATE

It is certified that the work contained in the thesis entitled **“ Stability and control of flow past elliptic cylinders”** by Deepak Kumar (Roll No. 166103027), has been carried out under my supervision and that this work has not been submitted elsewhere for a degree.

(Bhaskar Kumar)
Assistant Professor
Department of Mechanical Engineering
Indian Institute of Technology Guwahati

July, 2022

Dedicated to my parents

For their continuous support, patience and endless love.

भारतीय प्रौद्योगिकी संस्थान गुवाहाटी
Indian Institute of Technology Guwahati

Acknowledgements

I would like to express my sincere gratitude to the people who have directly or indirectly supported me in completing this amazing journey. Too many people are worth mentioning, but the first acknowledgement cannot be anyone else but my supervisor, Dr. Bhaskar Kumar. This work would have never been completed without his guidance and continuous support. He provided me with all kinds of facilities required to carry out this work. Whenever I was in doubt or fear of uncertainty, one call from him cleared all my doubts and made me keep going. I feel proud that I am his first PhD student, and I would like to continue working with him after completing my degree. He not just helped me with my research work but also gave me regular advice to keep my health well. I consider myself very fortunate that I have worked with him, and the past years have been a life-changing experience.

Besides my thesis supervisor, I would like to thank my doctoral committee members, Prof. Niranjan Sahoo, Prof. Amaresh Dalal and Prof. Dipankar Bandyopadhyay, for their insightful comments. Their suggestions and encouragement helped me to widen my research from various perspectives.

I would like to show my greatest respect to the late Prof. Subhas Chandra Mishra. He was the first person at IIT Guwahati who sparked a dream in my eye to become a researcher. I still remember all his lessons and work ethics. I will never forget him throughout my life.

I would like to thank NIT Durgapur for providing me with this amazing opportunity to pursue my career in academics. A special thanks goes out to the people of the Mechanical engineering department, NIT Durgapur. Without their support, I could not have completed this work. I am thankful to Dr. Jaydeep Howlader for allowing me to perform some numerical computations on his lab servers at NIT

Durgapur. I express my respect to Prof. Aniruddha Gangopadhyay for his unconditional support. Without the company of Dr. Sujay Saha and Dr. Bhibhas Sen at NIT Durgapur, this journey would have been difficult. They always took care of me like a little brother.

I am thankful to Dr. Hiranya Deka and Wasim Akram for many technical discussions about my work. They helped me a lot throughout this entire journey. I am very much grateful to the Computer & Communication Centre of IIT Guwahati for providing the High-Performance Computing facility. I am thankful to the Department of Mechanical Engineering, IIT Guwahati, for providing me with the required facilities and an excellent working environment. I acknowledge Dr. Prabas Banerjee, Dr. Vinod Pandey, Shatrughan Jaiswal, Ujjawal Chetan, Agneev Roy, and Bhaskar Bhattacharyya for many fruitful discussions and the laughter that we shared together.

I acknowledge my friend, Ankesh Kumar, for his continuous support, both emotionally and financially. He always stood beside me and was one call away whenever I needed his help. Towards the end of my journey at IIT Guwahati, I had a wonderful time with Angan Sarkar, Mukesh Sharma, and Krishan Chand. I am thankful to them for all the laughter we shared. Their presence made my journey worth remembering.

Words cannot express my feelings for my parents for the sacrifice they have made for me. They always showed constant support and love throughout this journey. They are the pillars of my life, and without them, this journey would have never been completed. I express my special thanks to my sisters and cousin brother Arun Kumar for his care and unconditional support in pursuing my PhD. I am also grateful to my relatives for showing their patience and support throughout this journey.

Deepak Kumar

Institute of Technology

ABSTRACT

Linear stability analysis of steady two-dimensional flow past elliptic cylinders of different aspect ratio (Ar) is conducted. Computations are carried out for flow Reynolds number (Re) in the range 30-200. First, the main characteristics of the steady flow, like the bubble length, bubble width, separation Reynolds number, separation angle, drag coefficient, coefficients of the front and rear stagnation pressure, and the maximum vorticity on the cylinder surface have been obtained. Least squares fit equations for some of these quantities have also been presented. In the special case of a circular cylinder, results computed with the largest domain show that the bubble length, bubble width, maximum vorticity on the cylinder surface, coefficients of pressure drag and total drag and the flow separation angle are linear functions of Re, $Re^{0.5}$, $Re^{0.35}$, $Re^{-0.4}$, $Re^{-0.5}$ and $Re^{-0.1}$, respectively. As Ar changes, the trends in the growth, with respect to Re^n (with the corresponding index), for the bubble length, bubble width and the maximum surface vorticity deviate from their linear nature. The effect of blockage on the steady flow characteristics has been studied by varying the location of the side boundaries. In certain cases, the flow properties are found to vary in a nonmonotonic fashion with change in the blockage. An explanation based on the dual role of the side boundaries in promoting and suppressing the growth of the corresponding flow property is offered. From the linear stability calculations, we find that there are three sets of complex eigenmodes which become unstable with increasing Re. We refer to them as primary wake mode (PWM), secondary wake mode (SWM) and tertiary wake mode (TWM), respectively. The critical Re for the onset of instability of these modes and the corresponding Strouhal number (St) have been computed. The effect of blockage on the linear stability results is also studied. Our computations show that the modes which have larger growth rate tend to come close to the cylinder surface and the extent to which they spread downstream in the wake is less compared to the weaker modes. The size of the vortical structures in a mode is inversely related to its *St*. The change in the structure of the modes with the aspect ratio, *Re* and blockage is therefore linked to the corresponding change in their growth rate and *St*. Structural sensitivity analysis is conducted to find the region best suitable for effecting control of the unstable modes. It is shown that the linear stability computations with slip-plate of small size placed at different locations on the centerline is more suited for the present study and gives more information than the sensitivity analysis. We carry out unsteady computations by selectively suppressing one or more linear modes to see the kind of flow which evolves and, as a result, make an attempt to understand the role of the unstable linear modes in the fully developed nonlinear flow.

Keywords:

elliptic cylinder, steady flow, linear stability analysis, structural sensitivity analysis, blockage, slip-plate

Indian Institute of Technology Guwahati

Contents

भारतीय प्रौद्योगिकी संस्थान गुवाहाटी • Indian Institute of Technology Guwahati •

List of Figures


भारतीय प्रौद्योगिकी संस्थान गुवाहाटी
Indian Institute of Technology Guwahati

List of Tables

Nomenclature

English Symbols

$\mathbf{A}$	Non-symmetric matrices
$\mathbf{B}$	Non-symmetric matrices
a	Semi-major axis
b	Semi-minor axis
$\mathbf{f}$	Body force
H	Computational domain half-width
L_u	Computational domain upstream length
L_d	Computational domain downstream length
$\mathbf{n}$	Normal vector
p	Pressure
p'	Perturbation field for pressure
t	Temporal coordinates
$\mathbf{u}$	Velocity
u	Stream-wise velocity
u'	Perturbation field for velocity
U	Free stream velocity
v	Cross-stream velocity
x, y	Spatial coordinates

Greek Symbols

$\mathit{\Gamma}$	Finite element boundary
λ	Eigenvalue
μ	Dynamic viscosity
ν	Kinematic viscosity
ρ	Density of fluid
$\boldsymbol{\sigma}$	Stress tensor
τ	non-dimensionalized time
$\mathit{\Omega}$	Finite element domain
θ_s	Separation angle
ω_{max}	Maximum vorticity on the surface of the cylinder

Abbreviations

Ar	Aspect ratio
C_{Dp}	Pressure drag coefficient
C_{Df}	Skin friction drag coefficient
C_D	Total Drag coefficient
C_p	Pressure coefficient
C_{p0}	Front stagnation pressure
C_{pb}	Rear stagnation pressure
L_B	Bubble length
Re	Reynolds number
Re_S	Separation Reynolds number
St	Strouhal number
W_B	Bubble width

Acronyms

PWM	Primary wake mode
SWM	Secondary wake mode
TWM	Tertiary wake mode
FEM	Finite element method
LSA	Linear stability analysis
PSPG	Pressure-stabilizing/ Petrov-Galerkin
SUPG	Streamline-upwind/ Petrov-Galerkin
FFT	Fast Fourier Transform
LE	Leading edge
TE	Trailing edge

Subscripts

sd	space dimension
r	real parts
i	imaginary parts
el	number of elements

Superscripts

e	element

Indian Institute of Technology Guwahati

Chapter 1

Introduction

When a fluid flows past a stationary body or, equivalently, when a body moves in a fluid at rest, a region of disturbed flow is formed around the body. The extent of the disturbed flow largely depends on the shape, orientation and size of the body, as well as, the velocity and the viscosity of the fluid, and may be influenced by a wide variety of small disturbances. The practical engineering applications of flow past bluff bodies like heat exchanger tubes, risers in marine technology, road vehicles, buildings, naval applications, and bridges motivate researchers to study the phenomena of flow separation and vortex shedding. The most critical consequence of massive flow separation behind a bluff body is the dramatic increase of the drag force due to the low base pressure. In addition, the oscillations in the wake of bluff bodies induce structural vibrations which cause early deterioration of the materials and sometimes structural failure. These oscillations also produce acoustic noise and enhance the mixing. An understanding of the flow instabilities leading to wake oscillations and their control is of fundamental importance in gaining insights into the cause of such phenomenon and also in applications demanding robust and durable structural design. In what follows, we present a brief outline of the related topics.

1.1 Bluff body flows

Flow past a bluff body is generally associated with flow separation due to its shape and orientation with respect to the incoming free stream. The extent to which a body behaves like a bluff body depends on the comparative strength of the pressure

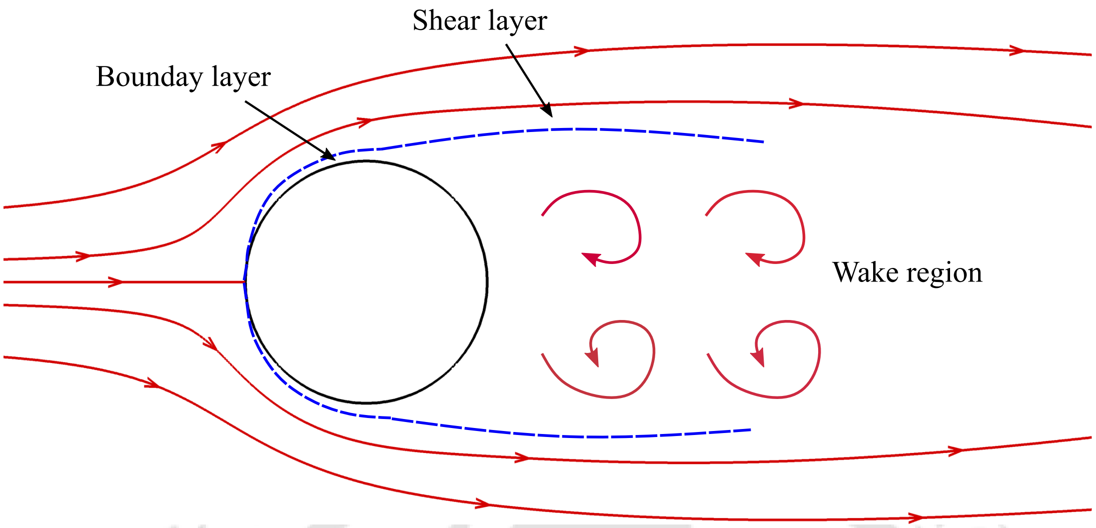

Figure 1.1: A schematic representation of the streamlines in flow past a circular cylinder.

drag and the skin friction drag. If there is a significant contribution of the pressure drag to the total drag acting on the body then we call the body as a bluff body. In general, bluff body wakes exhibit complex flow features. Figure 1.1 shows a schematic diagram of the streamlines in flow past a circular cylinder. The region of the boundary layer, the shear layer and the wake can be seen. As the Reynolds number (Re) is increased, the flow dynamics becomes more and more complex.

Flow past a circular cylinder is the most studied among the family of bluff body flows. Generally, phenomena appearing in a bluff body wake are also seen in the case of flow past a circular cylinder. However, there are engineering applications involving flow past a body like a wing, a rotor blade, a submarine, a missile, etc, which can hardly be modelled as flow past a circular cylinder. They can be better represented as flow past an elliptic cylinder. Also, these days, designers prefer elliptical pillars over circular pillars to support bridges. The aerodynamic forces generated when the wind blows past these structures are of significant concern during their design. Flow past an elliptic cylinder is characterized by an additional parameter, the aspect ratio (Ar), apart from Re. In this thesis, we conduct an elaborate study of the steady and unsteady laminar flow past elliptic cylinders. We investigate the various vortex shedding patterns obtained with cylinders of different Ar and Re.

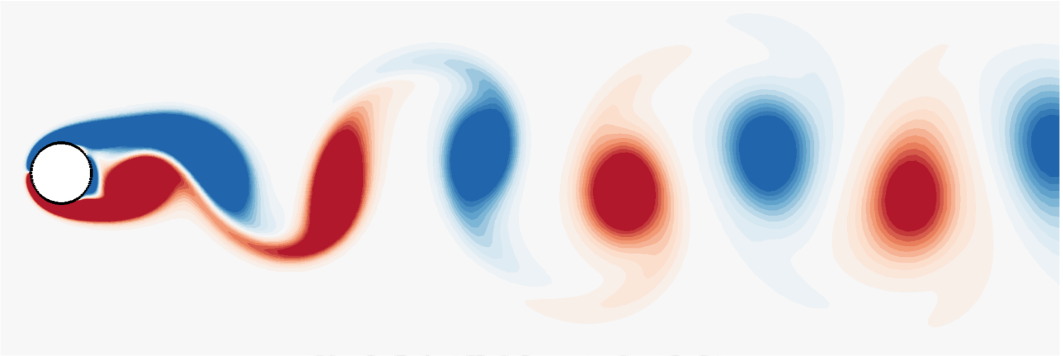

Figure 1.2: von Kármán vortex shedding for flow past a circular cylinder at $Re = 150$.

1.2 Vortex shedding

Vortex shedding is one of the important features of bluff body flows. Figure 1.2 shows the example of vortex shedding for flow past a circular cylinder at $Re = 150$. In this flow, eddies are generated alternately from the rear side of the upper and the lower surface of the body. The eddies form low-pressure zones, which create a pressure gradient to accelerate the fluid, thereby producing oscillatory force on the body. The oscillations generally occur at a specific frequency. Resonance occurs if the oscillation frequency coincides with the natural frequency of the structure. In the resonance condition, the oscillations can damage tall and uniform structures, and sometimes lead to fatigue failures. One such example of the failure is the collapse of the original Tacoma Narrows suspension bridge in 1940. Since the Tacoma incident, the analysis of vortex shedding and its effect on the structure has become a major research topic. However, later, it was found that the bridge failed by aeroelastic flutter. Recently, the collapse of one of the three towers of a thrill ride, ”VertiGo,” at Cedar Point in Sandusky, Ohio, during the winter of 2001 is an example of vortex shedding failure.

1.3 Flow past an elliptic cylinder

Flow past an elliptic cylinder is the generalization of flow past a circular cylinder which involves a new variable: the aspect ratio. The dynamics of the wake of an elliptic cylinder is much more rich compared to the same for a circular cylinder.

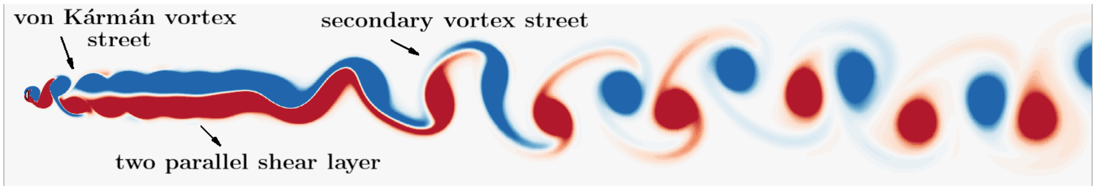

Figure 1.3: Flow past an elliptic cylinder (major axis normal to the incoming stream) with $Ar = 0.25$ and $Re = 150$: presence of a near wake von Kármán vortex street, two parallel shear layers and the secondary vortex street can be clearly seen.

As we change the aspect ratio of the cylinder, the flow becomes more and more complex. For example, flow past an elliptic cylinder is characterized by the presence of a near wake vortex street (von Kármán vortex street) followed by the diffusion of vortices to form two parallel shear layers (see figure 1.3). The oscillations in the shear layers become stronger in the downstream direction and eventually lead to the formation of the secondary vortex street. With a decrease in aspect ratio, the extent of the von Kármán vortex street reduces in the wake and the onset location of the secondary vortex street moves close to the cylinder. For low aspect ratios, the shedding pattern is much more complex and chaotic with the appearance of vortex paring and long wavelength wake oscillations (Thompson *et al.* [4]).

1.4 Stability of fluid motion

Fluid systems are often characterized and described by their stability properties. It is known that smooth laminar flows are stable to small disturbance only when certain conditions are satisfied. For example, in the flow of homogeneous viscous fluids in a channel, Re must be less than some critical value. When these conditions are not satisfied, infinitesimal disturbance grows spontaneously. Sometimes the disturbance can increase to a finite amplitude and reach equilibrium, resulting in a new steady/oscillatory state. The new state may then become unstable to other types of disturbances and may grow to yet another steady/oscillatory state, and so on. Finally, the flow becomes a superposition of various disturbances of random phases, and reaches a chaotic condition that is commonly described as "turbulent". Osborne Reynolds was the first to present the notion of hydrodynamic stability in 1883 through a pipe flow experiment.

To introduce the notion of stability, first, an equilibrium state has to be defined. Equilibrium state of a system refers to the state which is independent of time. For example, steady flow in a pipe, steady flow past a circular cylinder, etc. In general, a system can have multiple equilibrium states. Sometimes, one may conduct stability of a time varying state of a system. In this case we refer to the state as a base state. To check the stability characteristics of a state, we perturb the state. If the system returns to the original state, i.e., if the perturbation decays, the state is termed as stable. Here, we should note that only if all possible perturbations decay with time, the state is a stable state of the system. On the other hand, even if there exists a single perturbation which takes the system away from the original state, the state is regarded as unstable. Though there are several different theories available using which one can investigate the stability of fluid flows, one can categorise them into two groups: linear (stability) theory and the nonlinear theory. Linear stability theory investigates the stability of a system to infinitesimal perturbations, whereas the nonlinear theory investigates the response to finite perturbations. There are further subcategories depending on the approach adopted. We will not dwell here into exploring this vast territory. For bluff body flows, linear stability analysis has been quite successful in helping us gain an understanding the flow behaviour. In the present work, we use the linear stability theory for investigating the flow phenomenon.

1.5 Linear stability analysis

Linear stability analysis generally follows the approach of normal mode analysis. First, we find the base state whose stability is in question. In the present work, the base state is always a steady flow. We determine this by solving the time independent form of the Navier-Stokes equations. The governing equation of the fluid flow is nonlinear. Therefore, the perturbation equation obtained by subtracting the steady flow equation from the unsteady flow equation is also nonlinear. Assuming the perturbations to be infinitesimal, we drop the nonlinear term from the perturbation equation to obtain the linearized perturbation equation. Generally, the boundary conditions are homogeneous. So, we adopt the method of separation of variables to arrive at an eigenvalue problem. The solution to the eigenvalue problem gives a set of eigenvalues and the corresponding eigenvectors. In general, the eigenvalues and the eigenvectors are complex. The real part of an eigenvalue represents the growth rate of the corresponding eigenvector or the eigenmode. The imaginary part is related to the frequency of oscillation of the corresponding eignemode. If the system is perturbed using a particular eigenmode, the oscillation which develops in the system exhibits the frequency of the mode. The perturbation field shows the alternate appearance of the real and the imaginary parts of the eigenvector in time. If the growth rate of the mode is negative, it decays with time. The success of linear stability theory depends on finding a complete set of normal modes to represent the development of an arbitrary initial perturbation. In this theory, the long-time dynamics of the flow is determined by the unstable eigenmode. A general perturbation may contain several modes. One therefore concludes that if all the eigenvalues of the system have negative real part then all the modes, and hence, all possible infinitesimal perturbations decay. The system is regarded as stable. On the other hand, even if one of the eigenvalues has a positive real part then arbitrary perturbations grow, and therefore, the system is said to be unstable. If the unstable eigenvalue is real, the system does not undergo oscillatory motion. The perturbation either grows or decays without oscillating. If the perturbation grows without oscillating, the system generally settles to another steady state. In the language of dynamical systems, we say that the system has encountered a pitch-fork bifurcation (Sahin & Owens [5]). However, if the unstable mode is complex, the system exhibits an oscillatory growth. In the language of dynamical systems, we say that the system has undergone a Hopf-bifurcation (Mathis *et al.* [6], Sreenivasan *et al.* [7]). The oscillations settle to a periodic state. A detailed discussion on linear stability analysis of fluid flows can be found in standard texts like Drazin & Reid [8] and Schmid & Henningson [9].

The linear stability analysis can be conducted in the local or global sense depending on the nature of the base flow. Local stability analysis is used in nonparallel flows where the local parallel flow approximation may be considered reasonable. Global stability analysis is used for a general two-dimensional or three-dimensional flow.

1.5.1 Local stability analysis

In the local stability analysis, one assumes the base flow profile at the station of interest in the flow field to be parallel and determines its stability characteristics via analysing the Rayleigh equation for inviscid flows or the Orr-Sommerfled equation for viscous flows (Drazin & Reid [8]). Generally, one also determines whether the base flow is absolutely/convectively unstable at various stations in the flow field. If in a flow field, an arbitrarily small perturbation, introduced at any location, grows in time and spreads both upstream and downstream of the location and contaminates the entire flow field in due course of time, the flow is said to be absolutely unstable, whereas, if the disturbance is swept downstream or upstream as it grows, so that, after sufficient time, the flow field returns to its original state, the instability is said to be convective. The local stability analysis has limitations. It does not reveal the stability characteristics of the entire system. It does not directly relate to the nonparallel flow. Using asymptotic theory, it is possible to show that the global instability resulting in self-sustained oscillations in nonparallel flows do not occur until a sufficient region in the flow field is absolutely unstable based on the parallel flow approximation. For flow past a circular cylinder, it is found that a region of absolute instability appears in the flow field at $Re \simeq 25$ (Monkewitz [10], Pier [11]), while the flow remains globally stable until $Re \approx 47$.

1.5.2 Global stability analysis

When the base flow is highly nonparallel, one conducts stability analysis of the entire flow field simultaneously. This is sometimes referred as the biglobal or triglobal analysis depending on the dimensionality of the base flow. One generally, carries out the temporal stability analysis by separating the time part in the linearized perturbation equation. The resulting eigenvalue problem is solved to determine the temporal modes and their growth rate. Interestingly, for nonparallel flows, the temporal stability analysis marks the onset of instability in the flow field. This is unlike the parallel flows where the temporal instability, generally, marks the onset of convective instability and the perturbation introduced in the flow field ultimately gets washed out of the domain.

Most of the fluid flow problems are either two-dimensional or three dimensional. The global linear stability analysis of these problems helps reveal great understanding of the fluid flow phenomenon. In this work, we determine the stability of flow past elliptic cylinders by performing the global linear stability analysis of two-dimensional steady base flow. The mathematical equations associated with the global linear stability analysis of steady flows are discussed in chapter 3. For more details on the global linear stability analysis, one can refer to the work by Noack & Eckerman [12] and the review paper by Theofilis [13].

1.6 Structural sensitivity and passive control

In the present work, we examine the sensitivity of the global linear modes to structural perturbations. The sensitivity analysis provides us with the information which could be used to effect flow control. We use this approach to effect selective control of the unstable modes in order to determine the resulting flow dynamics.

Structural perturbations refer to the "mild" change in the structure of the problem, i.e., the change either in the boundary conditions or in the governing equations. For example, the introduction of small objects in the flow field causing change in the base flow and/or the boundary conditions. This gives us a means to effect passive control. One could also effect an active control based on pressure and velocity feedback. The sensitivity of the global linear modes is determined by measuring the drift in the eigenvalue and the change in the corresponding eigenmode brought about by a general structural perturbation. One possible way to conduct this study is to determine the region in the flow field where by introducing the perturbation the drift in the eigenvalue is the largest. Since the flow dynamics at low *Re* is governed by a few modes, we determine this region for each of the modes separately. A simple analysis shows that the region in the flow field which is most sensitive to the structural perturbations, which do not involve the change in the base flow, is given by the overlap of the direct and the adjoint modes. From this analysis one may also conclude that the overlap region is the region where the dynamics responsible for the growth of the mode is active. Hence, this is identified as the core of instability. This is explained in more detail in Giannetti & Luchini [14]. Many researchers in the past have investigated the structural sensitivity of the eigenmode responsible for the von Kármán vortex shedding (Giannetti & Luchini [14], Marquet *et al.* [15]). We conduct a similar analysis in this work.

1.7 Control of vortex shedding

As mentioned in the previous section, we, in the present thesis, offer selective control of the unstable modes obtained from the linear stability analysis. There are various different ways of effecting flow control presented in the literature (Choi*et al.* [16], Strykowski & Sreenivasan [17]). They are primarily classified into two: active control methods and passive control methods. The active control is achieved by using techniques which involve feedback based on velocity and pressure fields or other active control mechanisms like acoustic excitation, suction and blowing, and rotary oscillations of cylinders kept in the wake. In the present work, passive control is effected using a slip-plate. The slip-plate allows the flow to slip along itself. It is placed on the wake centerline. Since, the plate inhibits cross-stream oscillations, it acts as a means to suppress the growth of the modes. If all the unstable modes are suppressed, the vortex shedding in the wake ceases and the flow settles down to a steady state. If one or more of them are allowed to grow then the flow develops the corresponding characteristic dynamics. We use the information from structural sensitivity analysis of the unstable modes as well as conduct more elaborate study for carrying out passive control of the cylinder wake.

1.8 Layout of the thesis

In this thesis we conduct a study of the two-dimensional flow past elliptic cylinders. A comprehensive investigation of the flow behaviour is carried out by varying the flow Reynolds number, cylinder aspect ratio and the domain width. Both the steady flow and the linear stability analysis is conducted in order to understand the role of the unstable modes in the flow dynamics. In chapter 2, we present a review of the research carried out in the past. Chapter 3 presents the governing equations for the fluid flow and the numerical method used to solve them. In chapter 4, we discuss the main characteristics of the steady flow past elliptic cylinders like the bubble length, the bubble width, the separation Reynolds number, the separation angle, the drag coefficient, the front and rear stagnation pressure and the maximum vorticity on the surface of the cylinder. In chapter 5, we carry out the linear stability analysis of steady base flow past elliptic cylinders. The unstable modes, their growth rate and the corresponding Strouhal number for cylinders of different aspect ratio are presented. The effect of blockage on the stability properties is also discussed. In Chapter 6, we perform structural sensitivity analysis to find the region best suitable for effecting control of the unstable modes. In Chapter 7, we show that the linear stability computations with slip-plate of small size placed at different locations on the centerline give more information than the sensitivity analysis. We then carry out unsteady computations by selectively suppressing one or more linear modes to see the kind of flow which evolves and, as a result, make an attempt to understand the role of the unstable linear modes in the fully developed nonlinear flow. Finally, we present the conclusion and future scope of the work in chapter 8.

Indian Institute of Technology Guwahati

Chapter 2

Literature review

A brief review of the research carried out in the past, on the relevant aspects of flow past elliptic cylinders, is presented below. First, the discussion about the steady flow results is presented. This is followed by a brief review of the linear stability studies.

2.1 Steady flow

The physics of bluff body wakes has attracted many researchers since the advent of fluid mechanics. In general, wake flows at low Reynolds number (Re) are steady. They become unsteady at a relatively higher Re. The structure and characteristics of the steady flow past a bluff body is quite rich and has been the subject of serious investigation by several researchers in the past. Flow past circular and elliptic cylinders is the most prominent in this area. Studies have been conducted via experimental (Taneda [18], Gerrard [19], Coutanceau & Bouard [20], Williamson [21], Zdravkovich [22]), computational (Jain & Rao [23], Dennis & Chang [24], Fornberg [25], Fornberg [2], Gajjar & Azzam [3], Sen *et al.* [1], Dennis & Chang [26], D'Alessio & Dennis [27], Dennis & Young [28], Faruquee *et al.* [29], Sivakumar *et al.* [30], Sen *et al.* [31], Sen *et al.* [32], Paul *et al.* [33], Sen [34]) and theoretical (Tomotika & Aoi [35], Yamada [36], Underwood [37], Smith [38], Chernyshenko [39], Chernyshenko & Castro [40], Chernyshenko [41], Hasimoto [42], Imai [43], Takaisi [44], Tamada *et al.* [45], Shintani *et al.* [46]) methods to understand the nature of these flows. One can obtain the steady flow past bluff bodies at

Re far beyond the onset of unsteadiness using computational methods. In spite of the simplicity of the problem, because it involves only one variable, Re, the computation of steady flow at higher Re is quite difficult. The computational difficulties encountered while obtaining a steady-state solution of the Navier-Stokes equations at higher Re are discussed in Fornberg [2] and Fornberg & Elcrat [47]. A ride through the literature reveals that though the investigation of the steady flow past a circular cylinder is quite extensive, the same for elliptic cylinders is mostly limited to low Re.

Flow past a circular cylinder has been investigated by several researchers in the past. Fornberg [48] conducted numerical investigation of the flow up to $Re = 600$. He found that the bubble length increases linearly with Re whereas the bubble width grows as $Re^{0.5}$ up to $Re = 300$ and increases linearly thereafter. Smith [38] found that the bubble length, the bubble width and the drag coefficient vary linearly with Re, $Re^{0.5}$ and $Re^{-0.5}$, respectively. Theoretical studies by Smith [49], Peregrine [50] and Chernyshenko [39] also confirm that, at higher Re, the bubble length and the bubble width vary linearly with Re. Recently, Sen *et al.* [1] numerically obtained the steady flow past a circular cylinder in the range $6 \leq Re \leq 40$. They found that the bubble length, separation angle, base suction, total drag, pressure drag, viscous drag and the maximum vorticity on the surface of the cylinder vary linearly with Re, $Re^{-0.5}$, Re^{-1}, $Re^{-0.5}$, $Re^{-0.64}$, $Re^{-0.60}$ and $Re^{0.5}$, respectively.

For flow past an elliptic cylinder, studies show that the change in the aspect ratio (minor axis/major axis) of the elliptic cylinder significantly affects the flow behaviour. Dennis & Chang [26] numerically solved the Navier-Stokes equations for steady two-dimensional flow past elliptic cylinders of different aspect ratio ($Ar = 0$, 0.05, 0.1, 0.2, 0.4) placed parallel to the free stream. They reported the values of the frictional drag coefficient and the pressure drag coefficient for $Re = 40$. They found that the frictional drag coefficient decreases with decrease in Ar while the pressure drag coefficient increases. D'Alessio & Dennis [27] reported the drag and lift coefficients for an inclined elliptic cylinder ($0° \leq \alpha \leq 90°$; $Ar = 0.2$) at $Re =$ 5 and 20. Here α represents the angle which the major axis of the ellipse makes with the streamwise axis. The lift coefficient was found to first increase and then decrease with increase in α. It was found to decrease with increase in Re. For the drag coefficient, they found an increase with increase in α and decrease with increase in Re. They also observed that, at $Re = 5$, no separation of flow occurs for $\alpha \leq 30°$. As the inclination is increased, the separated region appears and is clearly seen at

$\alpha = 70°$. At slightly higher Re $(= 20)$, they showed that the separation begins at $\alpha = 40°$. For $\alpha = 90°$, a symmetrical vortex pair is formed behind the cylinder at $Re = 5$ and 20. Dennis & Young [28] numerically investigated the steady two-dimensional flow past elliptic cylinders ($Ar = 0.1, 0.2$) with different inclination and the flow Reynolds number in the range 1-40. They presented the variation of the coefficients of lift and drag, and the streamline patterns for different α and Re. They found that, with increasing inclination, separation eventually occurs, and the lift to drag ratio decreases. They also presented a bifurcation diagram to demonstrate how flow patterns vary with inclination. For $\alpha = 90°$, they found the symmetric flow with two attached vortices behind the cylinder.

Faruquee *et al.* [29] studied $Re = 40$ (steady) flow around an elliptical cylinder with its major axis parallel to the free-stream. They explored the effect of Ar on the shape of the wake bubble and the pressure and velocity distributions in the flow field. They determined the length of the wake bubble from the plots of the streamlines and velocity vector, and also from the plot of the rear axis velocity along the streamwise central line. They found that the bubble length, the bubble width and the drag coefficient increase with the increase in Ar. They reported quadratic correlations for the bubble length and the drag coefficient in terms of Ar. They also found the critical Ar $(= 0.34)$ for the flow to form a pair of steady vortices. Below this Ar, no separation bubble was seen. Sivakumar *et al.* [30] did a comprehensive study of the steady flow characteristics (drag coefficient, bubble length, surface pressure distribution) for flow past elliptic cylinders ($0.2 \le Ar \le 5$) with their major axis perpendicular to the incoming flow. The Reynolds number in their study was allowed to vary in the range 0.01-40. They studied the same for non-Newtonian fluids with the power-law index in the range 0.2-1.8. For constant Re, the bubble length was found to decrease with the increase in Ar irrespective of the fluid properties. They reported the functional relationship for drag coefficient and stagnation pressure coefficient in terms of Ar, Re and the power-law index.

Sen *et al.* [32] used the stabilized finite-element method to study the steady separated flow past an elliptic cylinder with different aspect ratio ($Ar = 0.2$, 0.5, 0.8, 1.0). They computed the steady flow up to $Re = 40$ and varied the angle of incidence (α) between 0° and 90°. They determined the critical Re for flow separation for different Ar and α. They found that the critical Re for flow separation decreases with the decrease in Ar but shows non-monotonic variation with α. They also reported the steady flow characteristics like the bubble length, the maximum vorticity on the surface of the cylinder and the separation angle for different Ar and α. For $\alpha = 0°$ and $90°$, the bubble length increases linearly with Re irrespective of Ar while the separation angle shows non-linear variation. Sen *et al.* [31] compared the steady flow characteristics of elliptic cylinders (of different Ar) placed perpendicular to the free-stream with the same for a square cylinder. They presented the variation of bubble length, bubble width, separation angle, frictional drag coefficient, pressure drag coefficient and the total drag coefficient with increasing Re. They found that among all the cylinder shapes, the critical Re for flow separation is smallest ($= 1.05$) for $Ar = 0.2$ and largest ($= 6.29$) for a circle. Compared to the circular cylinder, the square cylinder generates more drag and creates a separation bubble with larger length and width at the same Re. Also, the flow separates at a much lower Re for the square cylinder. Recently, Sen [34] studied the steady flow characteristics for cylinders of different aspect ratio ($Ar = 0.2,\ 0.5,\ 0.8$). They presented the results for $Re \leq 40$ and $0° \leq \alpha \leq 90°$. The discussion on pressure distribution and viscous forces on the cylinder are the main highlights of their work. They found that for $Re = 40$, elliptic cylinders of $Ar \leq 0.5$ behave like a streamlined body for $\alpha < 20°$ and like a bluff body for $\alpha \geq 20°$. An elliptic cylinder of $Ar = 0.2$ behaved as the best bluff body for $\alpha = 90°$ and as the best streamlined body for $\alpha = 0°$. These conclusions were obtained by observing the ratio of the pressure drag coefficient and the frictional drag coefficient. Paul *et al.* [33] studied the combined effect of Ar and α on critical Re for flow separation and the same for transition from the steady flow to unsteady flow. They presented the empirical equations for the critical parameters as a function of Ar and α.

Yoon *et al.* [51] numerically studied the flow around an inclined elliptic cylinder for Re in the range 20 to 100. They constructed a bifurcation diagram to distinguish the existence of the recirculation region behind the elliptic cylinder and showed the transition of flow from the steady to unsteady regime using a stability diagram. Shi *et al.* [52] numerically investigated the wake of elliptic cylinders at $Re = 150$. They varied Ar and α, in the range 0.25-1.0 and 0°-90°, respectively. They found three distinct wake patterns (patterns I, II, III) with the change in Ar and α. Pattern I refers to the presence of the steady wake behind the cylinder. It appears for $Ar < 0.37$ and $\alpha < 2.5°$. Pattern II is characterized by the presence of the Karman wake followed by a steady wake. It appears for $0.25 \leq Ar \leq 1.0$ and depends on α. Pattern III appears for $Ar \leq 0.67$ and $\alpha > 52°$. It refers to the presence of the Karman wake followed by the secondary wake. More recently, Kumar and Sahu [53] studied the two-dimensional flow phenomena of power-law fluids past an unconfined rotating elliptic cylinder in the laminar flow regime. They consider several parameters like Re (5-40), Ar (0.1-0.7), power-law index (0.4-1.8), and non-dimensional rotational speed (1, 2, and 4). They presented the lift and drag coefficients as functions of these parameters.

Blockage significantly affects the behaviour of the flow past bluff bodies and reveals exciting features that generally do not appear in unbounded flow. In general, the definition used in the literature expresses blockage as the cross-stream dimension of the body divided by the cross-stream width of the domain. In this work, half-width (H) of the domain is used to show the effect of blockage. Several researchers (Fornberg [2], Anagnostopoulos *et al.* [54], Gajjar & Azzam [3], Sen *et al.* [1], Singha & Sinhamahapatra [55], Mishra *et al.* [56]) have investigated the effect of blockage on the steady flow past a circular cylinder. Fornberg [2] obtained the steady flow past a circular cylinder up to $Re = 700$ for the side boundaries located at a distance H varying in the range 2.5 to ∞ and up to $Re = 800$ for $2.5 \leq H \leq 50$. He found that the bubble length increases approximately linearly with Re for all values of H. For Reynolds number in the range 100-800, he reported that the bubble length and the bubble width decrease with the decrease in H, while the drag coefficient and the maximum vorticity on the surface of the cylinder increase.

Anagnostopoulos *et al.* [54] studied the flow past a circular cylinder at $Re = 106$ for blockage ratio 0.05, 0.15 and 0.25. Here, the blockage ratio is defined as the reciprocal of the domain half-width. They showed that when the lateral boundaries come close to the cylinder, the vortices formed behind the cylinder are suppressed and the bubble length reduces. The value of the absolute pressure, the front stagnation pressure, the total drag coefficient, the pressure drag coefficient and the maximum vorticity on the surface of the cylinder increase with increase in blockage. Gajjar & Azzam [3] presented the results for steady flow characteristics like the bubble length, the bubble width, the drag coefficient and the maximum vorticity on the surface of the cylinder for the domain half-width (H) = 2.5, 10, 25 and 50 for Re up to 3500, 2500, 2500 and 1400, respectively. They reported the presence of three different types of solutions with change in H. For small H (= 2.5), type I solution occurs in which a slender bubble is formed. Also, the length of the bubble increases with increase in Re. As H increases, the bubble characteristics vary significantly and type II solution appears. The bubble width shows an unusual growth near the downstream end. The bubble length and width increase with Re. For large H (25 and more), type III solution is seen. In this case, both the length as well as the width of the bubble become very large.

Sen *et al.* [1] investigated the steady flow past a circular cylinder for $6 \leq Re \leq 40$ and the blockage ratio in the range 0.000125-0.80. They reported the critical Reynolds number (Re_S) for flow separation as 6.29 for the blockage ratio approximately equal to 0.05. They found that, for the blockage ratio less than 0.01, the steady flow characteristics are independent of blockage. For $6 \leq Re \leq 40$, the bubble length, the separation angle and Re_S show non-monotonic variation with the blockage ratio. Singha & Sinhamahapatra [55] computed the steady flow past a circular cylinder for $Re = 45$, 100, 150, 200 and 250 with the domain half-width (H) in the range 1-4. They showed that transition to vortex shedding regime is delayed when the lateral wall are close to the cylinder because of the interaction between the vortices from the lateral wall and the cylinder wake. More recently, Mishra *et al.* [56] studied the flow past a circular cylinder for $4 \leq Re \leq 100$ and the blockage ratio 0.9. They found that the large blockage ratio causes a drastic fall of pressure on the cylinder surface and much-delayed inception of adverse pressure gradient. This results in a delayed flow separation, and the value of Re_S increases from 6.19 (unbounded) to 27.8 (blockage ratio = 0.9). The bubble length shows linear variation up to $Re = 50$, and beyond that, it varies non-linearly with Re. They presented the least square fit equation for the total drag coefficient and the pressure drag coefficient as a function of Re^{-1}.

2.2 Linear stability analysis

The transition of flow from steady to unsteady state occurs at Re depending on the aspect ratio of the cylinder and also to some extent on the blockage of the computational domain. Several researchers in the past have conducted linear stability analysis of steady flow past elliptic cylinders in order to investigate the transition phenomenon. Jackson [57] employed finite-element formulation along with inverse iteration to carry out the linear stability analysis. He reported $Re = 45.40$ for the onset of vortex shedding in flow past a circular cylinder. The same for elliptic cylinders of different aspect ratios at different angles of incidence was also presented. Zebib [58] employed a spectral method to compute the steady, incompressible laminar flow past a circular cylinder. He found, via linear stability analysis, the range for the critical Reynolds number and Strouhal number as 39-43 and 0.11-0.13, respectively. Noack & Eckelmann [12] carried out linear stability analysis of steady and periodic flow past a circular cylinder using low-dimensional Galerkin method. They showed that the onset of two-dimensional vortex shedding is a supercritical Hopf bifurcation. They also performed Floquet stability analysis to identify the secondary instability, which causes three-dimensionality to appear in the flow.

Morzyński *et al.* [59] employed the subspace iteration method with the inverse Cayley transformation to solve the eigenvalue problem resulting from the linear stability analysis of flow past a circular cylinder. They reported the critical Reynolds number and Strouhal number as 47 and 0.132 respectively. Paul *et al.* [33] conducted linear stability analysis of flow past elliptic cylinder placed perpendicular to the incoming free-stream. They reported the critical Reynolds number and Strouhal numbers for aspect ratios of the cylinder varying from 0.1 to 1.0. They also reported the critical parameters for varying inclination of the elliptic cylinder. More recently, Yoon *et al.* [51] numerically studied the flow around an inclined elliptic cylinder for Reynolds numbers in the range 20 to 100. They constructed a bifurcation diagram to distinguish the existence of recirculation region behind the elliptic cylinder and showed the transition of flow from steady to unsteady using a stability diagram.

For flow past a circular cylinder, Barkley & Henderson [60] concluded that there is only one mode which becomes unstable leading to the primary wake instability in a two-dimensional flow before the three-dimensionality appears. In contrast, Boppana & Gajjar [61] reported the presence of a second unstable mode before the onset of three-dimensionality. According to them, the second unstable mode loses stability somewhere between $Re = 125$ and 150. In the same year, Verma & Mittal [62] performed two-dimensional linear stability analysis for flow past a circular cylinder. They reported $Re = 110.8$ for the onset of instability of the second mode. They found that structure of the second mode is very similar to the primary mode. However, it is associated with a smaller growth rate and a larger Strouhal number. They studied the relative role of two modes in the development of von Kármán vortex shedding through non-linear regimes. They concluded that the nonlinear computation beginning with either mode leads to the same flow with the same Strouhal number.

The location of the lateral walls of the computational domain has a noticeable effect on the instability of the flow. Zebib [58] suggested that the critical parameters at the onset of instability depend on the size of the computational domain.

Later, many researchers (Chen *et al.* [63], Sahin & Owens [5], Kumar & Mittal [64], Boppana & Gajjar [61]) studied this and referred it as the blockage effect. Chen *et al.* [63] performed numerical and experimental analysis to study flow past a cylinder confined between parallel planes. They used a parabolic velocity profile at the inlet and imposed the no-slip boundary conditions on the lateral walls. For linear stability studies, they considered blockage ratios in the range 0.1 to 0.7. They reported the critical Reynolds number and Strouhal number for the onset of unsteadiness in the given range of blockage ratios. Sahin & Owens [5] studied a similar problem for Re in the range 0 to 280, for blockage ratio 0.1-0.9. They found the presence of at least three separate curves of neutral stability representing the transition from symmetric steady flow to unsteady flow, symmetric steady flow to asymmetric steady flow and asymmetric steady flow to unsteady flow, respectively.

Mittal & Kumar [65] and Kumar & Mittal [64, 66] utilized the stabilized finite element formulation for conducting the linear stability analysis of two-dimensional flow past a circular cylinder. Kumar & Mittal [64] studied blockage effect on the instability of flow past a circular cylinder and explained the discrepancies present in the data for the critical Reynolds number and Strouhal number reported by earlier studies. They conducted computations for blockage ratio in the range 0.005 to 0.125. They found that the critical Reynolds number for the onset of instability first decreases and then increases with the blockage. However, the critical Strouhal number increases monotonically with the increase in blockage. They also proposed equations relating the critical parameters with the blockage ratio. Boppana & Gajjar [61] studied the instability of flow past a row of circular cylinders with blockage ratios in the range 0.02-0.4. They showed the presence of a second mode in the flow which becomes unstable between $Re = 125$ and 150 for a blockage ratio equal to 0.1.

2.3 Structural sensitivity analysis and passive control

It is known that the presence of vortex shedding in the wake of a bluff body causes undesirable effects such as structural vibrations, acoustic noise and resonance. In the past, researchers have explored various ways of effecting control of vortex shedding. The controlling methods can be classified as passive, active open-loop and active closed-loop (or feedback control), respectively. Generally, for passive control, objects such as a small control cylinder (Strykowski & Sreenivasan [17], Mittal & Raghuvanshi [67]), a plate (Roshko [68], Gerrard [19], Lin & Wu [69], Ozono [70], Mittal [71], Serson *et al.* [72], Soumya & Prakash [73]) are utilized. In particular, studies with plate have been quite popular. In computational investigations sometimes even a slip-plate is used. A slip-plate is a hypothetical plate which allows slip of velocity along its surface and prevents any flow normal to it. Recently, Serson [72] compared the effect of a plate with slip boundary condition and with no-slip boundary condition. They showed that the effect of the boundary condition is restricted to a thin boundary layer near the plate and slip-wall boundary condition is also able to capture most of the flow physics. They encouraged the use of slip-wall boundary conditions for the fact that it reduces the computational cost of the simulations. Mittal [71] carried out the numerical computation with slip-plates of various length placed at different locations on the centerline of the flow field of $Re = 100$ flow past a circular cylinder. He found that the shortest length of the plate required to suppress vortex shedding is two cylinder diameters, approximately, and needs to be located in the latter part of the wake bubble of the basic unperturbed flow.

Alternatively, one could use the structural sensitivity of the stability problem to determine the most effective location to control the dynamics of the flow. Many researchers (Chomaz [74], Giannetti & Luchini [14], Marquet *et al.* [15], Kumar & Mittal [75]) in the past have investigated the structural sensitivity of the eigenmode responsible for von Kármán vortex shedding. The results suggest that the core of the global instability can be located as the region where the product of the associated direct and the adjoint eigenmodes is nonzero.

2.4 Closure and objectives

From the above literature review we notice the following. Most of the investigations for steady flow past elliptic cylinders are limited to low Re and are in a limited range of other parameters. We, in this work, plan to conduct a detailed analysis of the steady flow characteristics by varying the flow Re, Ar, and the domain width. The literature on linear stability studies for flow past elliptic cylinders are relatively scarce. Accordingly, we plan to investigate the stability properties of steady flow past elliptic cylinders in order to gain an insight into the cause and behaviour of the various shedding patterns in the cylinder wake. We perform the structural sensitivity analysis of flow past elliptic cylinders to locate the most sensitive region of the instability modes. Thereafter, we make an attempt to determine the role of the instability modes in the unsteady flow and seek connection of the structures in the flow with those of the modes.

Indian Institute of Technology Guwahati

Chapter 3

Numerical method

The governing equations for the fluid flow are the Navier-Stokes equations. A stabilized finite element method for solving these equations has been developed and used by several researchers in the past (Hughes & Brooks [76], Brooks & Hughes [77], Tezduyar *et al.* [78], Mittal [79], Mittal & Kumar [65]). In this work, we solve the Navier-Stokes equations and the eigenvalue problem resulting from the linear stability equations using the stabilized finite element (SUPG and PSPG) formulation presented in Kumar & Mittal [65]. One may refer to the same for more details. Below, we present the governing flow equations and a brief description of the finite element formulation.

3.1 The governing equations

3.1.1 The incompressible flow equations

Let $\varOmega \subset \mathbb{R}^{n_{\rm sd}}$ and $(0, T)$ be the spatial and temporal domains respectively, where $n_{\rm sd}$ is the number of space dimensions, and let $\varGamma$ denote the boundary of $\varOmega$. The spatial and temporal coordinates are denoted by $\boldsymbol{x}$ and t. The Navier–Stokes equations governing incompressible fluid flow are

$$\rho\left(\frac{\partial \boldsymbol{u}}{\partial t} + \boldsymbol{u} \cdot \nabla \boldsymbol{u} - \mathbf{f}\right) - \nabla \cdot \boldsymbol{\sigma} = 0 \qquad \text{on } \varOmega \times (0, T), \tag{3.1}$$

$$\nabla \cdot \boldsymbol{u} = 0 \qquad \text{on } \varOmega \times (0, T). \tag{3.2}$$

Here $\rho, \boldsymbol{u}, \mathbf{f}$, and $\boldsymbol{\sigma}$ are the density, velocity, body force and the stress tensor, respectively. The stress tensor is written as the sum of its isotropic and deviatoric parts:

$$\boldsymbol{\sigma} = -p\mathsf{I} + \mathsf{T}, \quad \mathsf{T} = 2\mu\boldsymbol{\varepsilon}(\boldsymbol{u}), \quad \boldsymbol{\varepsilon}(\boldsymbol{u}) = \frac{1}{2}((\nabla\boldsymbol{u}) + (\nabla\boldsymbol{u})^{\mathrm{T}}), \tag{3.3}$$

where p and μ are the pressure and coefficient of dynamic viscosity, respectively. Both the Dirichlet and Neumann-type boundary conditions are accounted for, represented as

$$\boldsymbol{u} = \boldsymbol{g} \quad \text{on } \mathit{\Gamma}_{\mathrm{g}}, \quad \boldsymbol{n}\cdot\boldsymbol{\sigma} = \boldsymbol{h} \quad \text{on } \mathit{\Gamma}_{h}, \tag{3.4}$$

where $\mathit{\Gamma}_g$ and $\mathit{\Gamma}_h$ are complementary subsets of the boundary $\mathit{\Gamma}$. The initial condition on the velocity is specified on $\mathit{\Omega}$:

$$\boldsymbol{u}(\boldsymbol{x}, 0) = \boldsymbol{u}_0 \text{ on } \mathit{\Omega}, \tag{3.5}$$

where $\boldsymbol{u}_0$ is divergence free.

3.1.2 Equations for the linear stability analysis of the flow

To conduct a global, linear stability analysis of a non-parallel flow the unsteady solution is expressed as a combination of the steady solution and the disturbance:

$$\boldsymbol{u} = \boldsymbol{U} + \boldsymbol{u}', \quad p = P + p'. \tag{3.6}$$

Here, $\boldsymbol{U}$ and P represent the steady-state solution whose stability is to be determined while $\boldsymbol{u}'$ and p' are the perturbation fields of the velocity and pressure, respectively. Substituting Eq. (3.6) in Eqs. (3.1), (3.2) and subtracting from them, the equations for steady flow, and then dropping the nonlinear term, one obtains the linearized perturbation equations:

$$\rho\left(\frac{\partial\boldsymbol{u}'}{\partial t} + \boldsymbol{u}'\cdot\nabla\boldsymbol{U} + \boldsymbol{U}\cdot\nabla\boldsymbol{u}'\right) - \nabla\cdot\boldsymbol{\sigma}' = 0 \qquad \text{on } \mathit{\Omega}\times(0, T), \tag{3.7}$$

$$\nabla\cdot\boldsymbol{u}' = 0 \qquad \text{on } \mathit{\Omega}\times(0, T). \tag{3.8}$$

Here, $\boldsymbol{\sigma}'$ is the stress tensor for the perturbed solution computed using Eq. (3.3). We further assume that the disturbances are of the following form:

$$\boldsymbol{u}'(\boldsymbol{x}, t) = \hat{\boldsymbol{u}}(\boldsymbol{x})\mathrm{e}^{\lambda t}, \tag{3.9}$$

$$p'(\boldsymbol{x}, t) = \hat{p}(\boldsymbol{x})\mathrm{e}^{\lambda t}. \tag{3.10}$$

Substituting Eqs. (3.9) and (3.10) in Eqs. (3.7) and (3.8) we get:

$$\rho(\lambda\,\hat{\boldsymbol{u}} + \hat{\boldsymbol{u}}\cdot\nabla\boldsymbol{U} + \boldsymbol{U}\cdot\nabla\hat{\boldsymbol{u}}) - \nabla\cdot\hat{\boldsymbol{\sigma}} = 0 \quad \text{on } \Omega, \tag{3.11}$$

$$\nabla\cdot\hat{\boldsymbol{u}} = 0 \quad \text{on } \Omega. \tag{3.12}$$

Here, λ is the eigenvalue of the fluid system and governs its stability. In general, $\lambda = \lambda_\mathrm{r} + \mathrm{i}\lambda_\mathrm{i}$ where λ_r and λ_i are the real and imaginary parts, respectively. The steady-state solution $(\boldsymbol{U}, P)$ is associated with an unstable mode if the corresponding eigenvalue has a positive real part. The boundary conditions for $\hat{\boldsymbol{u}}$ and $\hat{p}$ are the homogeneous versions of the ones for U and p as specified by Eq.(3.4).

3.2 The finite element formulation

3.2.1 The incompressible flow equations

Consider a finite element discretization of Ω into subdomains Ω^e, $\mathrm{e} = 1, 2, ..., n_{el}$, where n_{el} is the number of elements. Based on this discretization, for velocity and pressure we define the finite element trial function spaces $\zeta^h_{\boldsymbol{u}}$ and ζ^h_p, and weighting function spaces $\mathcal{V}^h_{\boldsymbol{u}}$ and $\mathcal{V}^h_p$. These function spaces are selected, by taking the Dirichlet boundary conditions into account, as subsets of $[\mathbf{H}^{1h}(\Omega)]^{n_\mathrm{sd}}$ and $\mathbf{H}^{1h}(\Omega)$, where $\mathbf{H}^{1h}(\Omega)$ is the finite-dimensional function space over Ω. The stabilized finite element formulation of Eqs. (3.1) and (3.2) is written as follows: find $\boldsymbol{u}^h \in \zeta^h_{\boldsymbol{u}}$ and $p^h \in \zeta^h_p$ such that $\forall \mathbf{w}^h \in \mathcal{V}^h_{\boldsymbol{u}}$ and $q^h \in \mathcal{V}^h_p$

$$\begin{aligned}
&\int_\Omega \mathbf{w}^h\cdot\rho\left(\frac{\partial\boldsymbol{u}^h}{\partial t} + \boldsymbol{u}^h\cdot\nabla\boldsymbol{u}^h - \mathbf{f}\right)\mathrm{d}\Omega + \int_\Omega \boldsymbol{\varepsilon}(\mathbf{w}^h) : \boldsymbol{\sigma}(p^h, \boldsymbol{u}^h)\,\mathrm{d}\Omega \\
&+ \int_\Omega \mathrm{q}^h\,\nabla\cdot\boldsymbol{u}^h\,\mathrm{d}\Omega + \sum_{e=1}^{n_{el}}\int_{\Omega^\mathrm{e}} \frac{1}{\rho}\Big(\tau_\mathrm{SUPG}\,\rho\,\boldsymbol{u}^h\cdot\nabla\mathbf{w}^h + \tau_\mathrm{PSPG}\nabla q^h\Big)\cdot \\
&\qquad\left[\rho\left(\frac{\partial\boldsymbol{u}^h}{\partial t} + \boldsymbol{u}^h\cdot\nabla\boldsymbol{u}^h - \mathbf{f}\right) - \nabla\cdot\boldsymbol{\sigma}(p^h, \boldsymbol{u}^h\right]\mathrm{d}\Omega^e \\
&+ \sum_{e=1}^{n_{el}}\int_{\Omega^\mathrm{e}} \tau_\mathrm{LSIC}\,\nabla\cdot\mathbf{w}^h\rho\nabla\cdot\boldsymbol{u}^h\,\mathrm{d}\Omega^\mathrm{e} = \int_{\Gamma_h} \mathbf{w}^h\cdot\boldsymbol{h}^h\,\mathrm{d}\Gamma.
\end{aligned} \tag{3.13}$$

Equation 3.13 represents the Galerkin formulation to which the SUPG, PSPG and the Least square stabilization terms are added. It is well known that the

Galerkin formulation is unstable for the convection dominated flows. The SUPG and PSPG terms give stability to the basic formulation and allow the use of equal order interpolation functions for velocity and pressure (Tezduyar *et al.* [78]). The least square term gives additional stability at higher Reynolds numbers. The SUPG formulation was first introduced by Hughes & Brooks [76] and Brooks & Hughes [77]. Hughes *et al.* [80] first proposed the Petrov-Galerkin term allowing the usage of equal-order interpolations for velocity and pressure for Stokes flows. These formulations were later extended by Tezduyar *et al.* [78] for finite-Reynolds-number flows. The same for conducting the linear stability analysis of steady flows was first introduced by Mittal & Kumar [65]. It has been validated by several related studies involving the analysis of linear stability of steady and time-averaged flows (Kumar & Mittal [64, 66], Mittal *et al.* [81], Mittal [82, 83], Kumar *et al.* [84], Mittal [85], Mittal & Kumar [86], Kumar & Mittal [75]). The definition of the stabilization parameters being used in this work is the same as presented in Tezduyar *et al.* [78] and Mittal & Kumar [65].

3.2.2 Equations for linear stability analysis

Application of the FEM to the pertubartion equations, (3.11) (3.12), results in the following discrete equation: find $\hat{\boldsymbol{u}}^h \in \zeta^{h_u}$ and $\hat{p}^h \in \zeta^{h_p}$ such that $\forall \hat{\mathbf{w}}^h \in \mathcal{V}_{\boldsymbol{u}}^h$ and $\hat{q}^h \in \mathcal{V}_p^h$

$$\begin{aligned}
&\int_{\Omega} \hat{\mathbf{w}}^h \cdot \rho \left(\lambda \hat{\boldsymbol{u}}^h + \boldsymbol{U}^h \cdot \nabla \hat{\boldsymbol{u}}^h + \hat{\boldsymbol{u}}^h \cdot \nabla \boldsymbol{U}^h \right) \mathrm{d}\Omega + \int_{\Omega} \hat{\varepsilon}(\hat{\mathbf{w}}^h) : \hat{\boldsymbol{\sigma}}(\hat{p}^h, \hat{\boldsymbol{u}}^h)\, \mathrm{d}\Omega \\
&\quad + \int_{\Omega} \hat{q}^h \nabla \cdot \hat{\boldsymbol{u}}^h \mathrm{d}\Omega + \sum_{e=1}^{n_{el}} \int_{\Omega^e} \frac{1}{\rho} \left(\tau_{\mathrm{SUPG}}\, \rho\, \boldsymbol{U}^h \cdot \nabla \hat{\mathbf{w}}^h + \tau_{\mathrm{PSPG}} \nabla \hat{q}^h \right) \cdot \\
&\qquad \left[\rho \left(\lambda \hat{\boldsymbol{u}}^h + \boldsymbol{U}^h \cdot \nabla \hat{\boldsymbol{u}}^h + \hat{\boldsymbol{u}}^h \cdot \nabla \boldsymbol{U}^h \right) - \nabla \cdot \hat{\boldsymbol{\sigma}} \left(\hat{p}^h, \hat{\boldsymbol{u}}^h \right) \right] \mathrm{d}\,\Omega^e \\
&\qquad\qquad + \sum_{e=1}^{n_{el}} \int_{\Omega^e} \tau_{\mathrm{LSIC}} \nabla \cdot \hat{\mathbf{w}}^h \rho \nabla \cdot \hat{\boldsymbol{u}}^h \, \mathrm{d}\Omega^e = 0.
\end{aligned} \tag{3.14}$$

3.3 The eigenvalue problem

The formulation presented above for the differential eigenvalue problem leads to a generalized matrix eigenvalue problem of the form $AX - \lambda BX = 0$, where A and B

are non-symmetric matrices. Due to the continuity equation, matrix B is singular. We therefore solve the inverse eigenvalue problem $A^{-1}BX = (1/\lambda)X$. Sometimes, we shift the origin to gain faster convergence. We therefore solve the problem, $(A - \sigma B)^{-1}BX = \mu X$. Here, $\mu = 1/(\lambda - \sigma)$. This is referred as the shift-invert transformation. The subspace iteration method (Stewart & Miller [87]) in conjunction with shift-invert transformation is used to solve the eigenvalue problem. The solution to the eigenvalue problem results in the eigenpair (λ, X). Since the numerical dimension of the problem is usually very large, we look for the few modes which have the largest real part. In order to analyze the sensitivity of the modes to structural perturbations, both the direct and the adjoint modes are utilized (Giannetti & Luchini [14]). We therefore compute the direct as well as the adjoint modes. The adjoint modes satisfy the equation $A^TY - \lambda B^TY = 0$. Here A^T and B^T are the transpose of the matrices A and B.

Indian Institute of Technology Guwahati

भारतीय प्रौद्योगिकी संस्थान गुवाहाटी • Indian Institute of Technology Guwahati •

Chapter 4

Flow past elliptic cylinders

The structure and characteristics of the steady flow past a bluff body is quite rich and has been the subject of serious investigation by several researchers in the past. One can obtain the steady flow past bluff bodies at Re far beyond the onset of unsteadiness using computational methods. In spite of the simplicity of the problem, because it involves only one variable, Re, the computation of steady flow at higher Re is quite difficult. A ride through the literature reveals that though the investigation of the steady flow past a circular cylinder is quite extensive, the same for the elliptic cylinders is mostly limited to low Re. In this chapter, a comprehensive investigation of the steady flow past elliptic cylinders is carried out by varying the flow Reynolds number, the aspect ratio (Ar) and the domain width (H). Results are presented for $Re \leq 200$, $0.01 \leq Ar \leq 1.0$ and $10 \leq H \leq 100$.

In what follows, the problem set-up and the mesh convergence study is presented in section 4.1. In section 4.2, we present the steady flow results followed by the effect of blockage.

4.1 Problem set-up and the mesh convergence study

4.1.1 The computational domain and boundary conditions

The elliptic cylinder is placed symmetrically between upper and lower boundaries of a rectangular domain (see figure 4.1(a)). The major axis ($2a$) of the cylinder is perpendicular to the incoming flow. The ratio of the minor axis ($2b$) to the major

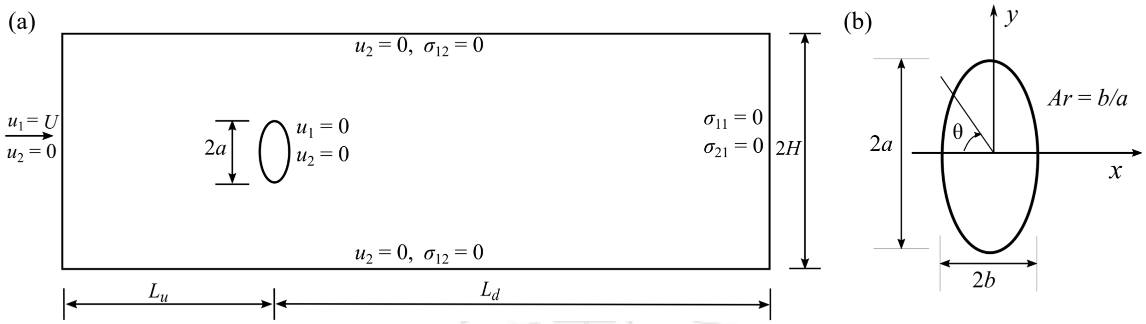

Figure 4.1: Flow past an elliptic cylinder: (a) domain and boundary conditions (L_u and L_d are the locations of the upstream and downstream boundaries, respectively; H is the half-width of the domain). (b) geometry of the elliptic cylinder. All linear distances are measured from the centre of the cylinder and angles are measured in clock-wise direction from the front stagnation point.

axis is defined as the aspect ratio ($Ar = b/a$). The origin of the Cartesian coordinate system coincides with the centre of the cylinder and the positive x direction is along the freestream flow. All angles are measured in the clock-wise direction from the front stagnation point of the cylinder. The unit for measuring length is taken as the semi-major axis of the ellipse. Therefore, different Ar correspond to different minor axes. In this work, we present results for nine different Ar values (1.0, 0.75, 0.5, 0.375, 0.25, 0.125, 0.0625, 0.03, 0.01) of the elliptic cylinder.

In figure 4.1, L_u, L_d and H denote the distance of the upstream, downstream and the lateral boundaries, respectively, from the centre of the cylinder. In present work, the upstream and downstream boundaries are located sufficiently far from the cylinder and have no significant influence on the overall flow field. L_u and L_d are 200 and 700, respectively. We change the domain size by changing H. Alternatively, this corresponds to different blockage which the flow experiences. We use five different H values (100, 50, 30, 20, 10) to study the effect of blockage. Blockage is defined as the reciprocal of the domain size. The closer the lateral boundaries are, the higher is the blockage.

The boundary conditions used to compute the steady flow are shown in figure 4.1(a). A free-stream value is assigned to the velocity at the upstream boundary. At the downstream boundary, a Neumann-type boundary condition for the velocity is specified that corresponds to stress-free conditions. On the upper and lower boundaries, the component of velocity normal to and the component of stress vector along these boundaries are prescribed a zero value. The no-slip boundary condition is applied on the surface of the cylinder. The boundary conditions for the linear stability computations are the same except at the inflow boundary, where the velocity components are set to zero. The results from the linear stability analysis are discussed in the chapter 5. The colour map used in some of the figures is based on the following convention: the red colour denotes a positive value with the dark red being the highest, while the blue colour represents a negative value with the dark blue being the lowest; the white background corresponds to a zero value.

4.1.2 Non-dimensional parameters

The Reynolds number is based on the major axis of the ellipse and defined as $Re = U(2a)/\nu$, where U is the oncoming uniform flow speed and ν is the kinematic viscosity. Semi-major axis of the ellipse is taken as the length scale for presenting the results. The aspect ratio defined earlier is the ratio of the semi-minor axis to the semi-major axis, i.e. $Ar = b/a$. All the results presented here are with respect to the nondimensional time $\tau = U\,t/(2a)$, where t is the dimensional time. Strouhal number, St, is defined as $f(2a)/U$, where f is the dimensional frequency. For linear stability analysis, St corresponding to eigenmodes is given by the equation 4.1.

$$St = \frac{\lambda_i(2a)}{2\pi \mathrm{U}} \tag{4.1}$$

where λ_i is the imaginary part of the eigenmode and $\frac{\lambda_i}{2\pi}$ represents the frequency of oscillation.

4.1.3 Mesh convergence study

For conducting the mesh convergence study, we use three different mesh types: M1, M2 and M3. These correspond to progressively increasing resolution. Also, we use two different domain sizes (H = 100, 10). While varying H, we ensure that the resolution of the mesh does not change. We, therefore, identify a mesh by (M, H) pair. For example, (M1, H = 100) represents the mesh having the lowest resolution and the domain with H = 100. The number of nodes (NN) and the number of elements (NE) corresponding to the meshes (M1, H = 100), (M2, H = 100) and (M3, H = 100) are (NN = 249165, NE = 247654), (NN = 301120, NE = 299504)

Table 4.1: Effect of mesh resolution on the steady flow characteristics (bubble length (L_B), bubble width (W_B), drag coefficient (C_D) and rear stagnation pressure (C_{pb})) is presented for $Re = 150$ flow in the domain with $H = 100$. Three different resolutions, M1, M2 and M3, are used. Here. $\delta = |\max\%$ difference$|$ in the numerical data is with respect to M1.

Ar	M1	M2	M3	δ	M1	M2	M3	δ
	L_B				W_B			
1.0	18.7355	18.7302	18.7255	0.0534	3.4499	3.4484	3.4480	0.0533
0.75	23.0025	22.9954	22.9917	0.0472	4.0368	4.0363	4.0349	0.0484
0.5	29.0813	29.0766	29.0675	0.0474	4.8740	4.8739	4.8744	0.0117
0.375	33.1450	33.1367	33.1299	0.0456	5.4380	5.4401	5.4408	0.0511
0.25	38.1872	38.1783	38.1642	0.0601	6.1498	6.1502	6.1511	0.0215
0.125	44.5812	44.5610	44.5431	0.0854	7.0832	7.0811	7.0823	0.0297
0.0625	48.4905	48.4544	48.4231	0.1391	7.6920	7.6898	7.6879	0.0532
0.03	50.8603	50.7964	50.7499	0.2170	8.0800	8.0756	8.0721	0.0983
0.01	52.5286	52.4461	52.3879	0.2679	8.3672	8.3556	8.3504	0.2011
	C_D				C_{pb}			
1.0	0.9215	0.9214	0.9213	0.0213	-0.3338	-0.3339	-0.3339	0.0285
0.75	0.9582	0.9581	0.9580	0.0219	-0.3320	-0.3321	-0.3321	0.0214
0.5	1.0067	1.0066	1.0065	0.0192	-0.3225	-0.3225	-0.3225	0.0192
0.375	1.0368	1.0367	1.0366	0.0176	-0.3145	-0.3145	-0.3145	0.0177
0.25	1.0720	1.0718	1.0718	0.0173	-0.3042	-0.3042	-0.3043	0.0169
0.125	1.1135	1.1134	1.1133	0.0229	-0.2914	-0.2914	-0.2915	0.0197
0.0625	1.1380	1.1378	1.1377	0.0283	-0.2837	-0.2838	-0.2838	0.0356
0.03	1.1534	1.1531	1.1530	0.0304	-0.2791	-0.2792	-0.2793	0.0630
0.01	1.1660	1.1655	1.1651	0.0758	-0.2758	-0.2760	-0.2760	0.0847

Table 4.2: Effect of mesh resolution on the steady flow characteristics (L_B, W_B, C_D and C_{pb}) is presented for $Re = 150$ flow in the domain with $H = 10$. Three different resolutions, M1, M2 and M3, are used. Here. $\delta = |\max\%$ difference$|$ in the numerical data is with respect to M1.

Ar	M1	M2	M3	δ	M1	M2	M3	δ
		L_B				W_B		
1.0	16.0322	16.0332	16.0305	0.0165	3.0702	3.0698	3.0680	0.0726
0.75	19.1794	19.1801	19.1773	0.0147	3.4595	3.4595	3.4593	0.0072
0.5	23.3953	23.3962	23.3933	0.0127	3.9426	3.9416	3.9420	0.0231
0.375	26.0647	26.0642	26.0632	0.0060	4.2228	4.2232	4.2223	0.0209
0.25	29.2441	29.2421	29.2391	0.0169	4.5316	4.5299	4.5276	0.0873
0.125	33.1023	33.0976	33.0925	0.0296	4.8699	4.8716	4.8740	0.0827
0.0625	35.3882	35.3731	35.3629	0.0716	5.0563	5.0562	5.0521	0.0840
0.03	36.7499	36.7221	36.7032	0.1271	5.1598	5.1591	5.1581	0.0329
0.01	37.6961	37.6602	37.6325	0.1690	5.2253	5.2279	5.2264	0.0499
		C_D				C_{pb}		
1.0	1.1116	1.1113	1.1112	0.0334	-0.5146	-0.5146	-0.5146	0.0086
0.75	1.1893	1.1891	1.1890	0.0315	-0.5539	-0.5540	-0.5540	0.0101
0.5	1.3024	1.3022	1.3020	0.0262	-0.6028	-0.6028	-0.6029	0.0116
0.375	1.3781	1.3779	1.3778	0.0233	-0.6326	-0.6326	-0.6327	0.0132
0.25	1.4717	1.4715	1.4713	0.0222	-0.6673	-0.6673	-0.6674	0.0138
0.125	1.5893	1.5890	1.5888	0.0305	-0.7084	-0.7084	-0.7085	0.0086
0.0625	1.6615	1.6610	1.6607	0.0494	-0.7323	-0.7322	-0.7322	0.0088
0.03	1.7065	1.7056	1.7052	0.0743	-0.7463	-0.7461	-0.7460	0.0356
0.01	1.7407	1.7393	1.7384	0.1311	-0.7560	-0.7557	-0.7556	0.0546

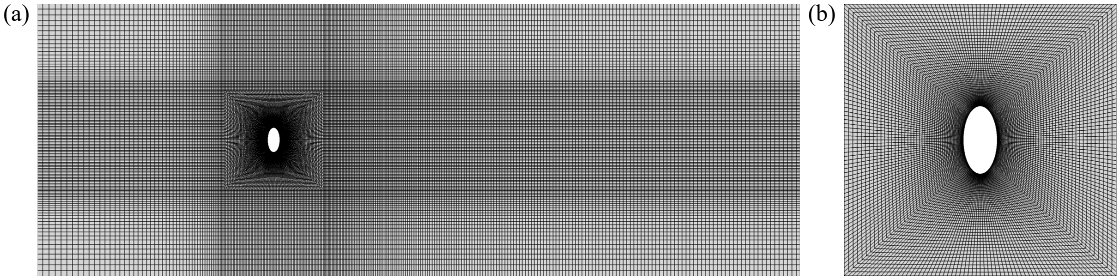

Figure 4.2: Flow past an elliptic cylinder: (a) the finite-element mesh with resolution M1 and the domain half-width $H = 100$, consisting of 249165 nodes and 247654 quadrilateral elements. (b) close-up view of the mesh.

and (NN = 370125, NE = 368354), respectively. The same for (M1, $H = 10$), (M2, $H = 10$) and (M3, $H = 10$) are (NN = 147857, NE = 146432), (NN = 177820, NE = 176304) and (NN = 214917, NE = 213262), respectively.

Figure 4.2 shows the element distribution of the non-uniform finite-element mesh M1 used for the domain with $H = 100$. The mesh consists of 249165 nodes and 247654 bilinear quadrilateral elements. The elements that lie close to the cylinder have a relatively small height, normal to the surface of the cylinder, to resolve the boundary layer and separating shear layer. The mesh is more refined in the downstream direction, and the element size gradually increases as we move away from the cylinder. The cylinder is placed at the centre of the mesh inside a square box consisting of radial and circumferential grid lines. Outside the box, the elements are rectangular.

Results from the mesh convergence study of the steady flow characteristics (L_B, W_B, C_D and C_{pb}) are shown in tables 4.1 and 4.2. The maximum % differences shown in the tables are with respect to the results from M1. We can see that for the domain with $H = 100$ (table 4.1), the maximum % difference in the numerical data for L_B, W_B, C_D and C_{pb} are 0.2679, 0.2011, 0.0758 and 0.0847, respectively. The same for $H = 10$ (table 4.2), are 0.1690, 0.0873, 0.1311 and 0.0546, respectively. The % difference, even though increases with decrease in Ar, remains extremely small throughout. We, therefore, keep the mesh resolution for all our calculations same as M1.

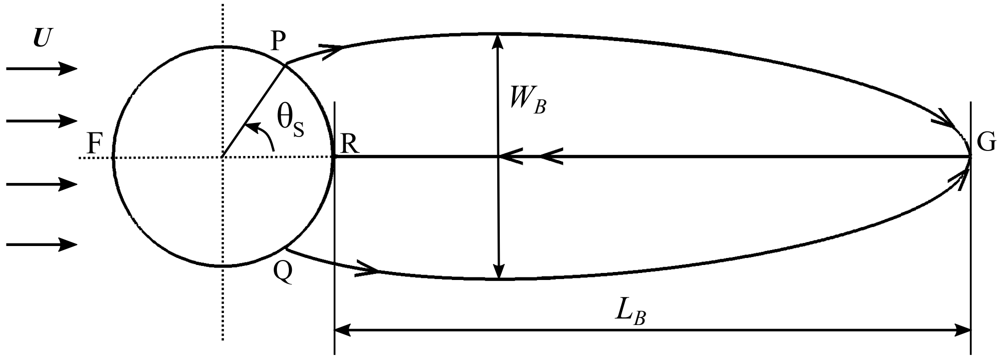

Figure 4.3: Schematic representation of the symmetric wake bubble: separation angle θ_S, bubble length L_B, bubble width W_B, front stagnation point F, rear stagnation point R, wake stagnation point G and the separation points P and Q.

4.2 Steady flow results

Here, we present the results for steady flow past an elliptic cylinder placed normal to the incoming flow. It is known that beyond a certain Re, the flow past an elliptic cylinder separates from the surface of the cylinder (Dennis & Young [28]), resulting in the formation of the wake bubble. Figure 4.3 shows a schematic diagram of the wake bubble. The separation angle, θ_S, is measured in the anticlockwise direction from the rear stagnation point R. The bubble length, L_B, is defined as the distance measured along the wake centerline between the rear stagnation point R and the wake stagnation point G. The bubble width, W_B, is the maximum distance between the upper and lower separation streamlines.

We present the variation of the steady flow characteristics like bubble length, bubble width, separation angle, drag coefficients, surface pressure, and vorticity distribution on the surface of the cylinder with the parameters Ar, Re, and H. The steady flow results are computed for (nine) different Ar, five different H and for Re values ≤ 200. The separation Reynolds number for each aspect ratio is determined for varying H. The equations for the best fit through the data are also proposed to show the steady flow behaviour with varying Ar, Re, and H. For better presentation and analysis, we first discuss the results obtained for the domain with $H = 100$. Later, we show the effect of blockage on the flow characteristics.

Table 4.3: Comparison of the steady flow characteristics (L_B, W_B, C_D and ω_{max}) for flow past a circular cylinder with those reported by Fornberg [2]. The present data are computed using the domain with $H = 100$.

	Fornberg [2]				Present			
Re	L_B	W_B	C_D	ω_{max}	L_B	W_B	C_D	ω_{max}
100	12.2	2.88	1.060	9.0	12.2941	2.8875	1.0651	9.0308
200	25.2	4.00	0.831	12.4	25.4212	4.0247	0.8352	12.3380

4.2.1 Results for the domain with $H = 100$ and comparison with published data

Table 4.3 shows a comparison of the bubble length, the bubble width, the drag coefficient and the maximum vorticity on the cylinder surface at $Re = 100$ and 200 for flow past a circular cylinder with those reported by Fornberg [2]. The close agreement amongst the results is clearly visible. Table 4.4 compares the steady flow separation angle and the drag coefficient for flow past a circular cylinder obtained from the present study with those published in the literature. We can see that the C_D values reported by Fornberg [48] at $Re = 100$ and 200 differ from the present results by 0.48% and 0.26%, respectively. The separation angle shows a difference of 0.31% at $Re = 100$ and 0.36% at $Re = 200$ with the recent results of Erturk & Gokcol [88]. A comparison of the steady flow characteristics for flow past an elliptic cylinder ($Ar = 0.5$) at $Re = 40$ is presented in Table 4.5. Our results match very well with those reported by Sen *et al.* [32]. We note a difference of $\approx 0.13\%$ for both L_B and θ_S, whereas the difference for C_D and C_{Dp} is less than 0.048%. The C_{Df} value agrees up to four decimal places. These observations show that the mesh resolution M1 used here is suitable for conducting the present study.

Figure 4.4 shows the vorticity field and the wake bubble computed at $Re = 150$ and 200 for different aspect ratios of the cylinder. The strength of vorticity in the shear layer increases with increase in Re/decrease in Ar. This causes the wake bubble to grow longer and wider. Therefore, the length and width of the bubble increase with the decrease in Ar/increase in Re. The variation of the bubble length with Re is plotted in figure 4.5. The bubble length is determined by locating

Table 4.4: Comparison of θ_S and C_D for flow past a circular cylinder at $Re = 100$ and 200 with earlier studies. The present results are obtained using the domain with $H = 100$.

	θ_S		C_D	
Studies \ *Re*	100	200	100	200
Son & Hanratty [89]	–	75°	–	0.924
Jain & Rao [23]	65°	74°	1.230	1.06
Dennis & Chang [24]	66.2°	–	1.056	–
Collins & Dennis [90]	65.4°	–	1.15	–
Patel [91]	66.06°	75.07°	1.1119	0.9485
Fornberg [25]	67.47°	74.92°	1.058	0.829
Fornberg [48]	–	–	1.060	0.833
Erturk & Gokcol [88]	66.084°	74.561°	–	–
Present	65.878°	74.291°	1.0652	0.8352

Table 4.5: Comparison of L_B, θ_S, C_D and its components (C_{Dp} and C_{Df}) for flow past an elliptic cylinder ($Ar = 0.5$) at $Re = 40$ with earlier studies. The present results are shown for the domain with $H = 100$.

Studies	L_B	θ_S	C_{Dp}	C_{Df}	C_D
Sivakumar *et al.* [30]	6.5488	–	1.2289	0.3278	1.5567
Sen *et al.* [32]	6.5531	76.49°	1.2443	0.3228	1.5671
Present	6.5442	76.59°	1.2437	0.3228	1.5665

the point along the wake centerline where the stream-wise velocity goes to zero. From figure 4.5, we see that the relative increase in L_B with Re is more for low Ar cylinders. In fact, the increase is linear for $Ar = 1.0$ and 0.75. For $0.01 \leq Ar \leq 0.5$, the curves show a non-linear growth. The reason for this is that the strength of the

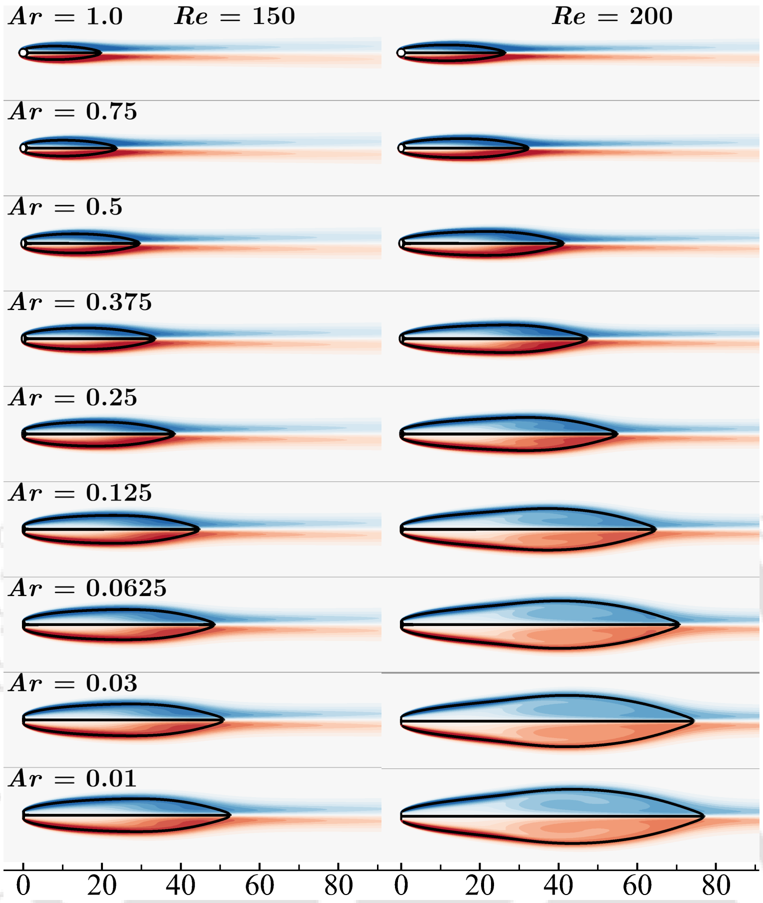

Figure 4.4: Vorticity field for flow past elliptic cylinders of different Ar at $Re = 150$ and 200 computed using the domain with $H = 100$. Streamlines (in black) show the symmetric wake bubble. The vorticity field is plotted in the range -0.4 to 0.4.

vorticity in the top and the bottom shear layers rapidly increase with Re for low Ar cylinders. This is further demonstrated by obtaining the best (least-square) fit equations from the data. Table 4.6 presents the best fit equations. The equations are linear for $Ar = 0.75$ and 1. For $0.01 \leq Ar \leq 0.5$, second order polynomials better fit the data. Here, we should note that, though the coefficients of Re^2 are very small, the contribution of the second order term becomes significant at higher Re.

For $Ar = 1.0$, several researchers (Smith [38], Chernyshenko [39]) in the past theoretically predicted the linear variation of L_B with Re. Sen *et al.* [1] numerically computed the steady flow for Re in the range 6-40 and proposed the equation $0.1336Re$ - 0.847 for L_B versus Re. Comparing this with the equation for $Ar = 1.0$

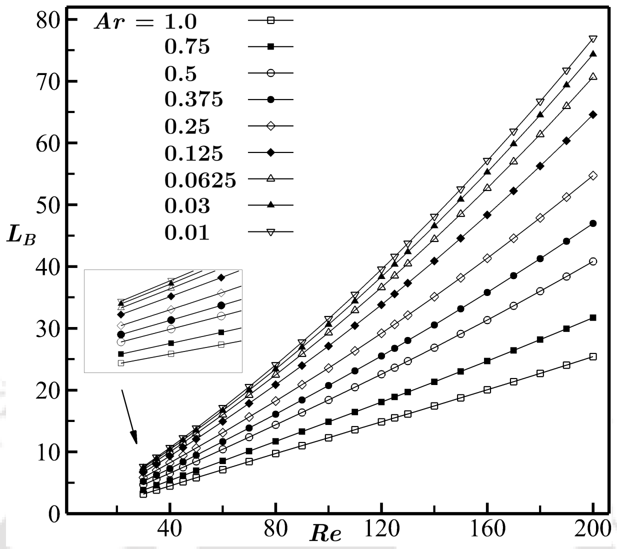

Figure 4.5: Variation of L_B with Re for cylinders of different Ar placed in the domain with $H = 100$.

Table 4.6: The least-square fit of the bubble length data (for $30 \leq Re \leq 200$, $H = 100$) shown in figure 4.5. The maximum % difference (over the Re range) between the actual data and the value obtained from the corresponding empirical equation is also mentioned.

Ar	Empirical equations	|max % difference|
1.0	$0.1301\ Re - 0.7155$	0.88
0.75	$0.1628\ Re - 1.2710$	5.35
0.5	$0.0002\ Re^2 + 0.1726\ Re - 0.5972$	2.66
0.375	$0.0002\ Re^2 + 0.1883\ Re - 0.5913$	4.09
0.25	$0.0003\ Re^2 + 0.2068\ Re - 0.5864$	3.53
0.125	$0.0005\ Re^2 + 0.2288\ Re - 0.5808$	1.08
0.0625	$0.0006\ Re^2 + 0.2416\ Re - 0.5784$	1.54
0.03	$0.0006\ Re^2 + 0.2495\ Re - 0.5827$	1.37
0.01	$0.0007\ Re^2 + 0.2551\ Re - 0.5861$	1.95

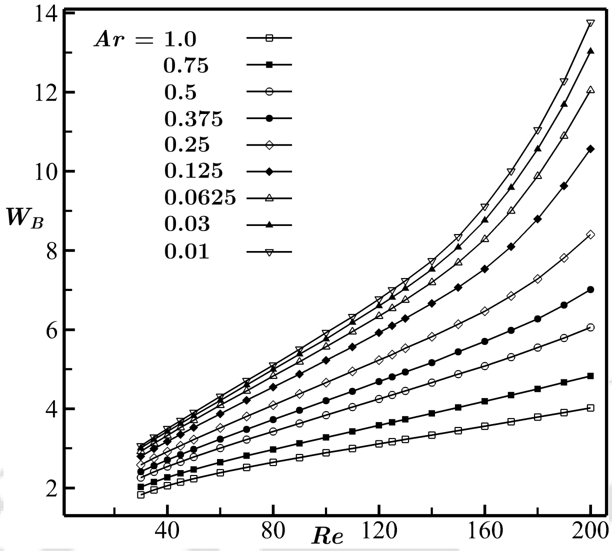

Figure 4.6: Variation of W_B with Re for cylinders of different Ar placed in the domain with $H = 100$.

shown in table 4.6, we find that the slope for L_B versus Re matches up to second decimal place. Since the range of Re used for obtaining the best fit equation in our case is different from that for Sen *et al.* [1], we find the equations slightly different. Despite this, the data obtained from the present equation and from the one proposed by Sen *et al.* [1] agree quite well down to $Re = 20$.

Figure 4.6 shows the variation of bubble width with Re for cylinders of different aspect ratio. The bubble width shows a non-linear growth with increase in Re. A relatively large growth is observed for low Ar cylinders. As it is true with L_B, the rapid increase in the strength of vorticity (see figure 4.4) in the shear layers for low Ar cylinder causes W_B to increase rapidly. Table 4.7 presents the least-square fit equations for W_B. For $Ar = 1.0$, W_B varies linearly with $Re^{0.5}$. This trend agrees with the theoretical predication made by Smith [38]. The numerical study by Peregrine [50] and Fornberg [48] also show that for $Ar = 1.0$, W_B varies linearly with $Re^{0.5}$ up to $Re = 300$. Beyond this, they predict a quadratic variation with $Re^{0.5}$. The order of polynomial in the best fit equations increases with decrease in Ar. For $Ar = 0.75$ and 0.5, second order (in $Re^{0.5}$) polynomials are required to obtain the best fit, whereas for $0.01 \leq Ar \leq 0.375$, the best fit polynomials are of third order (in $Re^{0.5}$).

The formation of wake bubble begins with the flow separation from the surface of

Table 4.7: The least-square fit of the bubble width data (for 30$\leq$ Re $\leq$200, H = 100) shown in figure 4.6. The maximum % difference (over the Re range) between the actual data and the value obtained from the corresponding empirical equation is also mentioned.

Ar	Empirical equations	$\lvert$max % difference$\rvert$
1.0	$0.2444\ Re^{0.5} + 0.4788$	2.22
0.75	$0.0113\ Re + 0.0927\ Re^{0.5} + 1.2233$	2.06
0.5	$0.0212\ Re + 0.0063\ Re^{0.5} + 1.6492$	2.49
0.375	$0.0037\ Re^{1.5} - 0.0787\ Re + 0.9316\ Re^{0.5} - 0.9656$	1.10
0.25	$0.0074\ Re^{1.5} - 0.1699\ Re + 1.7282\ Re^{0.5} - 3.0629$	2.42
0.125	$0.0148\ Re^{1.5} - 0.3549\ Re + 3.3081\ Re^{0.5} - 7.2331$	4.56
0.0625	$0.0200\ Re^{1.5} - 0.4852\ Re + 4.3987\ Re^{0.5} - 10.0823$	6.38
0.03	$0.0236\ Re^{1.5} - 0.5715\ Re + 5.1121\ Re^{0.5} - 11.9250$	6.62
0.01	$0.0267\ Re^{1.5} - 0.6499\ Re + 5.7711\ Re^{0.5} - 13.6637$	7.41

the cylinder. The Re at the onset of separation is the separation Reynolds number (Re_S). We compute Re_S for cylinders of different Ar. There are several ways (Paul *et al.* [33]) to determine Re_S. Srinivasan [92] determined the Re_S from the velocity field. He found that the value of $\frac{\partial^2 u}{\partial x^2}$ varies linearly with Re in the neighbourhood of Re_S, and at $Re = Re_S$, the value of $\frac{\partial^2 u}{\partial x^2}$ becomes zero at the rear stagnation point. We use the same criterion to obtain Re_S. The value of $\frac{\partial^2 u}{\partial x^2}$ is obtained using central differencing. The calculation of Re_S is validated with the data from Sen *et al.* [1] shown in figure 4.7. For $Ar = 1.0$, they report $Re_S = 6.30$, which is very close to the present value of 6.2975. For $Ar = 0.5$, Sen *et al.* [32] obtained $Re_S = 3.02$ which matches well with the present value of 3.0312. The linear variation of $\frac{\partial^2 u}{\partial x^2}$ with Re, close to Re_S, is observed for all Ar. Figure 4.8 shows the variation of Re_S with Ar. The value of Re_S monotonically decreases with decrease in Ar. This happens because, at a given Re, the adverse pressure gradient on the rear face is higher for low Ar cylinders. This leads to flow separation at low Re.

The linear variation of Re_S is observed for 0.125$\leq$ Ar $\leq$ 1.0. The best fit equation

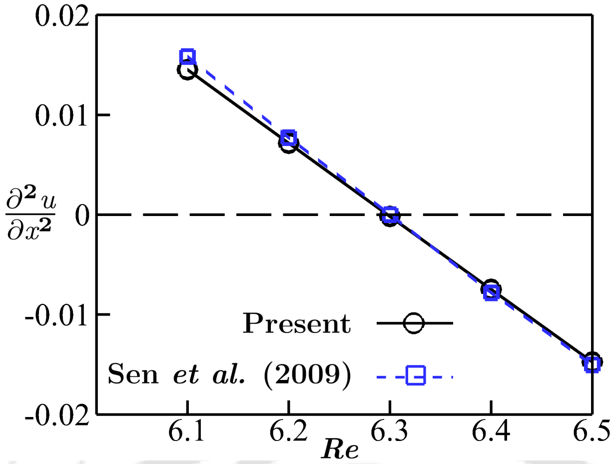

Figure 4.7: Variation of $\frac{\partial^2 u}{\partial x^2}$ at the rear stagnation point with Re for the steady flow past a circular cylinder. The numerical results from Sen *et al* [1] are compared with the present results.

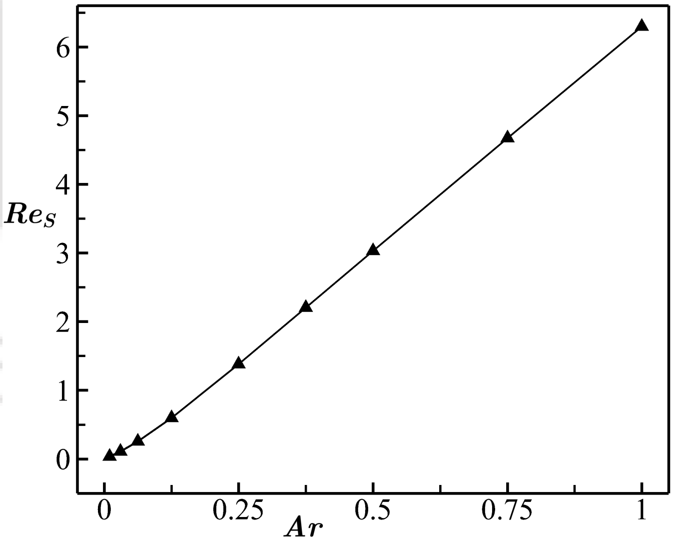

Figure 4.8: Variation of Re_S with Ar for the domain with $H = 100$.

for predicting Re_S for this range of Ar is given by equation 4.2. The predicted value obtained from equation 4.2 has maximum and average percentage difference of 3.12 and 0.83, respectively, with the actual data.

$$Re_S = 6.5355\ Ar - 0.2371 \tag{4.2}$$

The non-linear variation of Re_S is observed for $0.01 \leq Ar \leq 0.0625$. The best fit

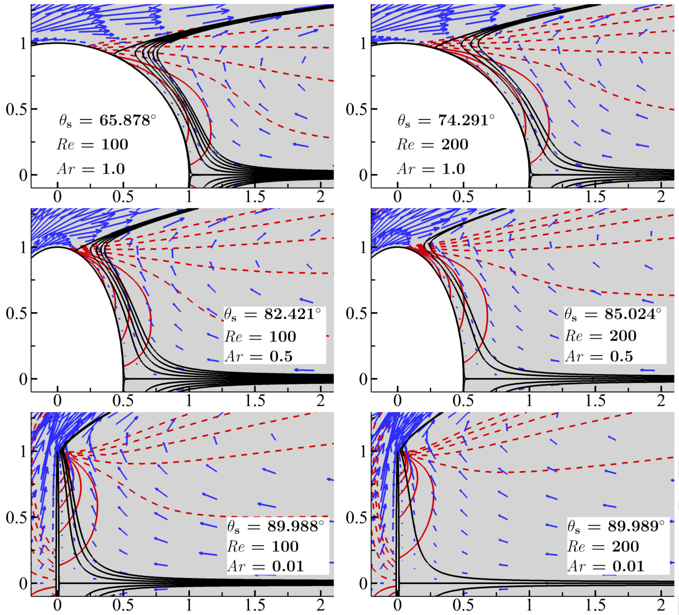

Figure 4.9: Separation angle (θ_s) at $Re = 100$ and 200 for cylinders with $Ar =$ 1.0, 0.5 and 0.01 placed in the domain with $H = 100$. The solid black lines display the streamlines and blue arrows show velocity vectors. The solid and dotted red lines show the positive and negative vorticity contours, respectively. The separation point is marked on the cylinder surface where the vorticity changes its sign from negative to positive. The vorticity contours are plotted in the range -1.0 to 1.0.

equation for this range of aspect ratio is given by equation 4.3. The maximum and average percentage difference between the actual value and the value obtained from the proposed equation are 0.081 and 0.039, respectively.

$$Re_S = 16.9084\ Ar^2 + 2.9837\ Ar + 0.0028 \tag{4.3}$$

As Re increases beyond Re_S, the point of separation moves on the surface of the cylinder away from the rear stagnation point. Since the steady flow is symmetric, there exists two separations points located symmetrically about the wake centerline. The separation point is located by marking the separation angle (θ_s). θ_s is determined by identifying the point on the cylinder surface where vorticity or shear stress is zero. Sen *et al.* [1] compared the angle obtained for zero vorticity with the same for zero shear stress and found both to be equal. Figure 4.9 shows θ_s for a few cases along with the streamline and vorticity contours. The point where the positive and

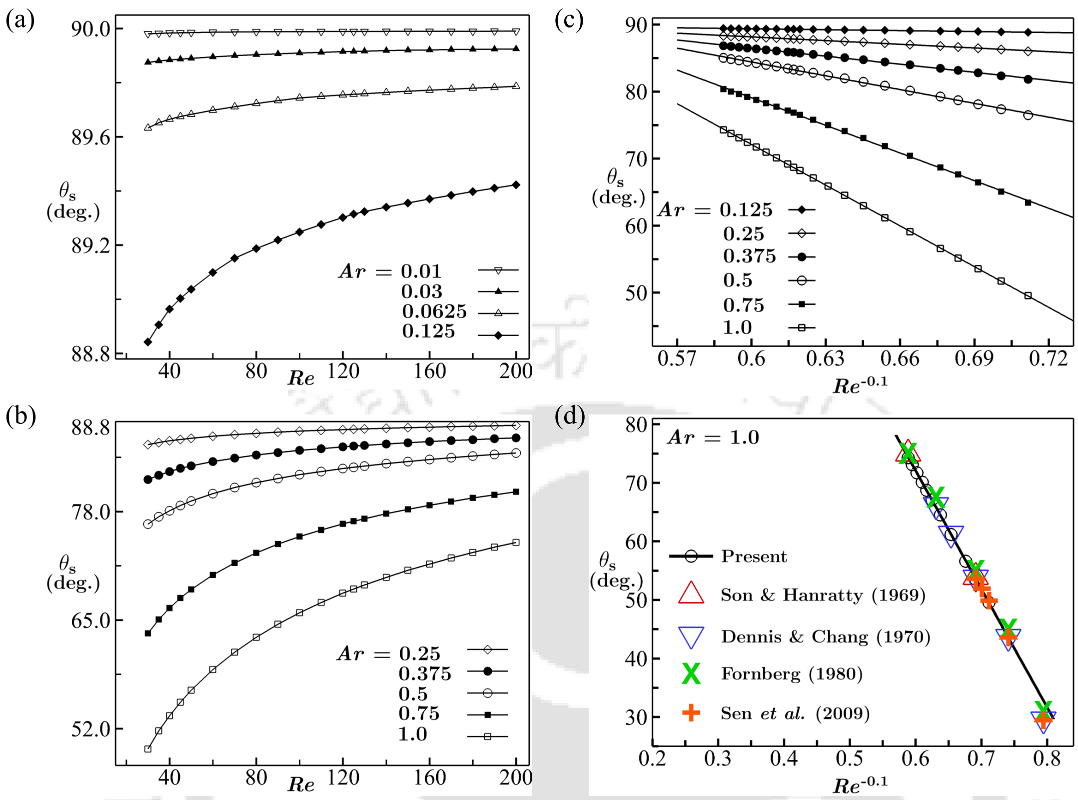

Figure 4.10: Variation of θ_s with Re for (a) $0.01 \leq Ar \leq 0.125$, (b) $0.25 \leq Ar \leq 1.0$. (c) linear fit of θ_s versus $Re^{-0.1}$, (d) comparison between previous results and present numerical data along with the linear fit equation (black line) for $Ar = 1.0$. The present results are for the domain with $H = 100$.

negative vorticity contours ”meet” (come close) is clearly visible. The separation streamline can also be seen. The separation angle presented here is obtained by the linear interpolation of the surface vorticity between adjacent points which have positive and negative vorticity. As expected, figure 4.9 shows that the separation point moves upstream with an increase in Re. This upstream shift is observed for all Ar.

Figures 4.10 (a) and (b) show the variation of θ_s with Re for cylinders of different Ar. For better presentation, the curves are separated in parts (a) and (b). θ_s monotonically increases with increase in Re/decrease in Ar. Close to Re_S, the increase in θ_s with Re is gradual for high Ar cylinders and rapid for low Ar cylinders. Although not shown here, the separation angle increases rapidly for low Ar cases and reaches close to 90°. After this, it remains more or less unchanged with increase in Re. At relatively higher Re, as shown in figure 4.10 (a) and (b), the increase in θ_s with Re is comparatively large for higher Ar cylinders. The least-square fit of the separation angle data for $0.125 \leq Ar \leq 1.0$ can be represented in the form $\theta_s = \mathrm{A}Re^{-0.1} + \mathrm{B}$. The values of A and B depend on the aspect ratio and are presented in equation 4.4. The maximum percentage difference in the actual data and the value obtained from the best fit equation is 0.88. The average of the differences is less than 0.43%. For $0.01 \leq Ar \leq 0.0625$, θ_s varies little and lies between 89.63° to 89.98°.

$$\left.\begin{aligned} \mathrm{A} &= -773.30Ar^{0.7} + 763.48Ar^{0.35} - 193.46 \\ \mathrm{B} &= \quad 390.22Ar^{0.7} - 380.90Ar^{0.35} + 185.13 \end{aligned}\right\} \tag{4.4}$$

For $Ar = 0.5$, Sen *et al.* [32] reported θ_s equal to 78.10° and 76.49° at Re = 30 and 40, respectively. These values match very well with 78.20° and 76.59° for the corresponding Reynolds numbers, from the present calculation. Wu *et al.* [93] conducted a comprehensive study for flow past a circular cylinder with Re in the range 7-200. They presented the time-average separation angle, boundary layer thickness and Strouhal number, all, as a function of $Re^{-0.5}$. Sen *et al.* [1] presented θ_s for flow past a circular cylinder as a function of $Re^{-0.5}$ in the range $10 \leq Re \leq 40$. In the present study, we find that the separation angle is better represented as a function of $Re^{-0.1}$, for $30 \leq Re \leq 200$ and $0.125 \leq Ar \leq 1.0$. Figure 4.10 (c) shows the linear fit curves for θ_s as a function of $Re^{-0.1}$. In figure 4.10 (d), we show that for $Ar = 1.0$, θ_s from previous studies lie on the proposed linear fit equation presented as a function of $Re^{-0.1}$. The black solid line represents the linear fit equation and the symbols display the actual numerical data. The previous results and present data are found to be in excellent agreement except for $Re \leq 30$.

In bluff body flows, there is a significant contribution of pressure drag to the total drag on the body. The pressure drag is the integral effect of pressure distribution on the body surface. Pressure is represented in the non-dimensional form as C_p (pressure coefficient) = $\frac{p-p_\infty}{\frac{1}{2}\rho U^2}$. Here p_∞ is the free-stream pressure. C_p distribution along the cylinder surface varies with Re as well as Ar. We define C_{p0} and C_{pb} as the front stagnation pressure coefficient (θ = 0°) and base pressure coefficient (θ = 180°), respectively. Figure 4.11 shows the variation of C_p distribution with Re for Ar = 1.0, 0.5 and 0.01. From our computations, it is found that the smooth variation of C_p along the cylinder surface exists for $Ar \geq 0.375$. In general, C_p

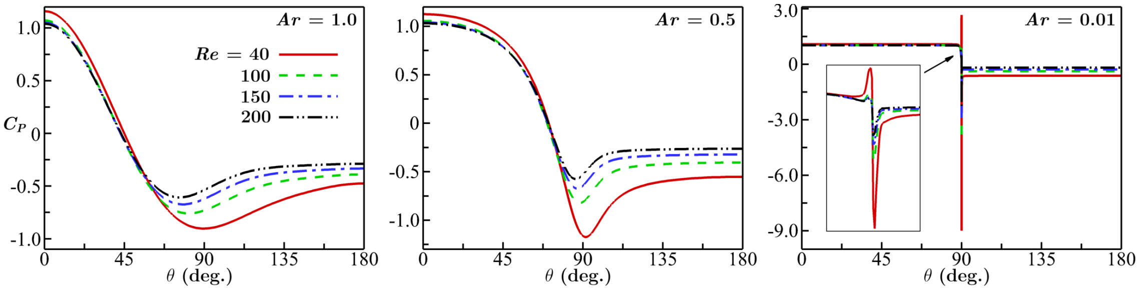

Figure 4.11: C_p distribution on the surface of elliptic cylinders (Ar = 1.0, 0.5 and 0.01) plotted for different Re. These results are for the domain with H = 100.

Table 4.8: Front stagnation pressure (C_{p0}), rear stagnation pressure (C_{pb}), minimum surface pressure ($C_{p_{min}}$) and $C_{p_{min}}$ location (θ_m) are presented with decreasing Ar at two different Re. The results are presented for the domain with H = 100.

	C_{p0}	C_{pb}	$C_{p_{min}}$	θ_m	C_{p0}	C_{pb}	$C_{p_{min}}$	θ_m
Ar	Re = 40				Re = 100			
1.0	1.1590	-0.4754	-0.9035	90.00	1.0717	-0.3893	-0.7601	81.81
0.75	1.1425	-0.5123	-1.0082	91.02	1.0638	-0.4009	-0.7887	84.87
0.5	1.1247	-0.5527	-1.1734	91.36	1.0555	-0.4051	-0.8225	87.95
0.375	1.1153	-0.5731	-1.3211	91.53	1.0513	-0.4033	-0.8588	89.48
0.25	1.1053	-0.5928	-1.6055	91.02	1.0469	-0.3986	-0.9527	90.34
0.125	1.0948	-0.6105	-2.4677	90.34	1.0425	-0.3904	-1.3154	90.17
0.0625	1.0892	-0.6181	-4.2898	90.08	1.0402	-0.3848	-2.1547	90.08
0.03	1.0862	-0.6213	-8.4914	90.04	1.0390	-0.3813	-3.9593	90.04
0.01	1.0842	-0.6230	-8.9985	90.01	1.0383	-0.3787	-4.0286	90.01

gradually decreases as we move on the surface of the cylinder, reaches minimum around θ equal to 90°, and then continues to increase till the rear stagnation point. As we decrease Ar, the fall in the C_p becomes sharp around θ close to 90°. For Ar = 0.03 and 0.01, we find a sharp rise in C_p before the fall. In addition, it remains more or less constant except around θ close to 90°. This variation is depicted for

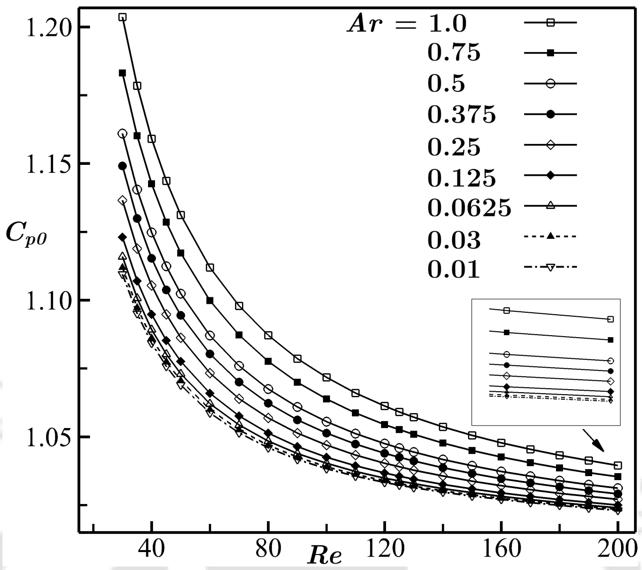

Figure 4.12: Variation of C_{p0} with Re for cylinders of different aspect ratios computed in the domain with H = 100.

Ar = 0.01 in figure 4.11. From the figure, we notice that for Ar = 0.01, at Re = 40, the maximum pressure on the cylinder surface occurs at θ = 89.97°, not at the front stagnation point. Similar observations were made by Sen [34] for Ar = 0.2 at very low Re. A detailed explanation of this behaviour is presented therein.

C_p distribution gives us some idea about the generation of pressure drag by the flow. Table 4.8 presents the variation of C_{p0}, C_{pb}, $C_{p_{min}}$ and θ for $C_{p_{min}}$ (θ_m) with Ar at two different Re. In particular, C_{p0} and C_{pb}, are mostly discussed in the literature. For Ar = 1.0 and Re = 100, Dennis & Chang [24] reported C_{p0} = 1.060 and C_{pb} = -0.393. Both match very well with the present results given in table 4.8. A comparison with the results of Sen [34] for Ar = 0.2 and Re = 40 shows an excellent agreement. The values of C_{p0} and C_{pb} from our calculation are 1.1012 and -0.6003, respectively. The same reported by Sen [34] are 1.1024 and -0.6006, respectively. Figure 4.12 shows the variation for C_{p0} versus Re for different Ar. We can see that C_{p0} monotonically decreases with decrease in Ar/increase in Re. At higher Reynolds numbers, the difference between C_{p0} values, for different Ar, reduces. In contrast, figure 4.13 shows that C_{pb} monotonically increases with increase in Re, for all Ar. In other words, there is enhanced pressure recovery at higher Re. As a consequence, the pressure drag decreases with increase in Re (see figure 4.14). On the other hand, the variation of C_{pb} with Ar depends on Re. For

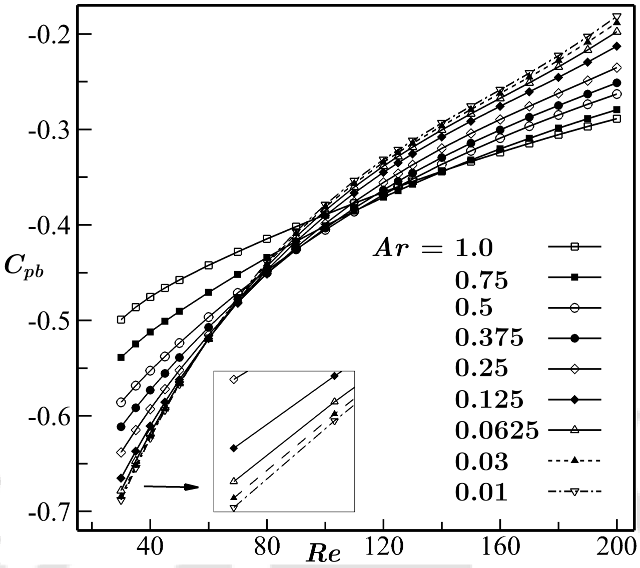

Figure 4.13: Variation of C_{pb} with Re for cylinders of different aspect ratios computed in the domain with $H = 100$.

$Re \leq 60$, C_{pb} monotonically decreases with decrease in Ar. For $60 \leq Re \leq 150$, we find a nonmonotonic variation with Ar. Further, around $Re \approx 95$, C_{pb} values are close to each other for all Ar. For $Re \geq 150$, C_{pb} monotonically increases with decrease in Ar. As already noted, the variation in C_{pb} affects the pressure drag acting on the cylinder.

The value of minimum surface pressure ($C_{p_{min}}$) and its location (θ_m) show change from a favourable pressure gradient to an adverse pressure gradient. From this point on, the pressure force acts in the direction opposite to the local flow. At a downstream location, the flow separates from the surface of the cylinder. Figure 4.11 shows that $C_{p_{min}}$ monotonically increases with increase in Re and its location moves upstream along the surface of the cylinder. This implies that the region of the favourable pressure gradient decreases, which causes the separation point to move upstream. This is one reason why the separation angle increases with increase in Re. For $Ar \leq 0.0625$, θ_m remains constant with Re.

As far as the variation with Ar is concerned, there is a decrease in $C_{p_{min}}$ with decrease in Ar. The larger negative value of $C_{p_{min}}$ indicates a higher adverse pressure gradient, which causes a stronger flow separation. The lowest value of $C_{p_{min}}$ occurs for $Ar = 0.01$. θ_m does not show much variation with Ar at lower Re. At higher Re, θ_m increases with decrease in Ar (see table 4.8). We compare $C_{p_{min}}$ and θ_m for

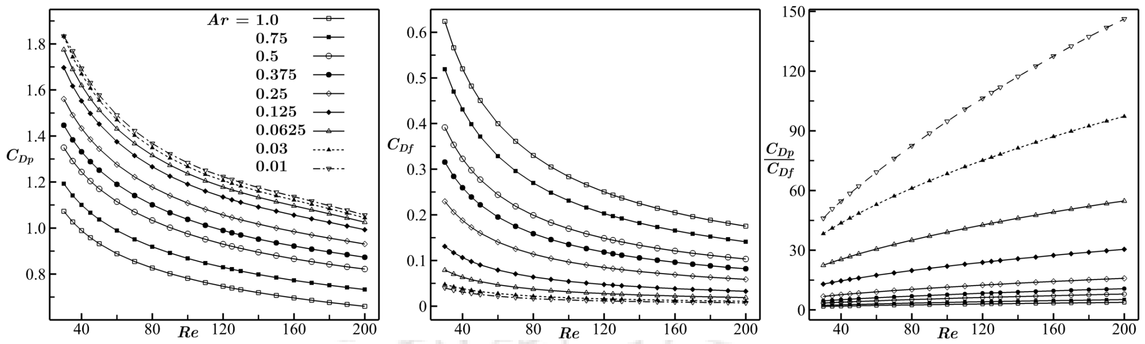

Figure 4.14: Variation of the pressure drag coefficient C_{Dp} (left), skin friction drag coefficient C_{Df} (middle) and their ratio (right) with Re for cylinders of different Ar computed in the domain with $H = 100$.

$Ar = 0.2$ and $Re = 40$ with the recent study by Sen [34]. In the present study, we found $C_{p_{min}}$ and θ_m equal to -1.8154 and 90.81°, respectively. Sen [34] reported the same as -1.8616 and 90.78°, respectively. An excellent agreement is observed.

Pressure and shear stress acting on the cylinder surface lead to a nonzero drag. The drag force in the nondimensional form is represented as the drag coefficient (C_D). It is defined as $C_D = \frac{D}{\frac{1}{2}\rho U^2 S}$, where, S = 2a × 1. The contribution of pressure to the total drag is represented in the nondimensional form as the pressure drag coefficient (C_{Dp}) and the same due to shear stress is represented as the skin friction drag coefficient (C_{Df}). Thus, $C_D = C_{Dp} + C_{Df}$. Figure 4.14 shows the variation of C_{Dp}, C_{Df} and their ratio plotted with Re for cylinders of different Ar. We can see that C_{Dp} is much larger than C_{Df}, a characteristics of bluff body flows. Further, for all Ar, C_{Dp} and C_{Df} monotonically decrease with the increase in Re. As a result, the total drag coefficient decreases with Re. This is shown in figure 4.15. Figure 4.14 shows that for constant Re, C_{Dp} monotonically increases with decrease in Ar. The percentage increase in C_{Dp} at lower Re is more than the same at higher Re. For example, at $Re = 30$, C_{Dp} for $Ar = 0.01$ is 70.86% higher compared to the same for $Ar = 1$. The difference reduces to 59.95% at $Re = 200$. Of particular interest is the overall increase of $\frac{C_{Dp}}{C_{Df}}$ with decrease in Ar. This implies that, as we move from a circular cylinder to a flat plate, the cylinder turns into a better and better bluff body. In contrast, for elongated cylinders (major axis aligned with the flow), as Ar decreases, one would expect the cylinder to behave more like a streamlined body.

Using the least square error minimization approach, C_{Dp} data shown in figure

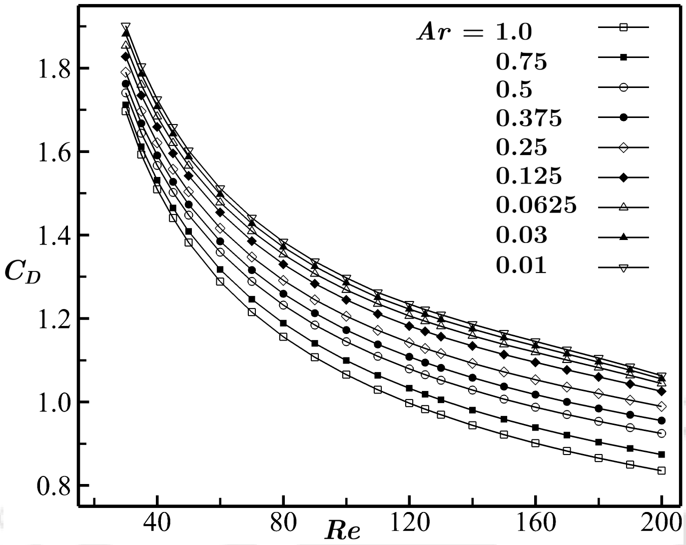

Figure 4.15: Variation of C_D with Re for cylinders of different Ar.

4.14 can be represented in the form $ARe^{-0.4} + B$. A and B depend on the aspect ratio and are given by the equation 4.5. The maximum difference in the actual data and the value obtained from the curve fit equation is 1.28%. The average difference is less than 0.45%.

$$\left.\begin{aligned} A &= -21.2901\ Ar^{0.2} + 27.2401\ Ar^{0.1} - 2.9743 \\ B &= -0.1127\ Ar^{1.6} + 0.0374\ Ar^{0.8} + 0.3752 \end{aligned}\right\} \tag{4.5}$$

For representing the best fit equation for skin friction drag, we consider two different ranges of Ar. For 0.25$\leq Ar \leq$ 1.0, C_{Df} is given as $ARe^{-0.6} + B$. A and B are given by the equation 4.6. The maximum difference in the actual data and the value obtained from the curve fit equation is 2.60%. The average difference is less than 0.80%.

$$\left.\begin{aligned} A &= 6.3568\ Ar^{0.5} - 1.2383 \\ B &= 0.0681\ Ar^{1.4} - 0.1164\ Ar^{0.7} + 0.0107 \end{aligned}\right\} \tag{4.6}$$

For 0.01$\leq Ar \leq$ 0.125, C_{Df} is represented in the form $ARe^{-0.8} + B$. A and B are given by the equation 4.7. The maximum difference in the actual data and the value obtained from the curve fit equation is 3.83%. The maximum difference occurs for $Ar = 0.01$ at $Re = 200$. The average difference is less than 1.02%.

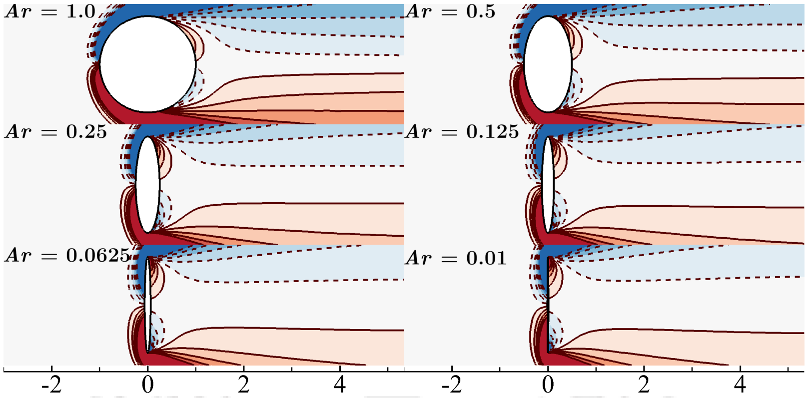

Figure 4.16: Close-up view of the vorticity contours for $Re = 100$ flow past elliptic cylinders computed in the domain with $H = 100$. Red and blue represent positive and negative values, respectively. Vorticity contours are shown in the range -1.0 to 1.0.

$$\left.\begin{aligned} \mathrm{A} &= 53.7475\ Ar^{0.2} - 70.4162\ Ar^{0.1} + 23.6643 \\ \mathrm{B} &= 0.6413\ Ar^{0.6} - 0.9766\ Ar^{0.4} + 0.5138\ Ar^{0.2} - 0.0924 \end{aligned}\right\} \tag{4.7}$$

Figure 4.15 shows that C_D monotonically decreases with increase in Re. The trend remains consistent for all Ar. For constant Re, C_D increases monotonically with decrease in Ar. Using the least square error minimization approach, C_D can be represented in the form $\mathrm{A}Re^{-0.5} + \mathrm{B}$, where A and B depend on aspect ratio and are given by the equation 4.8. The maximum difference in the actual data and the value obtained from the curve fit equation is 1.74%. The average difference is less than 0.28%.

$$\left.\begin{aligned} \mathrm{A} &= 2.5790\ Ar^{0.64} - 2.7978\ Ar^{0.32} + 7.9067 \\ \mathrm{B} &= -0.4777\ Ar^{0.64} + 0.2394\ Ar^{0.32} + 0.5285 \end{aligned}\right\} \tag{4.8}$$

Vorticity distribution around the cylinder is related to the structure of the wake and the flow separation phenomena. Figure 4.16 shows the close-up view of the vorticity field for cylinders of different Ar at $Re = 100$. We can see that the vorticity field is antisymmetric about the wake centerline. Above the wake centerline, the vorticity largely remains negative except in a small region close to the rear side of the cylinder surface. Here, vorticity has a positive sign. This is called a penetrated

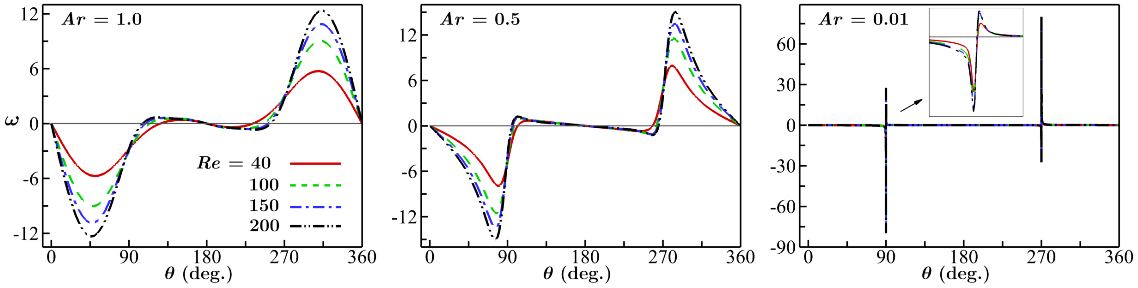

Figure 4.17: Distribution of ω on the surface elliptic cylinders plotted at different Re for the domain with $H = 100$.

vorticity. A similar region is present on the lower part of the cylinder surface. Based on the notion of penetrated vorticity, Mishra *et al.* [56] proposed following explanation for the growth of the wake. The penetrated vorticity pair cause the shear layers on either side of the cylinder to diverge away. With the decrease in Ar, the strength of the penetrated vorticity increases. As a result, the separation between the shear layers increase and the wake grows broader. The same happens with the increase in Re.

The surface distribution of the vorticity can be used to determine the separation angle (Dennis & Chang [24]). Figure 4.17 shows the vorticity distribution plotted at various Re for three different Ar. The antisymmetric distribution of surface vorticity about the base point ($\theta = 180°$) is related to the symmetry of the steady flow. For $0.125 \leq Ar \leq 1.0$, a smooth variation of vorticity exists on the cylinder surface, while for $0.01 \leq Ar \leq 0.0625$, a sharp increase in vorticity is visible close to the shoulder ($\theta = 90°$). The location between the front and the rear stagnation point where the vorticity changes sign marks the point of flow separation and the corresponding angle is the separation angle. From figure 4.17 we can see that, starting from the front stagnation point, vorticity on both sides of the cylinder surface increases in magnitude and reaches a maximum (ω_{max}) before dropping down. With the increase in Re, the location of the maximum vorticity slightly shifts upstream along the cylinder surface. With the decrease in Ar, the location of ω_{max} moves in the downstream direction toward the cylinder shoulder. For $0.01 \leq Ar \leq 0.0625$, ω_{max} appears close to the cylinder shoulder.

Figure 4.18 shows the variation of ω_{max} as a function of Re for cylinders of different aspect ratio. We can see that ω_{max} monotonically increases with increase in Re/decrease in Ar. For lower aspect ratios, there is a rapid increase in ω_{max}

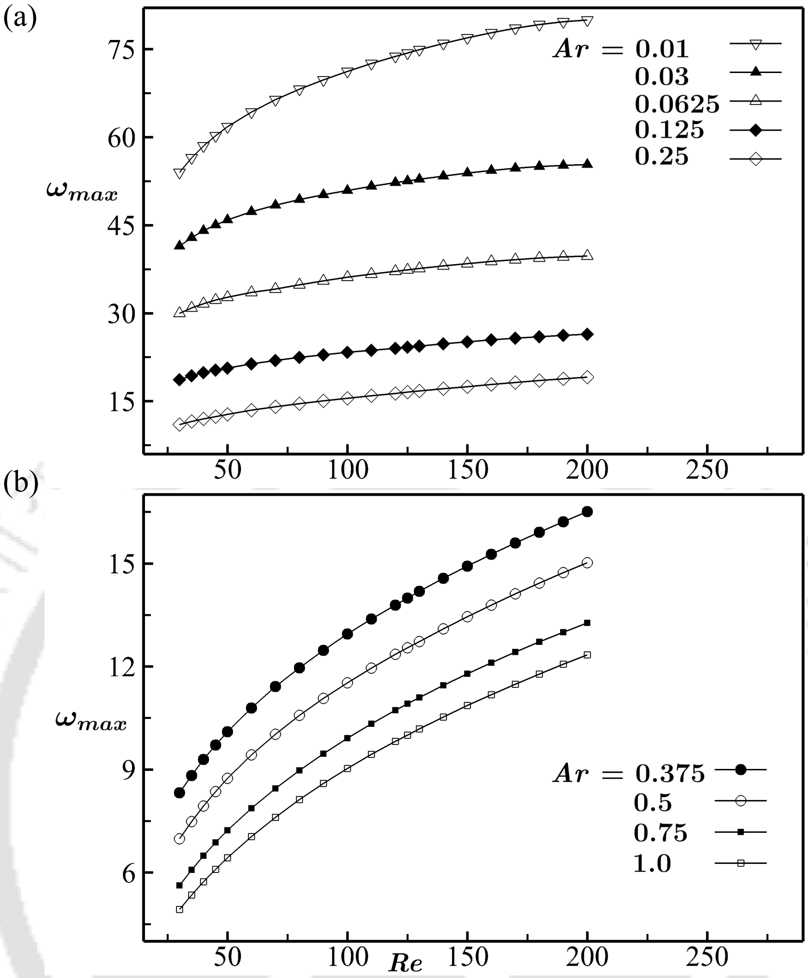

Figure 4.18: Variation of ω_{max} with Re for (a) 0.01$\leq Ar \leq 0.25$ and (b) 0.375$\leq Ar \leq$ 1.0.

with Re. A high value of ω_{max} on the cylinder surface indicates the presence of a stronger shear layer and a wider wake. Table 4.9 provides the empirical equations obtained using least-square fit to the data shown in figure 4.18. For $0.25 \leq Ar \leq 1.0$, ω_{max} is a linear function of $Re^{0.35}$. For $0.01 \leq Ar \leq 0.125$, ω_{max} is approximated by a second-degree polynomial in $Re^{0.35}$. The table also presents the maximum percentage difference, over the range of Reynolds number, between the actual data and the values evaluated from the corresponding equation. The actual data and the values estimated from the empirical equations are in very good agreement.

For $Ar = 1.0$, Sen *et al.* [1] proposed an empirical equation for ω_{max} as a function of $Re^{0.5}$ in the range $6 \leq Re \leq 40$. They extrapolated the empirical equation for

Table 4.9: Least square fit of ω_{max} data given in figure 4.18. These equations are obtained for 30$\leq$ Re $\leq$200 and H = 100.

Ar	Empirical equation	|max % difference|
1.0	$2.3980Re^{0.35} - 2.9870$	0.5375
0.75	$2.4705Re^{0.35} - 2.4859$	0.2299
0.5	$2.5744Re^{0.35} - 1.4068$	1.0899
0.375	$2.6283Re^{0.35} - 0.2540$	0.7997
0.25	$2.5855Re^{0.35} + 2.5749$	0.5374
0.125	$-0.1234Re^{0.7} + 3.6408Re^{0.35} + 8.2037$	0.8395
0.0625	$-0.2513Re^{0.7} + 5.5768Re^{0.35} + 14.5405$	0.6625
0.03	$-0.7203Re^{0.7} + 11.3912Re^{0.35} + 12.0455$	0.7500
0.01	$-1.1191Re^{0.7} + 19.1602Re^{0.35} + 3.4718$	0.7145

Re up to 400. Comparison with the results presented by Fornberg [2] and Gajjar & Azzam [3] show a good agreement for $Re \leq 100$. However, the difference between the estimated value and the numerical data increases with Re. At $Re = 400$, their results show a difference of around 15.72 % with those of Fornberg [2]. For $Re \geq 30$, the equation for ω_{max} presented in 4.9 gives better results. The extrapolation of ω_{max} for Ar = 1.0 shows an excellent agreement with Fornberg [2] in the range 30$\leq$ Re $\leq$400. At $Re = 400$, the difference between the extrapolated value and the numerical data from Fornberg [2] is 2.64 %.

4.2.2 Blockage effects

From previous studies on flow past a circular cylinder (Fornberg [2], Gajjar & Azzam [3], Sen *et al.* [1]), it has been found that the steady flow characteristics change significantly with change in blockage. Studies on flow past elliptic cylinders with blockage effects are scarce. Here, we investigate this effect on the steady flow characteristics presented in the previous section. We consider five different domain sizes (H = 10, 20, 30, 50 and 100). Table 4.10 presents a comparison of our numerical results with those of Gajjar & Azzam [3] for $Re = 100$ flow past a circular cylinder

Table 4.10: Comparison of $Re = 100$ (steady) flow past a circular cylinder results from the present study with those from Gajjar & Azzam [3].

	Gajjar & Azzam [3]				Present			
H	L_B	W_B	C_D	ω_{max}	L_B	W_B	C_D	ω_{max}
50	12.28	2.865	1.079	9.157	12.2703	2.8824	1.0760	9.1087
10	10.92	2.692	1.260	10.28	10.9098	2.7007	1.2523	10.2330

computed in domains with $H = 50$ and $H = 10$. For $H = 50$, the difference in L_B, W_B, C_D and ω_{max} are 0.08%, 0.60%, 0.28% and 0.53%, respectively. The same for $H = 10$ are 0.09%, 0.32%, 0.61% and 0.46%, respectively. These observations add credibility to our results. At this point, we would like to remind the readers that in our computations with different domain size, we keep the resolution of the mesh same as that used for computing the results with $H = 100$ (see section 4.1.3). This ensures that only the effect of blockage appears in the results. It is well known that as the lateral boundaries comes close to the cylinder their is a local flow acceleration. As a result, large velocity gradients develop in the boundary layer on the cylinder surface and in the shear layer downstream. We use fine enough mesh to capture these gradients accurately. Our comparison of the results for $H = 10$ in table 4.10 testifies this claim. The convergence study presented in section 4.1.3 with three different mesh resolution M1, M2 and M3 further strengthens this assertion.

Variation of bubble length

Figure 4.19 shows a three-dimensional surface plot of L_B as a function of Re and Ar for different H. It is observed that, for all domain sizes, L_B gradually increases with increase in Re/decrease in Ar. Figure 4.20 shows the variation of L_B with Re for different H. These are plotted for three different Ar. For $Ar = 1.0$, we can see a near linear growth for all domain sizes. As Ar decreases, L_B tends to climb rapidly for higher H. In fact, the rate of climb with respect to Re also increases, and so, the L_B versus Re curve is bent upward. This does not happen for $H = 10$. On the other hand, the nature of the variation of L_B with H depends on the flow Reynolds number. Below a certain Re, we find a nonmonotonic trend with change in H. In

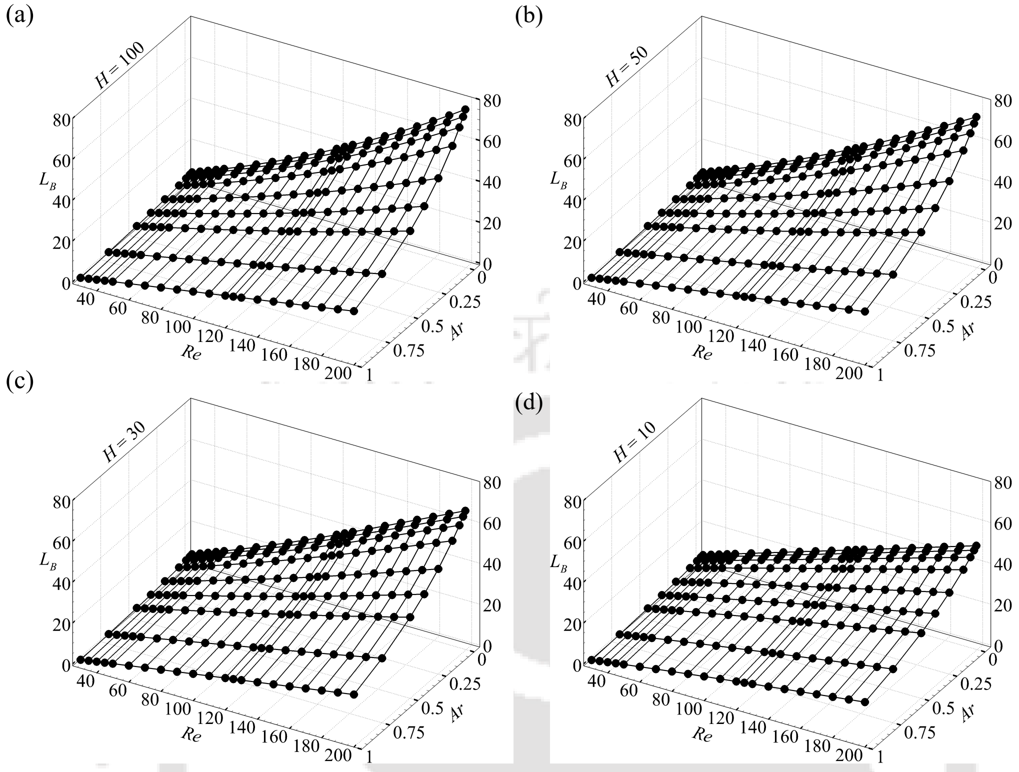

Figure 4.19: Variation of L_B with Re and Ar plotted for the domain with (a) $H = 100$, (b) $H = 50$, (c) $H = 30$ and (d) $H = 10$.

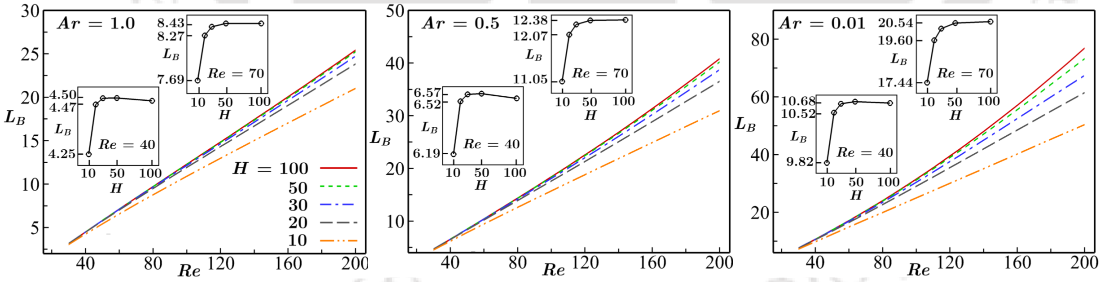

Figure 4.20: L_B versus Re for different H, plotted for $Ar = 1.0$ (left), 0.5 (middle) and 0.01 (right). The insets show the variation of L_B with H for $Re = 40$ and 70. The non-monotonic variation of bubble length with H is clearly visible.

figure 4.20 we can see the insets showing L_B versus H at $Re = 40$ and 70. The nonmonotonic change in L_B with change in H is clearly visible at $Re = 40$. Though the Reynolds number, up to which this nonmonotonic behaviour exists, depends on Ar, we find this happening below $Re = 60$. At higher Re, L_B shows monotonic

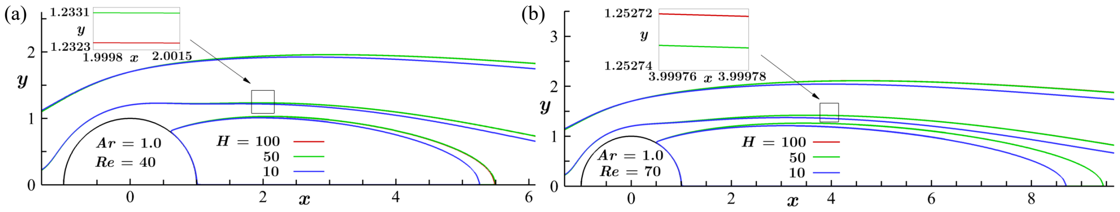

Figure 4.21: Streamline plots for flow past a circular cylinder with $H = 100$, 50 and 10 shown for (a) $Re = 40$ and (b) $Re = 70$. For all H, the two streamlines above the cylinder pass through the points (0, 1.2) and (0, 1.7). The shift in the streamline plots for different H shows the effect of blockage.

change with H. Overall, there is significant reduction in the bubble length with decrease in H. For example, $Re = 30$ flow past a circular cylinder shows a reduction of 3.34% in L_B, as we go down from $H = 100$ to $H = 10$. This reduction in L_B increases to 17.28% at $Re = 200$. As we decrease Ar, this effect of blockage on L_B becomes more prominent. The maximum decrease in L_B is observed for $Ar = 0.01$ at $Re = 200$, which is 34.47%. For $Ar = 1.0$, the nonmonotonic variation for L_B was also reported by Sen *et al.* [1].

The nonmonotonic variation of L_B at lower Re and its monotonic variation at higher Re is addressed by examining the streamline plots. Figure 4.21 shows the streamline contours for $Re = 40$ and $Re = 70$ fields for flow past a circular cylinder computed with $H = 100$, 50 and 10. For all H, the streamlines which pass through two points (0, 1.2) and (0, 1.7) along with the separation streamlines are plotted. For $Re = 40$, we can see that as H decreases from 100 to 50, the streamlines shift in the upward direction (see zoom-in plot). On further decreasing H, the streamlines shift in the downward direction. The upward shift results in increase in the wake bubble length, while the downward shift causes just the opposite. One could relate these occurrences to the two competing physical effects: flow acceleration and no-penetration condition on the lateral boundaries. In the beginning, when the side boundaries move towards the centerline, the flow tends to accelerate in the vicinity of the cylinder. As a result, the cylinder ”feels” a slightly higher Re flow leading to stronger shear layers, upstream movement of the separation point and divergence of the streamlines away from the wake centerline causing the bubble length to increase. As we bring the side boundaries sufficiently close, the no-cross-flow condition on them ”pushes” the streamlines towards the wake centerline. Hence, the bubble

Table 4.11: The least-square fit of the bubble length data shown in figure 4.19 is represented in the form $L_B = \mathrm{A}Re^n$. The functional dependence of A and n on Ar is presented here. These equations hold good for 30$\leq$ Re $\leq$200.

H	A	n
10	$0.2286\mathrm{e}^{-0.7852Ar}$	$0.0197Ar^2 - 0.0347Ar + 1.0177$
20	$0.1774\mathrm{e}^{-0.6637Ar}$	$0.0045Ar^2 - 0.0594Ar + 1.1030$
30	$0.1503\mathrm{e}^{-0.5496Ar}$	$0.0202Ar^2 - 0.1063Ar + 1.1515$
50	$0.1301\mathrm{e}^{-0.4324Ar}$	$0.0494Ar^2 - 0.1652Ar + 1.1930$
100	$0.1198\mathrm{e}^{-0.3619Ar}$	$0.0718Ar^2 - 0.2047Ar + 1.2163$

length decreases. We therefore understand that the two competing effects mentioned above cause the nonmonotonicity in the variation of the bubble length with H. At higher Re, the wake bubble grows larger. Hence, the presence of the side boundary is felt early on. In this case, the effect of the mild flow acceleration is dominated by the constraint imposed by the no-cross-flow boundary condition. Thus, there is a monotonic decay of the bubble length.

The least-square fit of the bubble length data shown in figure 4.19 is best represented in the form of $L_B = \mathrm{A}Re^n$. Table 4.11 presents A and n as functions of Ar. The proposed empirical equations are good for $30 \leq Re \leq 200$. The maximum difference, over the Re range, in the bubble length obtained from the proposed equations and the actual data corresponding to H = 100, 50, 30, 20 and 10 are 5.03%, 3.85%, 4.49%, 5.25% and 4.15%, respectively. For $H = 100$ and $Ar = 1.0$, n is equal to 1.0831, which shows a near linear variation of L_B with Re. As Ar decreases down to 0.01, n increases (monotonically) up to 1.2147. We can see that n is a quadratic function of Ar. So, the minimum value of n could be of interest. However, except for $H = 10$, the minima for n occur at $Ar > 1$. $Ar > 1$ corresponds to the cylinder placed with its major axis along the streamwise direction. We do not know how well the results extrapolate in this regime. For $H = 10$, the bubble length equation shows almost linear variation with Re for all Ar. The value of n is 1.0026 for Ar = 1.0 and 1.0174 for Ar = 0.01. The minimum for n is 1.0024 and occurs at Ar = 0.88.

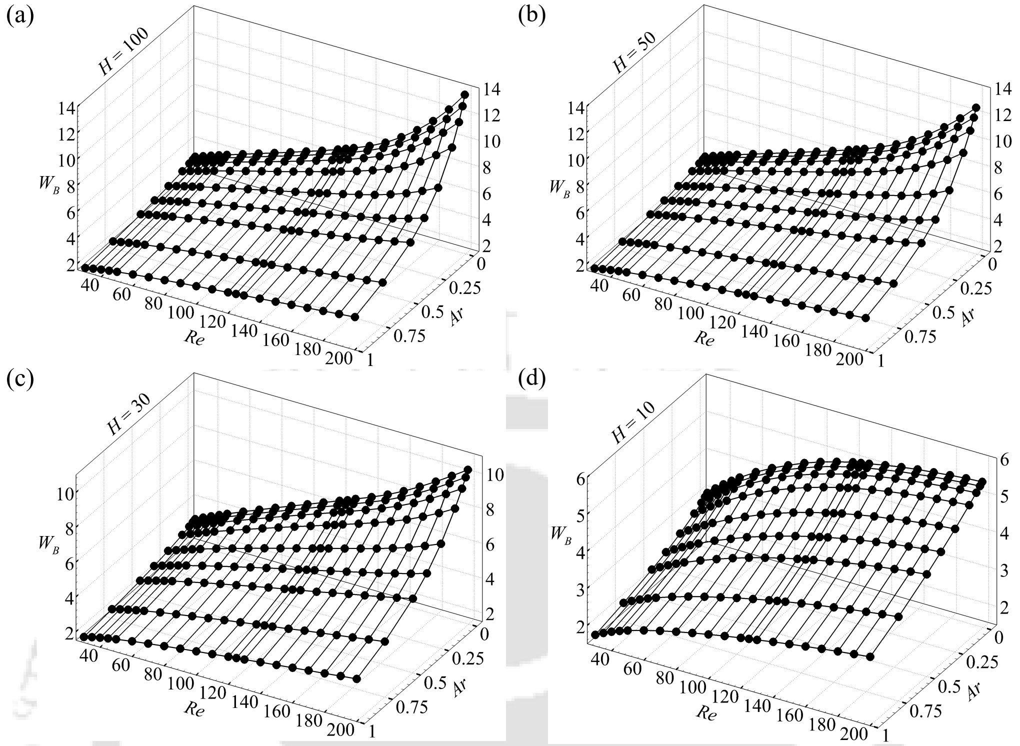

Figure 4.22: Variation of W_B with Re and Ar plotted for the domain with (a) H = 100, (b) $H = 50$, (c) $H = 30$ and (d) $H = 10$.

At this point, it is important to note that the equations presented for L_B in table 4.6 are either linear or quadratic. Attempt to provide a common expression for all Ar and still keep the error reasonably low has led us to consider a form different from that presented earlier. It is a fact that a given set of data could be approximated reasonably well by different functions in the range of parameters studied. It is really in the extrapolation beyond (the studied range) that the test of the approximation lies. As far as the results for unbounded flow past a circular cylinder is concerned, the linear growth of bubble length with Re is well established. Here is an attempt to arrive at a form which fits the data well for a wide range of parameters.

Variation of bubble width

Figure 4.22 shows the variation of W_B with Ar and Re plotted for different H. We can see that, in general, W_B increases with increase in Re/decrease in Ar. For Ar = 1.0, Gajjar & Azzam [3] and Fornberg [2] reported the decreasing trend in

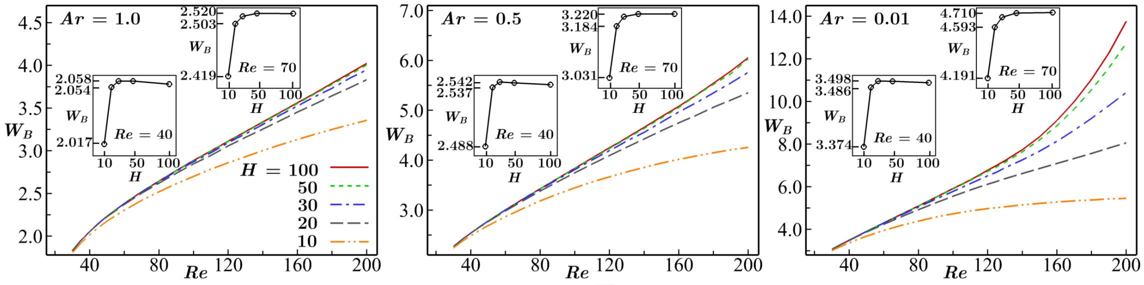

Figure 4.23: W_B versus Re for different H, plotted for Ar = 1.0 (left), 0.5 (middle) and 0.01 (right). The insets show the variation of W_B with H for Re = 40 and 70. The non-monotonic variation of bubble width with H is clearly visible.

bubble width with H. The variation of W_B versus Re for different domain sizes is plotted in figure 4.23 for Ar = 1.0, 0.5 and 0.01. The increase in W_B with Re is nonlinear and the nonlinearity appears to increase with decrease in Ar. For higher H, there is a rapid increase in W_B with Re. The rate of climb tends to increase with decrease in Ar. As it is true for L_B, the variation of W_B with H depends on Re. For $Re \leq 60$, the variation is nonmonotonic, while for higher Re, we see a monotonic change. The insets in figure 4.23 show W_B versus H curves for Re = 40 and 70. The nonmonotonic variation at Re = 40 and the monotonic variation at Re = 70 is clearly visible for all Ar. However, as we go down from H = 100 to H = 10, there is an overall decrease in W_B for all Re. This fall in W_B increases with increase in Re/decrease in Ar. The maximum occurs for Ar = 0.01, for which, the bubble width decreases by 60.33% upon decreasing H from 100 to 10.

The nonmonotonicity in the variation of W_B with H at lower Re and the monotonic variation for the same at higher Re can be explained along similar lines as presented for L_B versus H in the previous section. Figure 4.21 shows the change in the streamlines as we reduce H. The initial reduction in H causes the flow to accelerate resulting in the upward shift of the streamlines. W_B therefore increases. When the side boundaries are sufficiently close, the no-cross-flow condition on them cause the streamlines to shift downward reducing W_B. Hence, the nonmonotonicity. At a higher Re, the wake bubble grows and the effect of the no-cross-flow boundary condition dominates leading to a monotonic change in W_B.

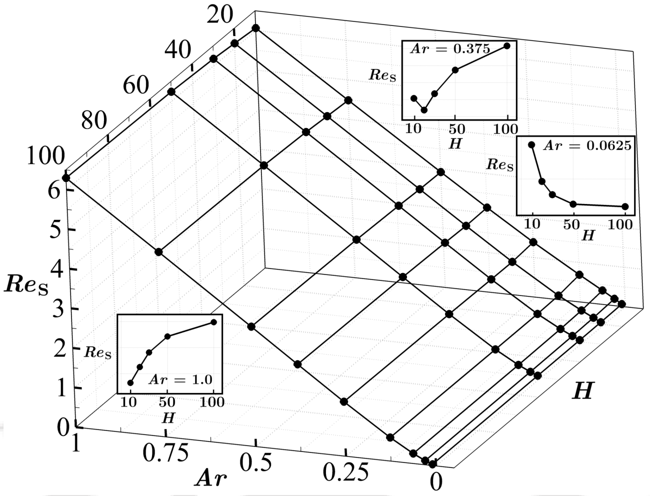

Figure 4.24: Three dimensional plot depicting the variation of Re_S with Ar and H. Insets showing the trend with respect to H for typical Ar are also shown.

Separation Reynolds number

Figure 4.24 shows a three dimensional plot depicting the variation of Re_S with Ar and H. Table 4.12 presents the Re_S data for the same. We can see that Re_S monotonically decreases with the decrease in Ar. This happens because the decrease in Ar causes the adverse pressure gradient on the cylinder surface to increase. Hence, the flow separates at a smaller Re.

The change of Re_S with H is rather nontrivial and depends on Ar of the cylinder. It is found from our computations that for Ar $0.5 \leq Ar \leq 1.0$, Re_S decreases monotonically with the decrease in H. A nonmonotonic variation with H is observed for $0.125 \leq Ar \leq 0.375$. For $0.01 \leq Ar \leq 0.0625$, Re_S monotonically increases with decrease in H. Insets in figure 4.24 show the trends for typical aspect ratios. We can understand this behaviour by taking into account the two competing effects-flow acceleration and the constraint due to the no-penetration on the side boundaries-discussed earlier regarding the variation of L_B with H, as well as the tendency of low Ar cylinders to develop high adverse pressure gradient supporting early flow separation. Quite obviously, flow acceleration due to the inward movement of side boundaries and the reduction in Ar, both cause the streamlines to shift away from the wake centerline. Therefore, at a certain Re, the streamlines for low Ar cylinders are expected to spread out more compared to that for high Ar cylinders. One can check this by drawing the streamlines which pass through a common point in both

Table 4.12: Re_S values for different Ar and H.

$Ar \setminus H$	100	50	30	20	10
1.0	6.2975	6.2427	6.1813	6.1252	6.0647
0.75	4.6729	4.6269	4.5759	4.5302	4.4847
0.5	3.0312	2.9960	2.9590	2.9288	2.9164
0.375	2.2032	2.1747	2.1469	2.1276	2.1414
0.25	1.3807	1.3605	1.3446	1.3399	1.3901
0.125	0.5985	0.5909	0.5936	0.6107	0.6904
0.0625	0.2553	0.2594	0.2745	0.2960	0.3549
0.03	0.1075	0.1173	0.1301	0.1437	0.1755
0.01	0.0343	0.0395	0.0446	0.0496	0.0610

the flow fields (similar to figure 4.21). Because of this, the streamlines in flow past a low Ar cylinder can ”feel” the constraint due to the no-penetration condition at a lower Re. The effect of the no-penetration condition is more dominant for low Ar cylinders than the effect due to flow acceleration. As the side boundaries come close, the streamlines are pushed towards the wake centerline thereby delaying separation. For similar reason, high Ar cylinders experience the effect of flow acceleration more than the no-penetration condition. Hence, the separation occurs early for them. For cylinders with moderate Ar, the two effects compete. Initially, the effect of flow acceleration dominates causing Re_S to reduce. Later, when the boundaries are close enough, the no-penetration condition pushes the streamlines toward the wake centerline delaying separation. We therefore, see the nonmonotonic variation.

Separation angle

Figure 4.25 shows the plot of θ_s versus Re for different domain size. These are plotted for Ar = 1.0, 0.5 and 0.25. We can see that θ_s increases with Re for all Ar and H. Also, there is an overall increase in θ_s with decrease in Ar. The variation of θ_s with H, however, shows different trends for different Ar. The variations are shown in the insets placed within the figure. For Ar = 1.0 and 0.75 (not shown

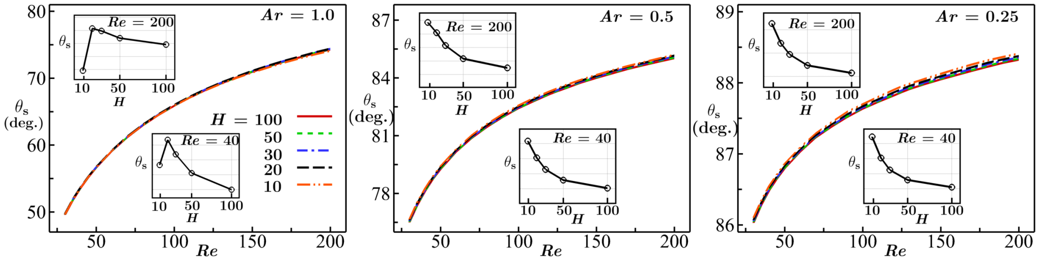

Figure 4.25: θ_s versus Re for different H, plotted for $Ar = 1.0$ (left), 0.5 (middle) and 0.25 (right). The insets show the variation of θ_s with H.

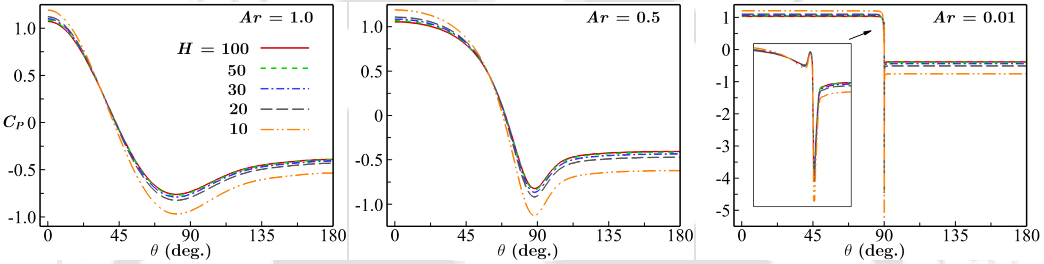

Figure 4.26: Variation of C_p with θ for $Re = 100$ flow past elliptic cylinders ($Ar =$ 1.0 (left), 0.5 (middle) and 0.01 (right)) computed with different H.

here), nonmonotonic variations of θ_s are observed. For $Ar = 1.0$, θ_s first increases with decrease in H from 100 down to 20. Thereafter, it decreases with decrease in H. This trend remains same at each Re. Sen *et al.* [1] reported the nonmonotonic behaviour of θ_s with decrease in H for flow past a circular cylinder. The present numerical results are consistent with those of Sen *et al.* [1] in the common range of parameters. For $Ar = 0.75$ and $Re \leq 100$, θ_s increases with decrease in H. Beyond $Re = 100$, θ_s shows nonmonotonic variation similar to $Ar = 1.0$. For $0.01 \leq Ar \leq 0.5$, θ_s increases monotonically with the decrease in H irrespective of Re.

Variation of Surface Pressure

Figure 4.26 shows the surface pressure distribution (C_p versus θ) for $Re = 100$ flow computed with different H. These are plotted for $Ar = 1.0$, 0.5 and 0.01. If we begin from the front stagnation point, except for very low Ar, C_p tends to decrease till around $\theta = 90°$. Beyond this, the pressure recovery happens till the rear stagnation point. The dip in C_p versus θ curve becomes more sharp as we decrease Ar. For very low Ar, C_p remains constant uptill close to $\theta = 90°$, where we see a sudden drop

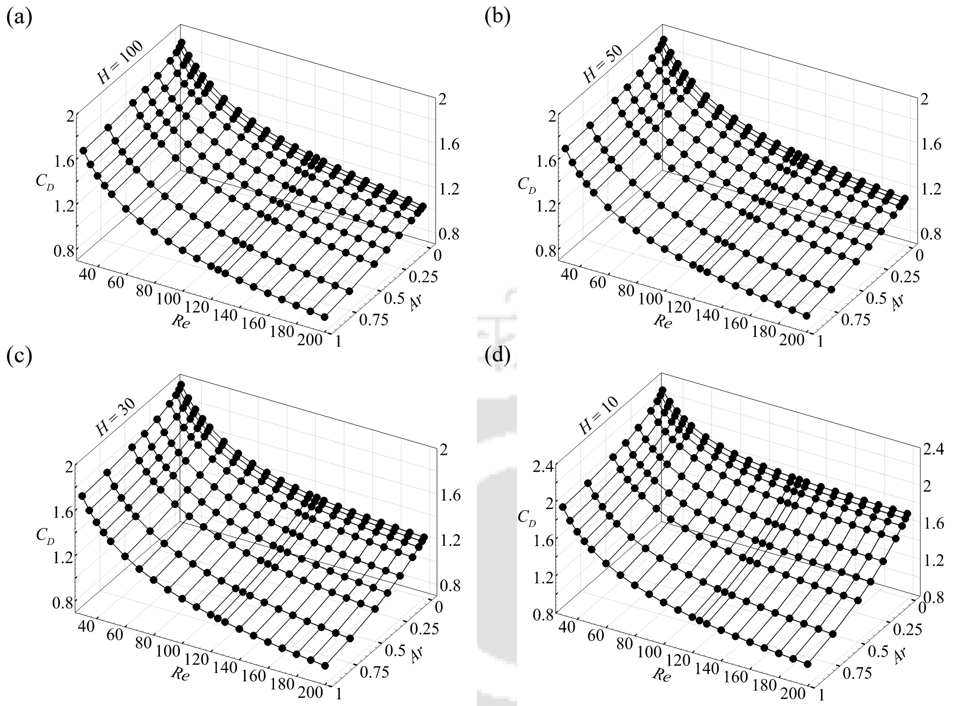

Figure 4.27: C_D as a function of Re and Ar, plotted for the domain with (a) $H = 100$, (b) $H = 50$, (c) $H = 30$ and (d) $H = 10$.

followed by an immediate rise to a smaller value. Thereafter, it remains constant till the rear stagnation point. This trend is seen for all H. The effect of change in H on C_p depends on θ. Pressure, at the front stagnation point (C_{p0}) and in the vicinity, increases with decrease in H. After a certain distance on the cylinder surface, the trend is reversed. As a result, $C_{p_{min}}$ and C_{pb} decrease with decrease in H. We therefore conclude that the pressure drag on the cylinder increases with decrease in H. This pattern is seen for cylinders of all Ar. The flow behaviour discussed here is typical and is found at other Re as well. For $Re = 40$ flow past a circular cylinder computed with $H = 20$, we obtain $C_{p0} = 1.2283$ and $C_{pb} =$ -0.5036. For the same flow parameters, Sen *et al.* [1] report $C_{p0} = 1.2246$ and $C_{pb} =$ -0.5037. Clearly, the results are in excellent agreement.

Variation of drag coefficients

Figure 4.27 shows the variation of C_D with Re and Ar. These are plotted for different H. We can see that C_D decreases monotonically with increase in Re. The

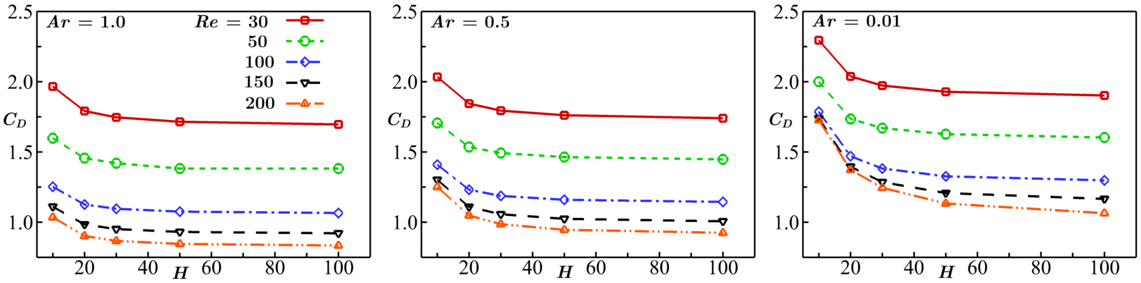

Figure 4.28: C_D versus H curves for different Re. These are plotted for $Ar = 1.0$ (left), 0.5 (middle) and 0.01 (right).

decreasing trend with Re remains consistent across all Ar and H. Figure 4.28 shows the variation of C_D with H for different Re. These are plotted for $Ar = 1.0$, 0.5, 0.01. For constant Re, C_D increases monotonically with decrease in H. This behaviour is same for all Ar. At low Re, the increase in C_D with decrease in H is less compared to the increase at higher Re. At $Re = 30$, C_D for flow past a circular cylinder increases by 15.89% with decrease in H from 100 down to 10, while at Re = 200, the same increase is 24.03%. The increase in C_D with decrease in H is gradually enhanced with the decrease in Ar. The highest rise in C_D with decrease in H from 100 down to 10 is 62.36%, and is observed at $Re = 200$ for $Ar = 0.01$.

The least square fit for C_D data shown in figure 4.27 can be represented in the form $\mathrm{A}Re^{-1} + \mathrm{B}Re^{-0.5} + \mathrm{C}$. A, B and C are presented as functions (dependent on H) of Ar in table 4.13. These curve fit equations hold good for $30 \leq Re \leq 200$. From the table, we can see that for $H = 100$ and 50, C_D varies as a linear function of $Re^{-0.5}$. For $H = 200$, $Ar = 1.0$ and $15 \leq Re \leq 40$, the best fit equation for C_D reported by Sen *et al.* [1] is a linear function of $Re^{-0.5}$. For $H \leq 30$, second-order polynomial fit is required to obtain better accuracy. We therefore conclude that nonlinearity in C_D versus $Re^{-0.5}$ increases with decrease in H. The maximum difference in the actual data and the values obtained from the curve fit for $H = 100$, 50, 30, 20 and 10 are 1.74%, 0.76%, 1.06%, 1.12% and 0.85%, respectively. The corresponding average differences are 0.28%, 0.29%, 0.28%,0.35% and 0.24%.

Maximum vorticity on the surface of the cylinder

Figure 4.29 shows the variation of ω_{max} as a function of Re and Ar. These are plotted for different H. We can see that ω_{max} monotonically increases with increases

Table 4.13: Functional coefficients A, B and C, appearing in the curve fit equation $C_D = \mathrm{A}Re^{-1} + \mathrm{B}Re^{-0.5} + \mathrm{C}$ (obtained from the data shown in figure 4.27), presented for different H. These expressions hold good for $30 \leq Re \leq 200$.

	$H = 10$
A	$16.1652Ar^{1.6} - 41.1660Ar^{0.8} + 34.6416$
B	$-4.6055Ar^{1.6} + 14.3331Ar^{0.8} - 3.7586$
C	$0.6221Ar^{1.6} - 1.9032Ar^{0.8} + 1.8427$
	$H = 20$
A	$25.3453Ar^{1.6} - 49.2758Ar^{0.8} + 27.1419$
B	$-6.5397Ar^{1.6} + 14.5298Ar^{0.8} - 0.8123$
C	$0.5929Ar^{1.6} - 1.5161Ar^{0.8} + 1.3005$
	$H = 30$
A	$21.6546Ar^{1.5} - 38.7071Ar^{0.75} + 18.0047$
B	$-5.0778Ar^{1.5} + 10.6799Ar^{0.75} + 2.0360$
C	$0.4154Ar^{1.5} - 1.1134Ar^{0.75} + 1.0193$
	$H = 50$
A	0
B	$3.3581Ar^{0.5} - 3.4364Ar^{0.25} + 7.8389$
C	$-0.7039Ar^{0.5} + 0.4389Ar^{0.25} + 0.5593$
	$H = 100$
A	0
B	$2.5790Ar^{0.64} - 2.7978Ar^{0.32} + 7.9067$
C	$-0.4777Ar^{0.64} + 0.2394Ar^{0.32} + 0.5285$

in Re/decrease in Ar. The rise in ω_{max} with Ar is sharp for $0.01 \leq Ar \leq 0.0625$. This is because, small Ar cylinders have large curvature near their shoulders, which leads to the development of large velocity gradients and large vorticity in the boundary layer. Large ω_{max} on the cylinder surface indicates the presence of a strong shear

Indian Institute of Technology Guwahati

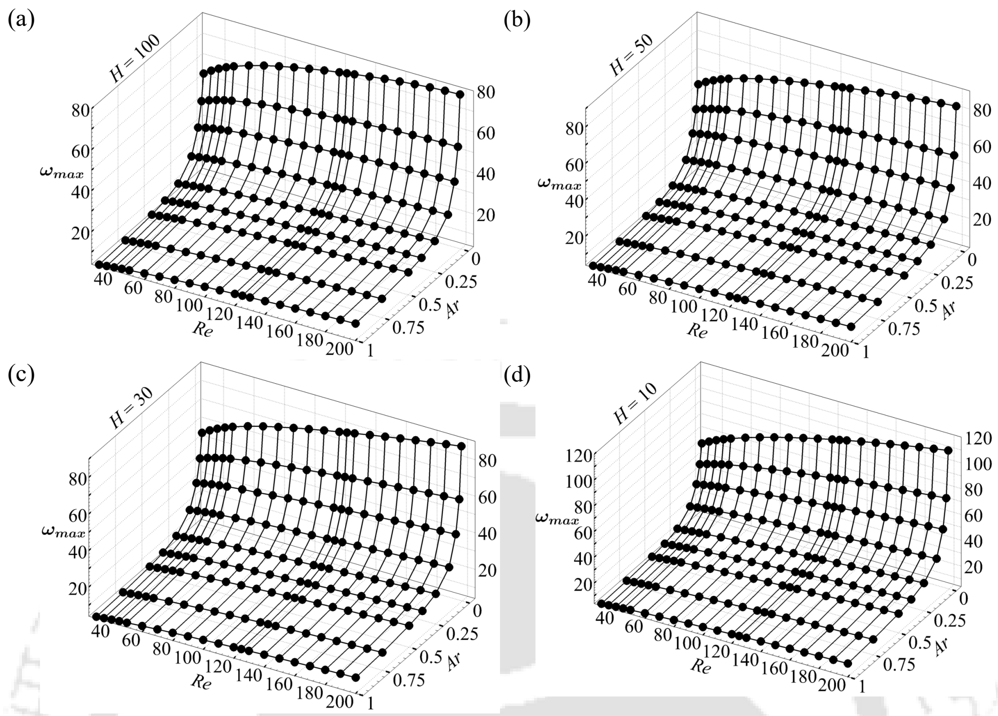

Figure 4.29: ω_{max} as a function of Re and Ar, plotted for the domain with (a) H = 100, (b) H = 50, (c) H = 30 and (d) H = 10.

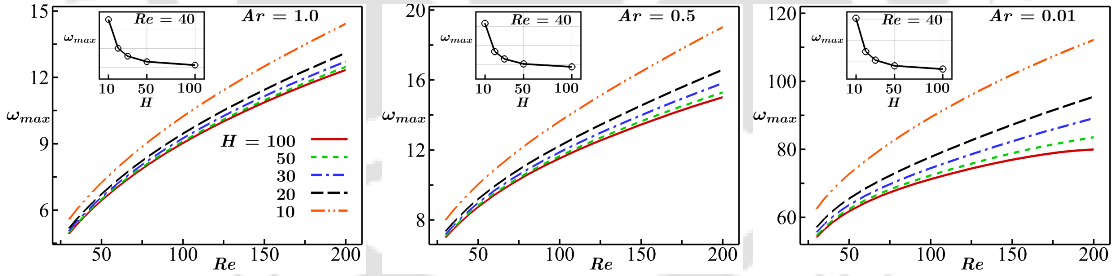

Figure 4.30: ω_{max} versus Re curves for different H, plotted for Ar = 1.0 (left), 0.5 (middle) and 0.01 (right). The insets show the variation of ω_{max} with H.

layer in the wake. Figure 4.30 shows the variation of ω_{max} with Re for different domain size. These are plotted for Ar = 1.0, 0.5 and 0.01. The insets in the figure show the variation of ω_{max} with H. Quite clearly, with the decrease in H, the rise in ω_{max} is more at higher Re than at lower Re. This rise is enhanced with decrease in Ar (see the relative spread between the curves for different H in figure 4.30). For Ar = 1.0, as we decrease H from 100 down to 10, ω_{max} increases by 13.22% at Re =

Table 4.14: Curve fit equations for ω_{max} on the surface of a circular cylinder for different domain size.

H	Empirical equation	$\vert$max % difference$\vert$
100	$2.3980Re^{0.35} - 2.9870$	0.5375
50	$2.4226Re^{0.35} - 3.0261$	0.7110
30	$2.4741Re^{0.35} - 3.1349$	1.0726
20	$0.0531Re^{0.7} + 2.0418Re^{0.35} - 2.1226$	0.0911
10	$0.1095Re^{0.7} + 1.7899Re^{0.35} - 1.4911$	0.0701

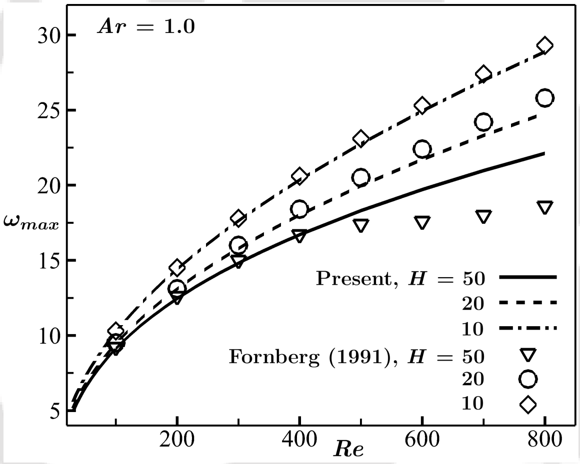

Figure 4.31: Comparison of ω_{max} extrapolated from empirical equations given in table 4.14 and numerical data of Fornberg [2] for 30≤ Re ≤800.

30 and by 16.88% at $Re = 200$. Similarly, for $Ar = 0.01$, ω_{max} increases by 15.70% at Re =30 and by 40.31% at $Re = 200$ for the same decrease in the domain size.

Table 4.14 presents the least square fit equations for ω_{max} obtained for a circular cylinder. The equations are presented for different H. The equations are linear in $Re^{0.35}$ for $H = 100$, 50 and 30, and quadratic in $Re^{0.35}$ for smaller domains. Using these equations, we extrapolate ω_{max} up to $Re = 800$. A comparison of the best fit equations with the results reported by Fornberg [2] is presented in figure 4.31. For $H = 50$, the extrapolated curve is in good agreement up to $Re = 400$. Interestingly, for $H = 20$ and 10, the extrapolations are in good agreement up to $Re = 800$.

Indian Institute of Technology Guwahati

Chapter 5

Linear stability analysis

In this chapter, we present the results obtained from the linear stability analysis of the steady base flow past elliptic cylinders. In the past, linear stability analysis of the flow past an elliptic cylinder has been carried out by several researchers (Jackson [57], Paul *et al.* [33], Thompson *et al.* [4]). However, the results are very scanty and do not give a comprehensive view of the flow behaviour. Here we present a detailed analysis of the related flow problem. The linear stability study is carried out for cylinders with different Ar, different flow Re and different lateral dimension (H) of the domain. Our results show the presence of three different kinds of eigenmodes in the flow which become unstable with increase in Reynolds number. We refer to them as the primary wake mode (PWM), the secondary wake mode (SWM) and the tertiary wake mode (TWM). These are identified based on their growth rate and modal structure in the flow field. The growth rate of PWM is the highest. It loses stability at relatively low Re and is responsible for the von Kármán vortex shedding. Upon increasing Re further, first SWM and then TWM loses stability. However, TWM is not observed to become unstable for all Ar.

Since there are three parameters (Re, Ar and H) which affect the flow behaviour, we first present the results for the domain with $H = 100$. Here the effect of Ar and Re on the stability characteristics are summarized. We then present the effect of varying H.

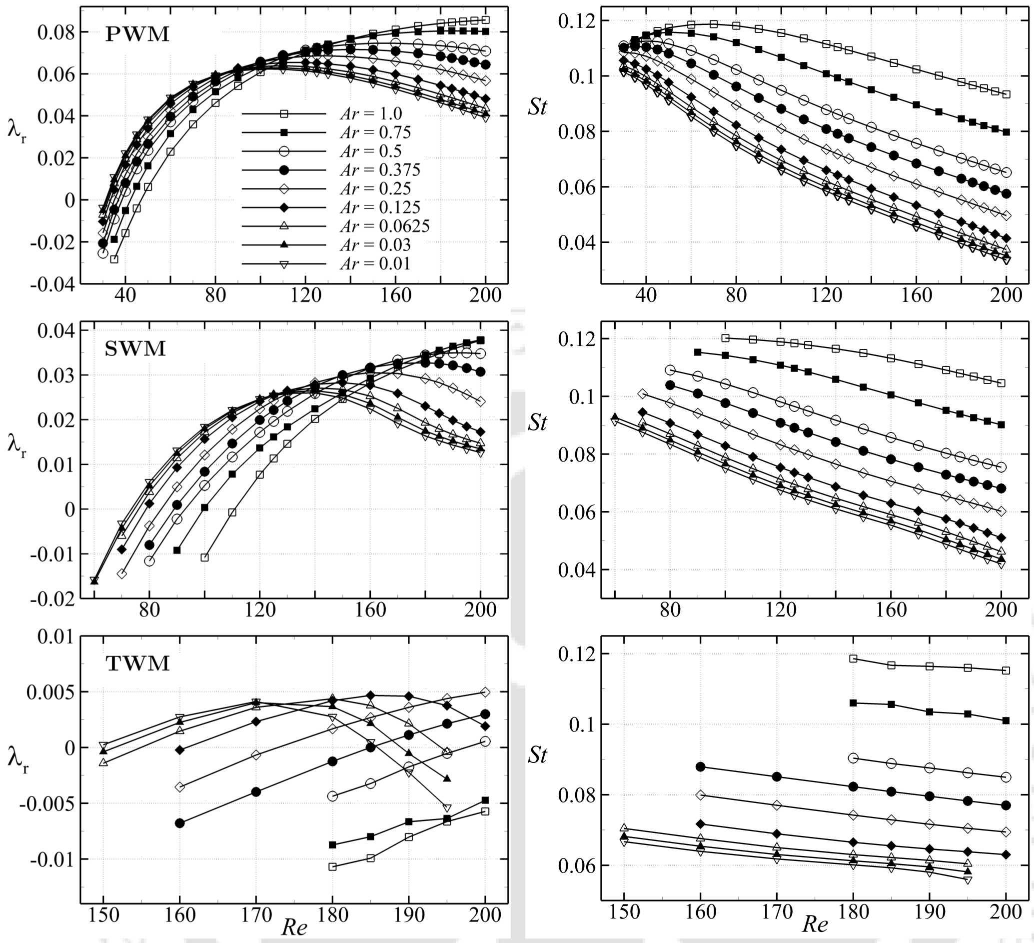

Figure 5.1: Variation of the growth rate (left column) and *St* (right column) for PWM (top row), SWM (middle row) and TWM (bottom row) with *Re* for the domain with $H = 100$.

5.1 Variation of growth rate and Strouhal number with *Re*

Figure 5.1 shows the variation of the growth rate (λ_r) and Strouhal number (St) with Re for PWM, SWM & TWM. The results are plotted for different aspect ratios of the cylinder inside a domain with $H = 100$. For PWM, the λ_r curves for $Ar = 1.0$ and 0.75 show a monotonic increase with Re. For other aspect ratios, it first increases and then passes through a maximum. It is found from these results that flow past a cylinder with low Ar exhibits higher growth rate at lower Re. Consequently, the critical Reynolds number for the onset of vortex shedding decreases for cylinder with smaller aspect ratio (Johnson *et al.* [94], Thompson *et al.* [4]). Similar observations can be made for SWM and TWM. For SWM, the λ_r curve for $Ar = 1.0$, 0.75 and 0.5 increases monotonically with Re. For other aspect ratios, it shows a nonmonotonic increase passing through a maximum. For TWM, the monotonic increase in λ_r is observed for Ar down to 0.25. Below this, the nonmonotonic increase similar to that found with the other modes is observed. For the considered Re range, TWM remains stable for $Ar = 1.0$ and 0.75. It become marginally unstable for $Ar = 0.5$ at $Re = 200$. And for lower Ar, it becomes unstable over a range of Re.

Right column of figure 5.1 shows the variation of St with Re for the three modes. For PWM, St curves show a non-monotonic variation for higher aspect ratio cylinders ($Ar = 1.0$, 0.75, 0.5). Similar observation has been reported for $Ar = 1.0$ by several researchers in the past (Giannetti & Luchini [14], Pier [11], Barkley [95]). For lower aspect ratios, St decreases monotonically with increase in Re. SWM and TWM show a monotonic decrease in St with increase in Re, for all Ar. There is however one difference in the St curves for TWM. Over all, the slope of the St curves, for TWM, is smaller than the other two modes and therefore the minimum which they reach, in the range of Re shown, is higher than that achieved by the other two modes.

5.2 Effects of blockage

From previous studies on flow past a circular cylinder (Kumar & Mittal [64], Boppana & Gajjar [61]), it has been found that blockage effects play an important role in modifying the stability characteristics of the flow. To investigate the effect of blockage, we carry out computations with five different domain widths ($H = 10$, 20, 30, 50 and 100). Recall, H is the half width of the domain. Blockage is defined as the reciprocal of the domain width. From our computations it is observed that, for each aspect ratio, the trend of the growth rate curve remains the same for all but $H = 10$ case. We therefore do not present these plots to avoid repetition. For the highest blockage considered, i.e., for $H = 10$, the growth rate of each mode, whether PWM, SWM or TWM, is found to monotonically increase with Re, for all Ar (see figure 5.2). In contrast, the St curve shows the same trend for all H. We can see from figure 5.2 that the St variation, for each of the PWM, SWM & TWM, for

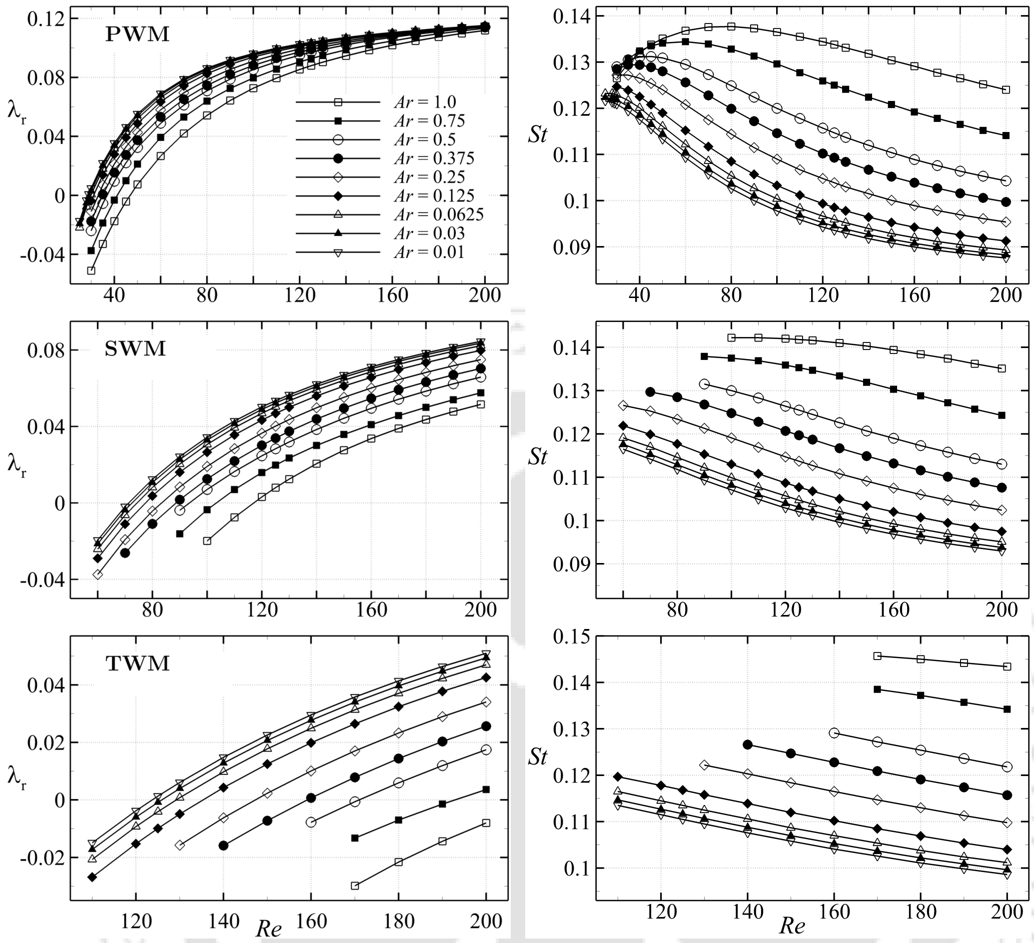

Figure 5.2: Variation of the growth rate (left column) and St (right column) for PWM (top row), SWM (middle row) and TWM (bottom row) with Re for the domain with $H = 10$.

each Ar, is similar to that shown in figure 5.1. Another conclusion which we derive from these computations is that there is an over all increase in the growth rate and St with increase in blockage. This can be confirmed by comparing figures 5.1 and 5.2. For each Ar, the λ_r curve in figure 5.2, for a large portion of the Re range, lies above the corresponding curve in figure 5.1. The same is true for the corresponding St curves in these figures.

To more clearly demonstrate the effect of blockage, we present in figure 5.3 the variation of growth rate and St with Re for different width of the domain. Here, Ar is taken as 0.25. From the figure we can see that, for PWM & SWM, for most part of the Re range, there is an increase in the growth rate with the increase in

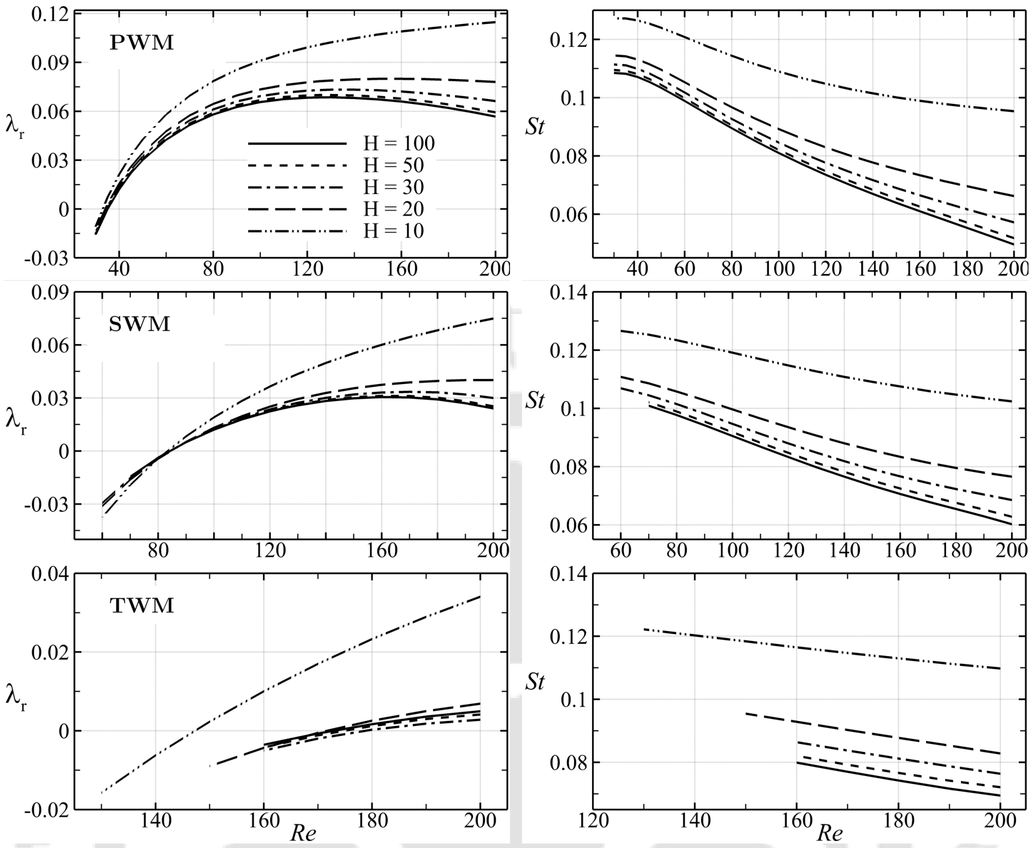

Figure 5.3: Variation of the growth rate (left column) and St (right column) for PWM (top row), SWM (middle row) and TWM (bottom row) with Re for flow past an elliptic cylinder with $Ar = 0.25$.

blockage. The growth rate of TWM however first decreases and then increases with increase in blockage. The St curve in figure 5.3 shows a monotonic increase with the blockage for all modes. The discussion above implies obvious effect on the critical Re for the onset of instability and the corresponding St for the three types of modes. We elaborate on this in the next section.

5.3 Critical parameters at the onset of instability

We determine the critical parameters (Re_c and St_c) for PWM, SWM & TWM, corresponding to their zero growth rate. Table 5.1 summarizes the critical values for $H = 100$. We can see that, for each eigenmode, Re_c and St_c decrease with the

Table 5.1: Critical Reynolds number and Strouhal number for PWM, SWM and TWM for flow past elliptic cylinders of varying Ar in a domain with $H = 100$.

	Re_c			St_c		
Ar	PWM	SWM	TWM	PWM	SWM	TWM
0.01	31.167	73.157	149.096	0.1010	0.0863	0.0670
0.03	31.598	74.220	151.468	0.1018	0.0873	0.0678
0.0625	32.052	75.807	154.566	0.1030	0.0887	0.0691
0.125	33.261	78.662	160.844	0.1049	0.0913	0.0715
0.25	35.084	84.059	172.696	0.1082	0.0963	0.0763
0.375	36.718	88.865	184.928	0.1107	0.1013	0.0809
0.5	38.347	92.737	197.226	0.1126	0.1063	0.0857
0.75	42.105	99.572	–	0.1150	0.1142	–
1.0	46.911	110.788	–	0.1167	0.1196	–

Table 5.2: Comparison of the critical parameters at the onset of the instability of PWM for flow past elliptic cylinders. The results are compared for $H = 100$.

	Thompson *et al.* [4]		Present	
Ar	Re_c	St_c	Re_c	St_c
0.25	35.6	0.1074	35.084	0.1082
0.5	38.8	0.1120	38.347	0.1126
0.75	42.6	0.1144	42.105	0.1150
1.0	47.2	0.1163	46.911	0.1167

decrease in the cylinder aspect ratio. Our calculations show that TWM does not become unstable for $Ar = 1.0$ and 0.75 below $Re = 200$.

Thompson *et al.* [4] performed linear stability analysis of flow past elliptic cylinders with different Ar. The critical parameters reported in their work for the onset

Table 5.3: Comparison of the critical parameters at the onset of the instability of PWM for $Ar = 1.0$ with previous studies for different blockages.

	$H = 10$		$H = 50$		$H = 100$	
Studies	Re_c	St_c	Re_c	St_c	Re_c	St_c
Jackson [57]	46.184	0.13804	–	–	–	–
Morzyński *et al.* [59]	47	0.1320	–	–	–	–
Sahin & Owens [5]	50.75	0.1211	–	–	46.74	0.1167
Kumar & Mittal [64]	47.222	0.1344	47.189	0.1178	47.313	0.1168
Boppana & Gajjar [61]	49.8	0.1358	48.8	0.1181	–	–
Thompson *et al.* [4]	–	–	–	–	47.2	0.1163
Present	46.738	0.1343	46.740	0.1177	46.911	0.1167

of instability corresponds to the same for PWM in our case. Table 5.2 compares the Re_c and St_c with those reported by Thompson *et al.* [4]. The results are in excellent agreement. Except for $Ar = 1.0$, where the difference is less than 0.3, Re_c at best differs in the first decimal place, whereas St_c differs in the third or fourth decimal place. The work done by Boppana & Gajjar [61] on flow past a cascade of circular cylinder showed the presence of second unstable pair (SWM in the present nomenclature) which becomes unstable between $Re = 125$ and 150 for a domain size corresponding to $H = 10$. The critical value was however not reported. Verma & Mittal [62] were the first to determine the critical Reynolds number for the SWM for flow past a circular cylinder. Re_c value reported by them is 110.8 and the St_c though not mentioned explicitly is close to 0.12. The data presented in Table 5.1 depicts a close match with these results. Table 5.3 compares the critical parameters of PWM for $Ar = 1.0$ with previous studies for different blockages. Slight variation in Re_c is observed. However, St_c shows close agreement with earlier studies. The difference in Re_c could be due to the use of different numerical methods, different mesh resolution or different location of the upstream and the downstream boundaries by previous studies. For $Ar = 0.5$, Jackson [57] reported $Re_c = 35.704$ and $St_c = 0.13321$, for a domain corresponding to $H = 10$. For this blockage and aspect ratio, we found $Re_c = 36.705$ and $St_c = 0.1308$. The difference could be attributed

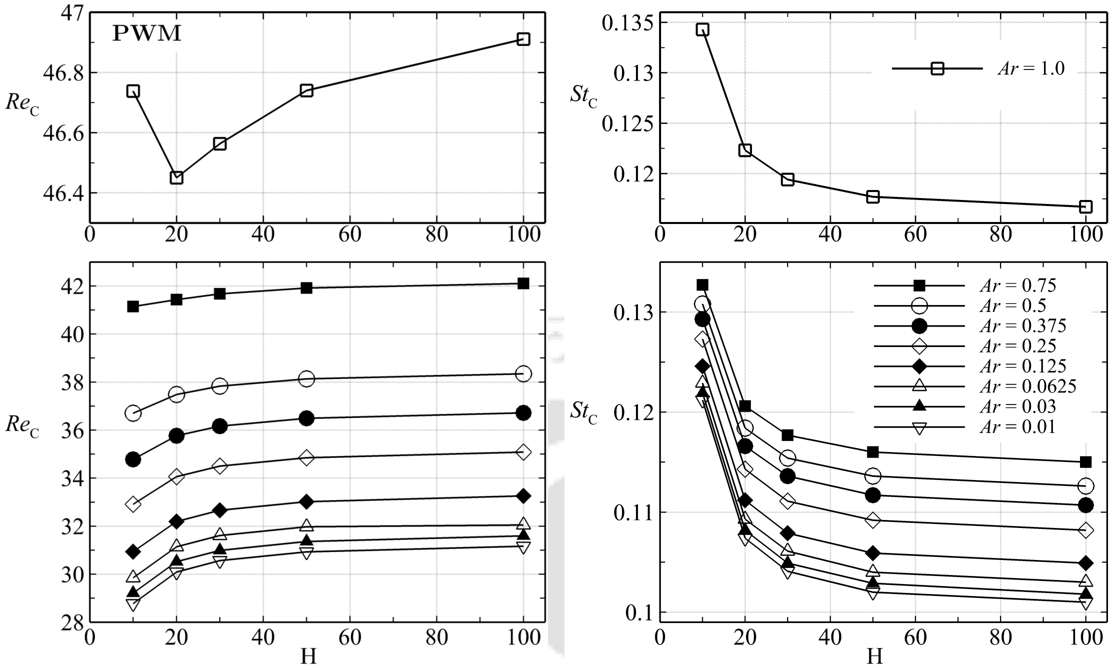

Figure 5.4: Effect of blockage on the critical Reynolds number (left) and the critical Strouhal number (right) for PWM.

to a much finer grid in our case.

In figures 5.4, 5.5 and 5.6, we show the effect of blockage on critical parameters for PWM, SWM & TWM, respectively. It can be observed that Ar has significant effect on the variation of Re_c with H. In contrast, St_c variation does not show any qualitative change with Ar. Based on the trend in Re_c curve, we therefore divide the plots into two categories for PWM and SWM. The top row of figure 5.4 shows the results for $Ar = 1.0$. For this case, Re_c first decreases with blockage and then increases. The non-monotonic variation of Re_c with blockages is similar to that presented by Kumar & Mittal [64] and Boppana & Gajjar [61]. While comparing the results, we note that Kumar & Mittal [64] had computed results for several smaller domain sizes and therefore a smooth curve fit was possible. Also, in the present case, the streamwise extent of the domain is larger, and therefore, according to Kumar & Mittal [64], has a consequent effect on the trend. From the results presented by Boppana & Gajjar [61], we see that the trend for the OE modes matches with that of PWM in the range of blockage used in the present work.

The second row of figure 5.4 shows the results for other aspect ratios ($0.01 \leq Ar \leq 0.75$). It is observed that the Re_c monotonically decreases as we increase

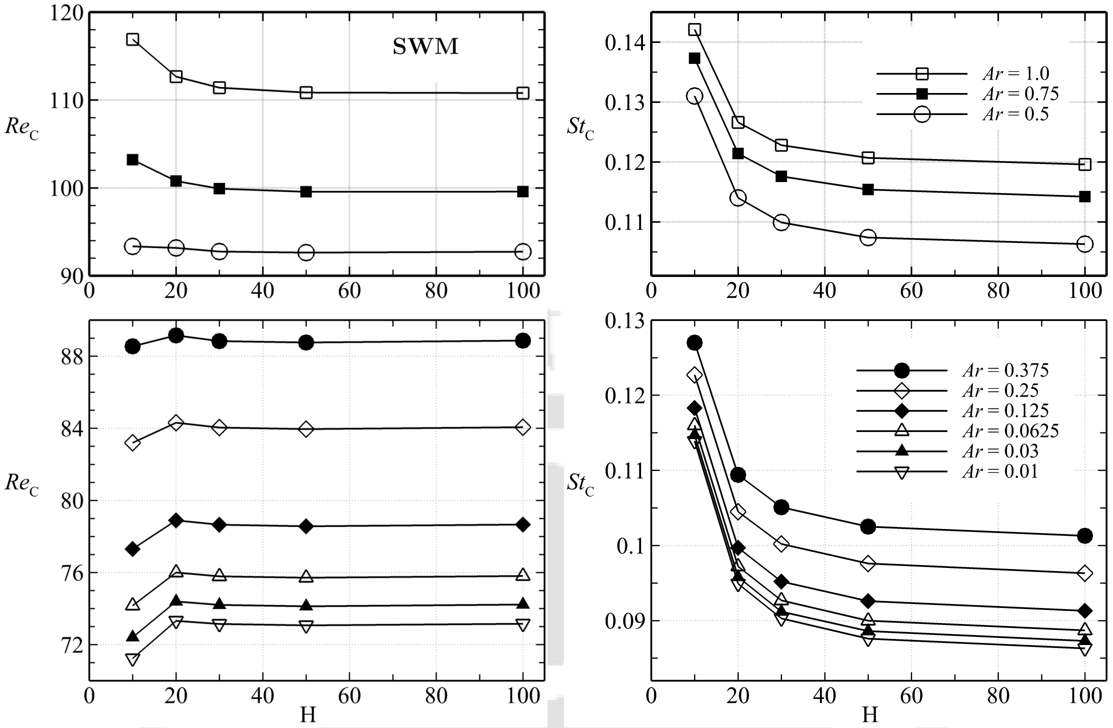

Figure 5.5: Effect of blockage on the critical Reynolds number (left) and the critical Strouhal number (right) for SWM.

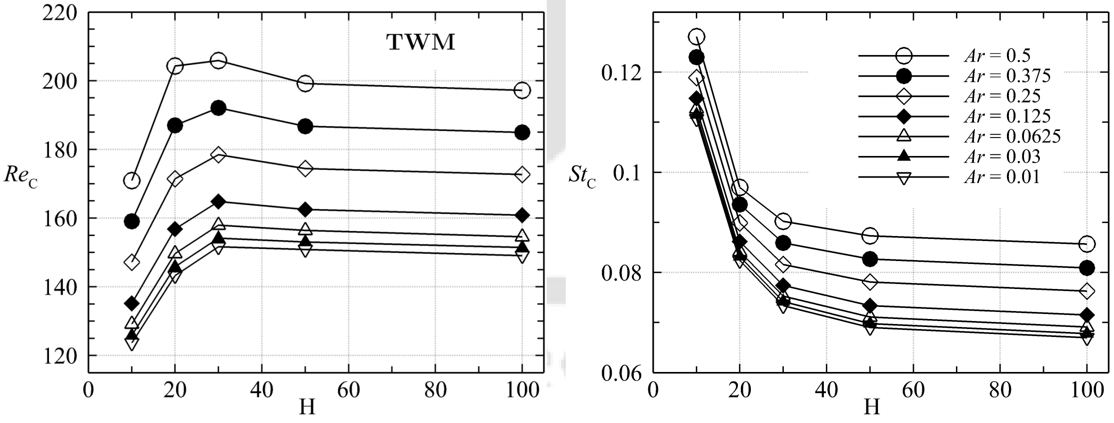

Figure 5.6: Effect of blockage on the critical Reynolds number (left) and the critical Strouhal number (right) for TWM.

the blockage. This possibly happens because the decrease in the aspect ratio causes the shear layer on either side of the cylinder to becomes stronger leading to stronger instability of the wake.

Table 5.4: Least-square curve fit equations, for the critical Reynolds number and the corresponding Strouhal number for PWM, obtained as a function of aspect ratio (0.01$\leq Ar \leq$1) and domain size (10$\leq H \leq$100).

	$Re_c = CAr^3 + DAr^2 + EAr + F$
C	$-21.3648\ H^{-0.4} + 17.4588\ H^{-0.2} + 6.650$
D	$68.3015\ H^{-1.2} - 4.7346\ H^{-0.6} - 13.0540$
E	$4.3390\ H^{0.8} - 36.0285\ H^{0.6} + 112.0671\ H^{0.4} - 154.7548\ H^{0.2} + 98.6937$
F	$-39.5543\ H^{-0.4} + 30.6258\ H^{-0.2} + 25.0831$
	$St_c = CAr^3 + DAr^2 + EAr + F$
C	$-6.1176\ H^{-0.8} + 11.6463\ H^{-0.6} - 8.1568\ H^{-0.4} + 2.4945\ H^{-0.2} - 0.2684$
D	$13.5124\ H^{-0.8} - 26.1136\ H^{-0.6} + 18.7005\ H^{-0.4} - 5.8835\ H^{-0.2} + 0.6514$
E	$-11.3440\ H^{-0.8} + 22.4236\ H^{-0.6} - 16.5596\ H^{-0.4} + 5.4036\ H^{-0.2} - 0.6185$
F	$1.5528\ H^{-0.6} - 1.9116\ H^{-0.4} + 0.7996\ H^{-0.2} - 0.0126$

Figure 5.5 shows the variation of Re_c and St_c with H for SWM. The top row presents the results for higher aspect ratios ($0.5 \leq Ar \leq 1.0$). Here, Re_c is found to increase with increase in blockage. An exception is $Ar = 0.5$. In this case there is no significant change in Re_c down to $H = 10$. In the second row of figure 5.5, results for lower aspect ratios ($0.01 \leq Ar \leq 0.375$) are shown. A non-monotonic variation of Re_c with blockage is observed. For all Ar, both in the top and bottom row of the figure, Re_c seems to settle beyond $H = 50$. The St_c curve however shows an increase with blockage for all Ar. For TWM, results are shown in figure 5.6. It is observed that Re_c first increases with blockage, reaches a maximum at $H = 30$, and then decreases. Unlike PWM and SWM, the trend for TWM is same for all Ar. St_c for TWM shows a monotonic increase with blockage for all Ar.

In Tables 5.4, 5.5 and 5.6, we present the least-square curve fit equations obtained for Re_c and St_c for PWM, SWM and TWM. The empirical equations proposed here can be used to determine the critical parameters for PWM, SWM and TWM for any Ar between 0.01 and 1.0, and any H between 10 and 100. For PWM, it is found that both Re_c and St_c shows non-linear variation with Ar and H. Third

Table 5.5: Least-square curve fit equations, for the critical Reynolds number and the corresponding Strouhal number for SWM, obtained as a function of aspect ratio (0.01$\leq$ Ar $\leq$1) and domain size (10$\leq$ H $\leq$100).

	$Re_c = CAr^3 + DAr^2 + EAr + F$
C	$-5981.0567\ H^{-3} + 457.2841\ H^{-2} - 32.5357\ H^{-1} + 37.6868$
D	$2792.0789\ H^{-3} + 443.2216\ H^{-2} + 52.7852\ H^{-1} - 60.0160$
E	$3327.5993\ H^{-3} + 11.5777\ H^{-2} - 33.6417\ H^{-1} + 60.7109$
F	$-11919.8492\ H^{-3} + 1402.0746\ H^{-2} - 41.7449\ H^{-1} + 72.6326$
	$St_c = DAr^2 + EAr + F$
D	$-1551.1905\ H^{-4} + 288.6587\ H^{-3} - 16.3854\ H^{-2} + 0.3328\ H^{-1} - 0.0151$
E	$1024.4048\ H^{-4} - 184.6706\ H^{-3} + 9.4589\ H^{-2} - 0.1999\ H^{-1} + 0.0484$
F	$1.9016\ H^{-2} + 0.1003\ H^{-1} + 0.0844$

Table 5.6: Least-square curve fit equations, for the critical Reynolds number and the corresponding Strouhal number for TWM, obtained as a function of aspect ratio (0.01$\leq$ Ar $\leq$0.5) and domain size (10$\leq$ H $\leq$100).

	$Re_c = EAr + F$
E	$-0.6173\ H^{2} + 16.6247\ H^{1.5} - 160.7328\ H + 655.0883\ H^{0.5} - 832.1217$
F	$0.1506\ H^{2} - 3.4062\ H^{1.5} + 24.9510\ H - 60.3226\ H^{0.5} + 156.9142$
	$St_c = EAr + F$
E	$87.1222\ H^{-3} - 10.7706\ H^{-2} + 0.1638\ H^{-1} + 0.0375$
F	$-65.7677\ H^{-3} + 12.5179\ H^{-2} - 0.1612\ H^{-1} + 0.0672$

order polynomial is required to obtain the curve fit equations for both Re_c and St_c. The maximum difference between the actual value of Re_c and the value obtained from the empirical equation is less than 0.27% and the average difference is less than 0.12%. For St_c, the maximum difference is 0.16% and average difference is 0.05%.

Indian Institute of Technology Guwahati

For SWM (see Table 5.5), third order polynomial is required to obtain the curve fit equations for Re_c. However, for St_c, the second-order polynomial is sufficient to predict the results with good accuracy. The maximum difference between the actual value of Re_c and the value obtained from the empirical equation is less than 0.47% and the average difference is less than 0.23%. For St_c, the maximum difference is 0.54% and the average difference is 0.18%. For TWM (see Table 5.6), the linear variation of Re_c and St_c is obtained with Ar. However, Re_c and St_c vary non-linearly with H. The empirical equations for TWM is obtained for aspect ratios, $0.01 \leq Ar \leq 0.5$. As mentioned earlier, TWM does not become unstable for $Ar = 1.0$. For $Ar = 0.75$, TWM becomes unstable only for $H = 10$. For TWM, the maximum difference between the actual value of Re_c and the value obtained from empirical equation is less than 0.58% and the average difference is less than 0.13%. For St_c, the maximum difference is 0.45% and the average difference is 0.20%.

5.4 Structure of eigenmodes

Figure 5.7 presents the real and imaginary parts of the three unstable eigenmodes, PWM, SWM & TWM, for flow past a cylinder with $Ar = 0.25$ at $Re = 180$ in a domain with $H = 100$. The mode structures shown are typical and are observed to have similar features at other Reynolds numbers as well. The cross-stream velocity and vorticity field of these modes are symmetric about the wake centerline. This is opposite to that of the base flow. The structures of stream-wise velocity and pressure are skew-symmetric about the wake centerline. The comparison between real and imaginary parts of the eigenmodes shows that they have similar structure, however, there is a spatial shift of one fourth of the (local) wave length between them. This shift combined with the corresponding temporal shift of one fourth of the time period of oscillation gives rise to the downstream convection of the vortices.

From the figure, we can see that the strength and extent of the three modes vary in the flow field. Here, it should be noted that the range of each flow variable is kept same for all three eigenmodes. For example, the range of vorticity fields for PWM, SWM, and TWM is same in all plots. We can see that PWM appears more prominent in the near wake and decays rapidly as we move downstream. Comparatively, SWM extends to a much larger distance away from the cylinder. Its strength seems to increase as we move downstream, however, there is a decrease in strength

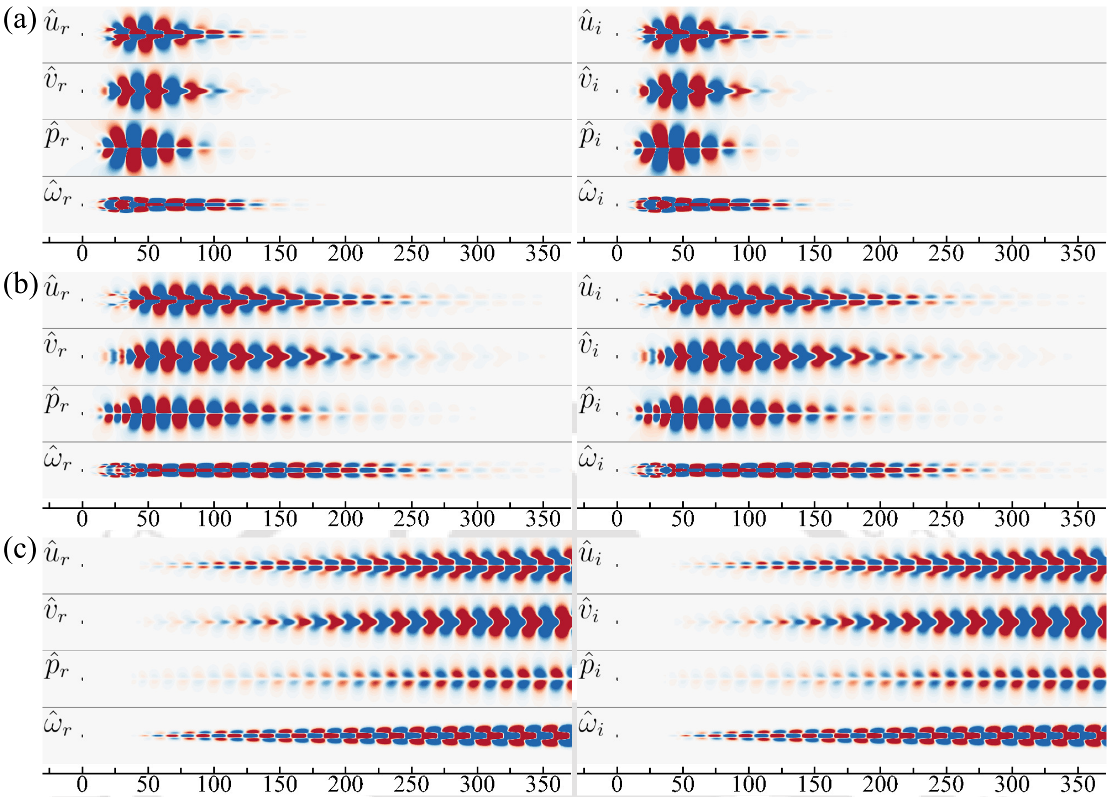

Figure 5.7: Real (left) and imaginary (right) parts of the stream-wise velocity ($\hat{u}$), cross-stream velocity ($\hat{v}$), pressure ($\hat{p}$), and vorticity fields ($\hat{\omega}$) corresponding to the three unstable eigenmodes, (a) PWM, (b) SWM, and (c) TWM, for flow past a cylinder with $Ar = 0.25$, $H = 100$ and $Re = 180$.

in the far wake. TWM is not so prominent in the near wake, but has the longest range of presence and extends all the way up to the downstream boundary. By and large, it is observed that the modes which have larger growth rate tend to come close to the cylinder surface and the extent to which they spread downstream in the wake is less compared to the modes which have smaller growth rate. In other words, stronger modes tend to approach the cylinder and also contract, whereas the modes which are weaker tend to recede and elongate. The size of the vortical structures present in a mode is large if its St is small and vice-versa. With this in view, we can understand the changes observed in the structure, length and location of the modes with change in Ar, Re and H.

In figure 5.8, we show the effect of varying aspect ratio on the structure of eigenmodes for $Re = 180$ flow. It is observed that with decrease in the aspect ratio,

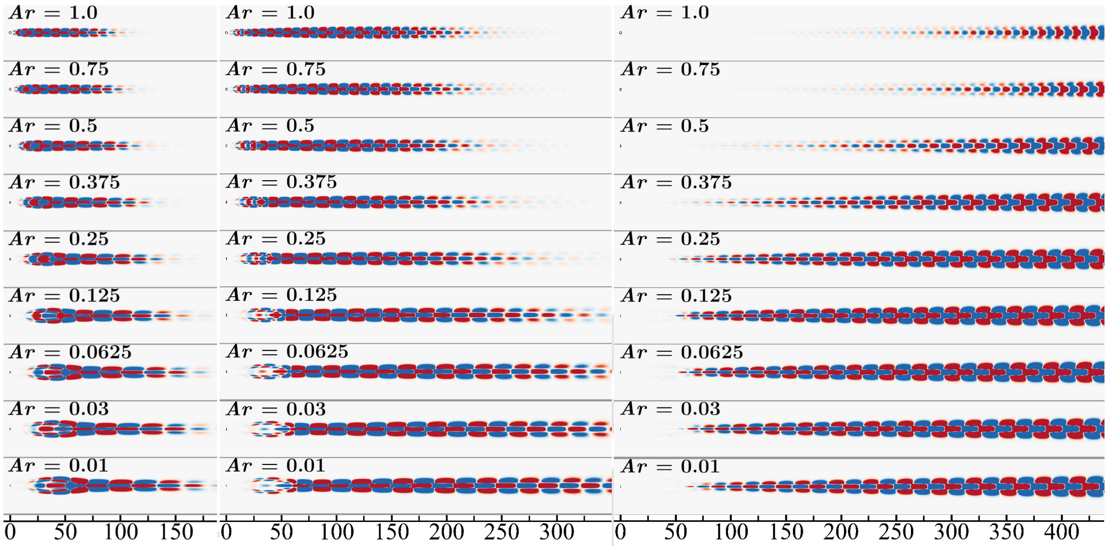

Figure 5.8: Comparison of the vorticity fields (real part) of PWM (left), SWM (middle) and TWM (right) obtained for $Re = 180$ flow past cylinders with different Ar in a domain with $H = 100$.

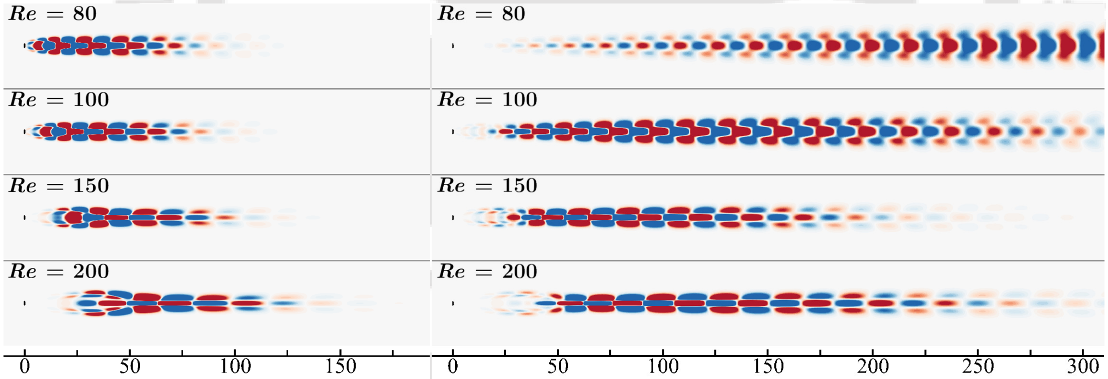

Figure 5.9: Comparison of the vorticity fields (real part) of PWM (left) and SWM (right) obtained with different Re, for $Ar = 0.25$ and $H = 100$.

PWM and SWM appear to recede downstream in the region close to the cylinder, and the extent, to which they spread in the wake, increases. This can be compared with the trend in the growth rate observed from figure 5.1. Clearly, at $Re = 180$, the growth rate decreases with decrease in Ar. Though we do not show this here, for low Reynolds numbers like $Re = 80$, opposite trend in the mode features is seen when we plot them with decreasing Ar. The behaviour of TWM is rather nontrivial. The

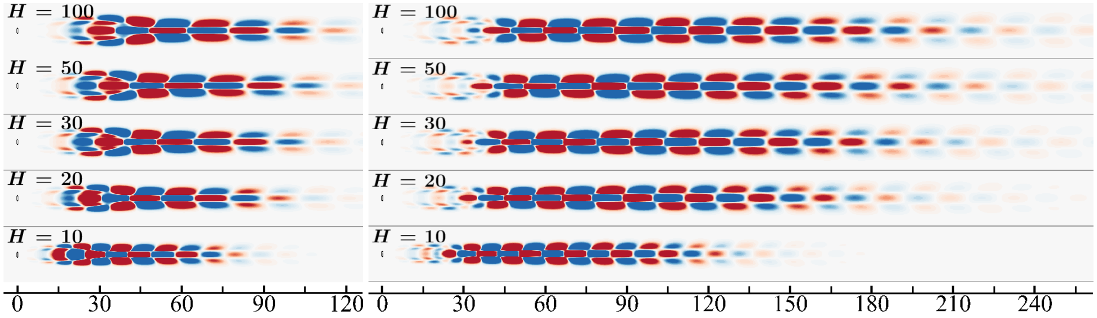

Figure 5.10: Comparison of the vorticity fields (real part) of PWM (left) and SWM (right) obtained with different H for $Re = 180$ flow past a cylinder with $Ar = 0.25$.

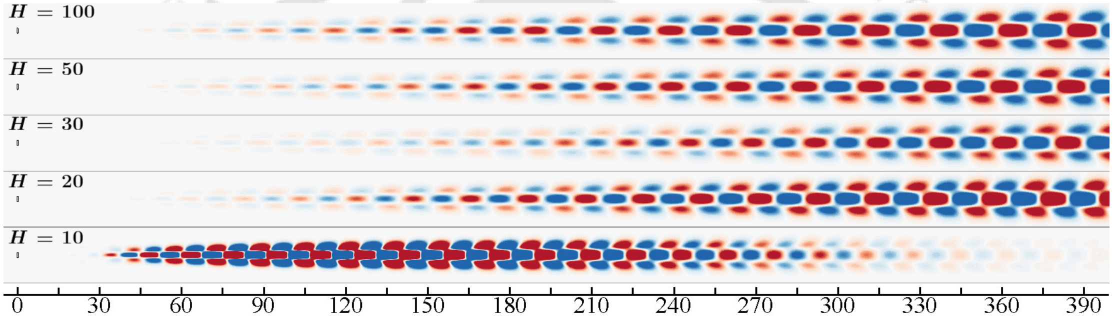

Figure 5.11: Comparison of the vorticity fields (real part) of TWM obtained with different H for $Re = 180$ flow past a cylinder with $Ar = 0.25$.

mode for $Ar = 1.0$ is the weakest and is almost nonexistent close to the cylinder. The modes corresponding to $Ar = 0.0625$, 0.125 and 0.25 happen to be the closest to the cylinder and therefore are among the strongest. The lateral width and size in the vortical structures of the eigenmodes also increase with decrease in the aspect ratio. This corresponds to a consequent decrease in the St. These conclusions are consistent with the results shown in figure 5.1.

Figure 5.9 shows the effect of Reynolds number on the structure of PWM and SWM for $Ar = 0.25$. TWM loses stability at higher Reynolds number and therefore we do not have much data to show the trend for this mode. With increase in the Reynolds number, PWM first comes a little close to and then drifts away from the cylinder. Also, the extent to which it spreads in the downstream first decreases and then increases. This indicates the initial strengthening and subsequent weakening of the mode. SWM also shows similar trend with an increase in Re. Again, these observations agree with the results shown in figure 5.1.

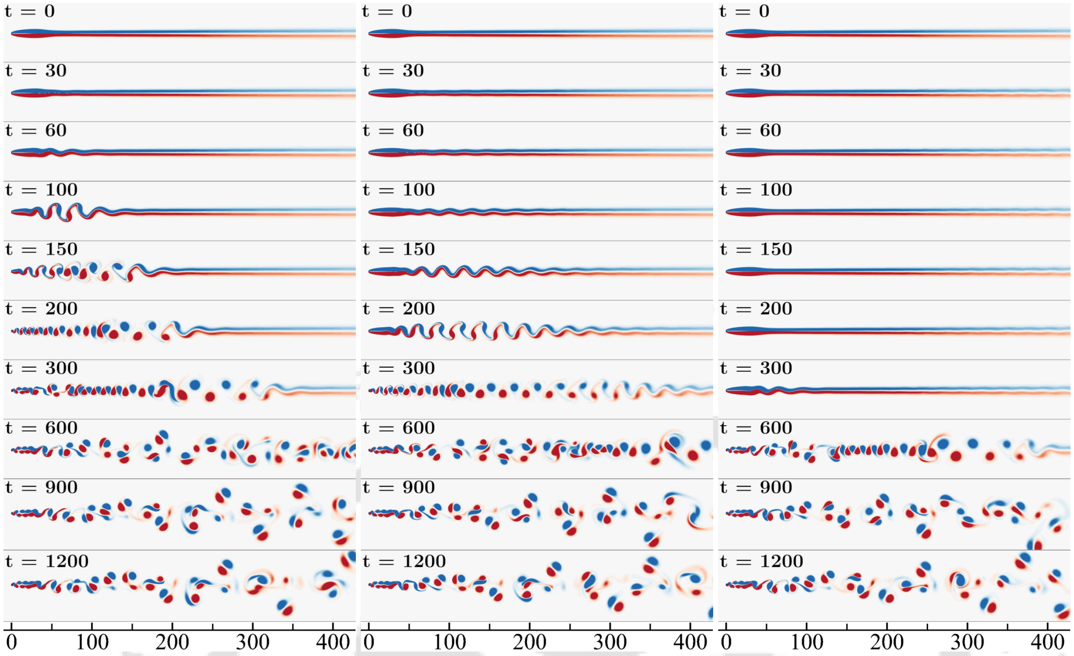

Figure 5.12: Time evolution of the vorticity field for the computations initiated with the steady flow + PWM (left), steady flow + SWM (middle) and steady flow + TWM (right). The computaions are done for $Re = 180$, $Ar = 0.25$ and $H = 100$.

Figures 5.10 and 5.11 show the effect of blockage on the structure of eigenmodes for $Re = 180$ flow past a cylinder having $Ar = 0.25$. To demonstrate the effect, we plot the vorticity fields for PWM, SWM and TWM. Over all, with increase in blockage, the modes are found to move close to the cylinder and are also seen to decay faster in the downstream direction. The size of the vortical structures present in the mode also decreases with increase in blockage. This is consistent with the results presented in figure 5.3. With increase in blockage, the growth rate of the modes increases. The simultaneous increase in St is related to the relatively small scale vortical structures present in the modes for higher blockage.

5.5 Time evolution of the eigenmodes

In previous sections we have shown the results confirming the existence of PWM, SWM and TWM, which progressively become unstable as we increase the flow Reynolds number. Since the fully developed flow is more or less the same what-

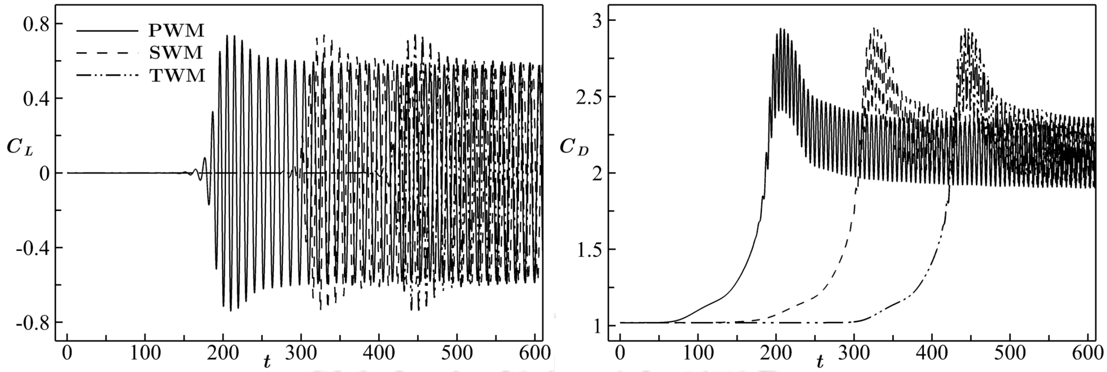

Figure 5.13: Time evolution of the lift and drag coefficient for the computations initiated with a combination of steady flow + PWM/SWM/TWM, for $Re = 180$ flow past an elliptic cylinder with $Ar = 0.25$ inside a domain with $H = 100$.

ever initial conditions we choose to begin with, one may wonder about the role of these modes and their relation with the unsteady flow. In order to study this we first compute the unsteady flow starting from the combination of the steady flow and one of these modes. We therefore have three different flow evolutions under consideration. We select $Re = 180$, $Ar = 0.25$ and $H = 100$ for which all the three modes are unstable. The time step size, $\varDelta t = 0.01$, is used for computing the unsteady flow. Figure 5.12 shows the time evolution of the vorticity field for the three different initial conditions. In each case, flow evolves differently with time until the nonlinear effects become prominent and eventually lead to the von Kármán vortex shedding in the near wake followed by large scale oscillations in the far wake. The time histories of the lift and drag coefficient in figure 5.13 show that the computation which begins with the PWM over the steady flow evolves faster and reaches the limit cycle sooner compared to the computations which begin with SWM or TWM over the steady flow. As expected, in each case, the flow reaches the same fully developed unsteady flow. Verma & Mittal [62] arrived at similar conclusions regarding flow past a circular cylinder.

From the above discussion it appears that the three modes have no specific role as far as the fully developed flow is concerned. However, if by some means, we kill all the modes, we get the steady flow and not the unsteady flow. It is therefore important to ask what kind of flow would evolve if only one of the modes or only two of them were allowed to grow. We address this question in next chapters.

Chapter 6

Structural sensitivity analysis

This chapter presents the structural sensitivity analysis results computed to find the region best suitable for effecting control of the unstable modes. In order to compute the flow with selective suppression of the linear modes, we first determine the region in the flow field where introducing a body would effect the suppression. In the past, the region for passive control has been determined by carrying out structural sensitivity analysis. Chomaz [74] and Giannetti & Luchini [14] showed that the region in the flow field which is most sensitive to the structural perturbations could be determined by taking the point-wise product of the direct and the adjoint modes. Chomaz [74] called the most sensitive region as the overlap region. The overlap region is identified as the core of instability, and it produces a significant drift in the eigenvalue if a small body is placed inside it. Figure 6.1 compares the structure of the direct mode and the adjoint mode. The cross-stream velocity field of PWM, SWM and TWM are shown for $Re = 180$, $Ar = 0.25$ and $H = 100$. Unlike the direct modes, the adjoint modes extend in the upstream direction. The overlap region for the same is shown in figure 6.2. It is observed that the location of the maximum for PWM lies at $x = 40.62$, and it appears in the later half of the separation bubble. The location of maximum of the overlap region is significant as far as the choice of structural perturbation is concerned. If we choose to place a slip-plate on the wake centerline to suppress the mode oscillations, the peak location mentioned above is expected to be the best. For SWM, we get two different peaks. The first peak lies at $x = 18.71$ and the second at $x = 46.68$. For TWM, we get four different peaks. These are at $x = 15.68$, 44.82, 48.55 and 111.71. The peak at $x = 111.71$ has the

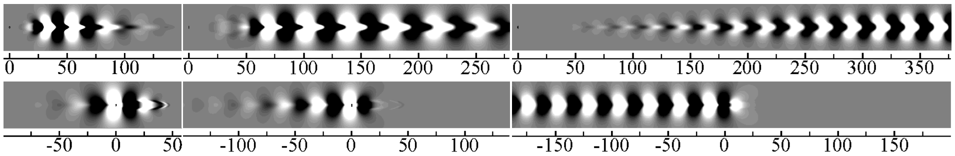

Figure 6.1: Real part of the cross-stream velocity field corresponding to direct eigenmodes (top) and adjoint eigenmodes (bottom) computed for $Re = 180$, $Ar = 0.25$ and $H = 100$. The three unstable eigenmodes are PWM (left), SWM (middle) and TWM (right). The darker shades of grey represent negative, while the lighter shades represent positive values.

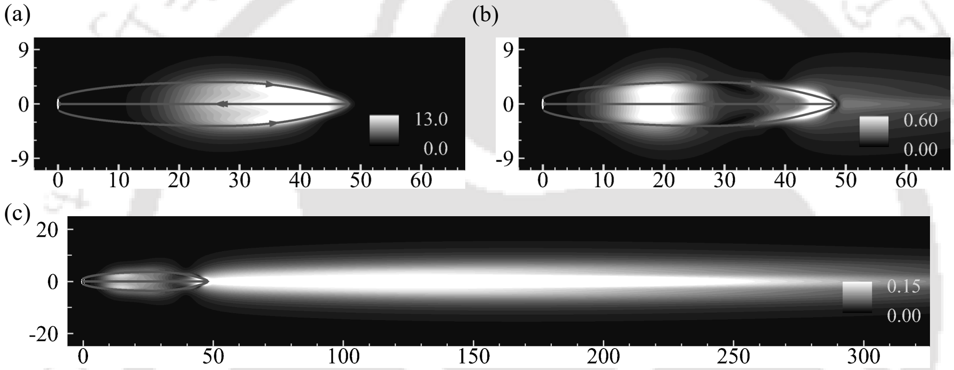

Figure 6.2: Sensitivity of the global eigenmodes at $Re = 180$ for $Ar = 0.25$: overlap region of the cross-stream velocity of (a) PWM, (b) SWM, (c) TWM.

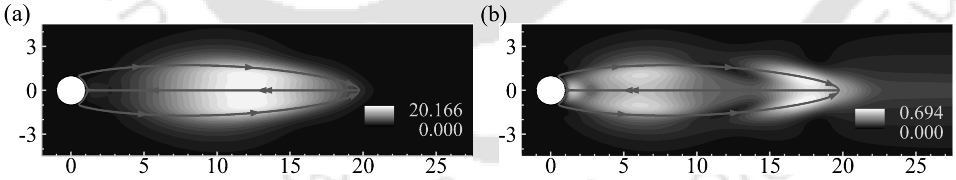

Figure 6.3: Sensitivity of the global eigenmodes at $Re = 150$ for $Ar = 1.0$: overlap region of the cross-stream velocity of (a) PWM, (b) SWM.

highest value in the overlap region, and therefore, is the most sensitive. Again, we could use one or more plates, placed about the location of the respective peaks, to suppress either SWM or TWM, or both.

Figure 6.3 shows the overlap region of the cross-stream velocity components of the direct and the adjoint modes corresponding to PWM and SWM. The modes

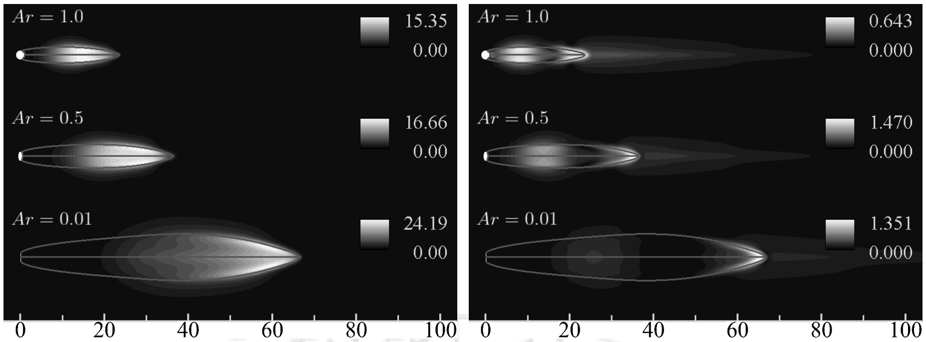

Figure 6.4: Sensitivity of the global eigenmodes at $Re = 180$ for $Ar = 1.0$, 0.5 and 0.01: overlap region of the cross-stream velocity of PWM (left), SWM (right).

are computed for $Re = 150$ flow past a circular cylinder with $H = 100$. For PWM, the maximum of the overlap region lies at $x = 11.95$. We therefore expect that a slip-plate placed on the centerline covering this region or more could suppress PWM. For SWM, three peaks in the overlap region appear. These are at $x = 1.47$, 6.13 and 17.78. Amongst these, the peak at $x = 17.78$ is the most sensitive. Again, we could use a single plate or more, placed at the location of the peaks, to suppress SWM. Interestingly, the peaks of the overlap for PWM and SWM lie inside the steady wake bubble.

In general, it is found that as the modes get affected by the variation of the parameters like Re, Ar and H, so do the corresponding overlap region and their peaks. We discuss the effect of these parameters on the overlap region and their peaks in more detail in subsequent sections

6.1 Effect of Ar

The change in aspect ratio significantly affects the overlap region of eigenmode and its peaks. Figures 6.4 and 6.5 show the overlap region of PWM, SWM and TWM at $Re = 180$ for $Ar = 1.0$, 0.5 and 0.01. It is observed that the points, at which the highest magnitude of the overlap region for PWM and SWM occur, lie inside the steady wake bubble, for all values of Ar. In contrast, the point corresponding to the highest magnitude of the overlap region for TWM lies outside the steady wake bubble and far from the cylinder. With the decrease in Ar, the locations of the maximum of the overlap region for PWM and SWM move away from the cylinder,

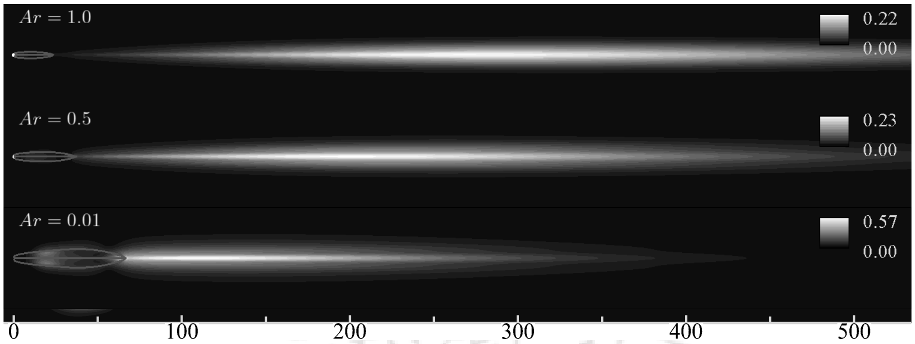

Figure 6.5: Sensitivity of the global eigenmodes at Re = 180 for Ar = 1.0, 0.5 and 0.01: overlap region of the cross-stream velocity of TWM.

whereas, the same for TWM comes close to the cylinder.

For Ar = 1.0, 0.5 and 0.01, the location of the maximum for PWM lies at x = 14.54, 27.98 and 60.36, respectively. For SWM, two different peaks appear. Both peaks recede in the downstream direction with the decrease in Ar. For Ar = 1.0, 0.5 and 0.01, the first peak appears at x = 8.15, 13.82, and 25.75, respectively. The second peak, which has the highest value in the overlap region, appears at x = 23.37, 35.30, and 65.58, respectively. It is also observed that the strength of the first peak of the overlap region for SWM decreases with the decrease in Ar. For TWM, four different peaks appear in the overlap region for each Ar. For Ar = 1.0, 0.5 and 0.01, the highest peak occurs at x = 269.97, 197.82 and 107.283, respectively. With the decrease in Ar, the highest peak moves close to the cylinder, while the other peaks moves away from the cylinder in the downstream direction. It is found that the variation trend of the overlap region with Ar is consistent over the Reynolds number range considered in this study. The overlap region results presented here is consistent with the change in the structure and location of the eigenmodes with Ar (see figures 5.10 and 5.11).

6.2 Effect of Re

Figure 6.6 shows the effect of Re on the overlap region for PWM and SWM, for Ar = 0.25. TWM becomes unstable at higher Re, and therefore, we do not have much data to show the trend for this mode. It can be observed that the increase in Re has significant effect on the location of the peak of the overlap region. The locations

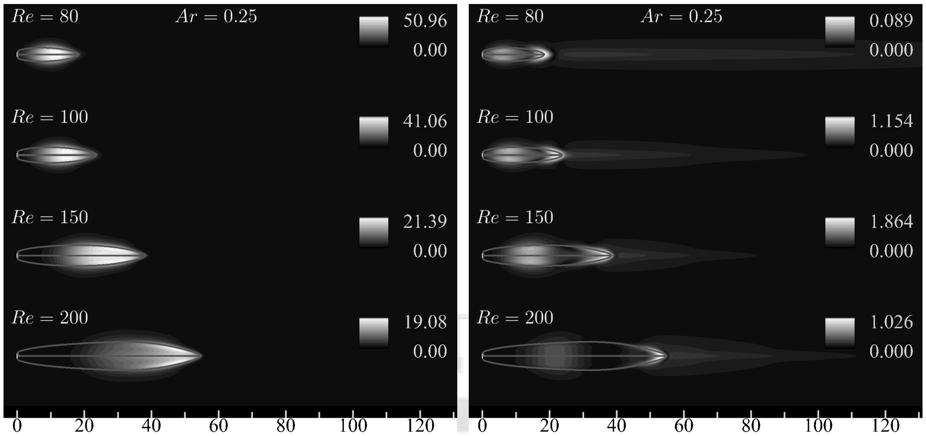

Figure 6.6: Sensitivity of the global eigenmodes for $Ar = 0.25$ at $Re = 80$, 100, 150 and 200: overlap region of the cross-stream velocity of PWM (left), SWM (right).

of the maximum, for the overlap regions for PWM and SWM, slowly move away from the cylinder in the downstream direction with the increase in Re. The peaks of the overlap region for PWM at $Re = 80$, 100, 150 and 200 lie at $x = 11.53$, 14.72, 26.51, 48.07, respectively. Similarly, for the mentioned Re, the first peak for SWM lies at $x = 4.84$, 7.84, 14.24, 21.84, respectively. The second peak, which has the highest value, lies at $x = 18.44$, 22.64, 37.44 and 53.43, respectively. The locations for the maximum of the overlap regions for PWM and SWM lie inside the steady wake bubble for the Re range studied in the present work. In case of SWM, it can be seen that the extent of the overlap region in the flow field first decreases with increase in Re from 80 to 150, and then increases with the further increase in Re upto 200. A similar trend appears in the effect of Re on the eigenmodes (see figure 5.9). The trend in the change with Re, for the overlap region, remains same for all Ar.

6.3 Effect of blockage

Figures 6.7 and 6.8 show the effect of blockage on the overlap region of the eigenmodes for $Re = 180$ flow past a cylinder having $Ar = 0.375$. Overall, with the increase in blockage, it is found that the location of the maximum of the overlap region moves close to the cylinder. The extent of the overlap region, up which it spreads in the flow field, decreases. Also, the width of the overlap region decreases

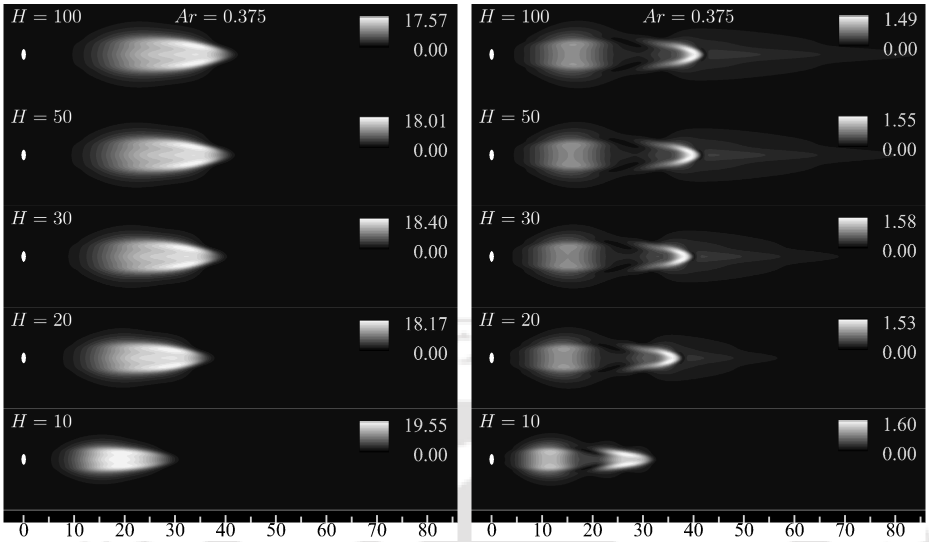

Figure 6.7: Sensitivity of the global eigenmodes at $Re = 180$ for $Ar = 0.375$: overlap region of the cross-stream velocity of PWM (left), SWM (right) with varying domain sizes.

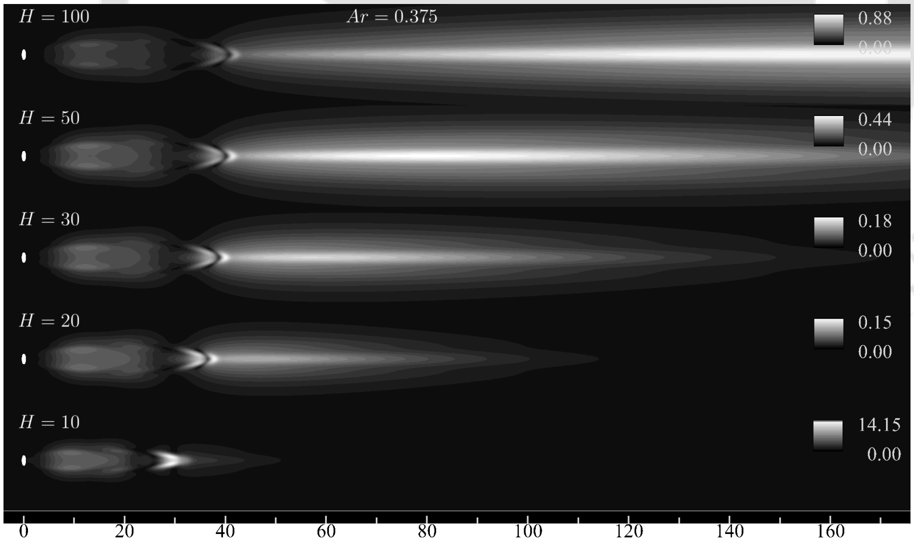

Figure 6.8: Sensitivity of the global eigenmodes at $Re = 180$ for $Ar = 0.375$: overlap region of the cross-stream velocity of TWM with varying domain sizes.

with the increase in blockage. For PWM, the location of the maximum moves from $x = 34.08$ to 18.92 with a change in H from 100 to 10. For SWM, the highest peak of the overlap region moves from $x = 40.16$ to 26.80 with change in H from 100 to

10. The most significant shift in the location of the maximum of the overlap region occurs for TWM. The highest value of the overlap region for TWM shifts from $x = 152.66$ to 29.75 with a change in H from 100 to 10. The variation trend of the overlap region with change in H remains same for all Ar and Re.

As discussed above, parameters like Re, Ar, and H significantly affect the overlap region and their peaks. In this connection, an interesting observation was made during our study. We found that the peak location of the overlap region for PWM comes closest to the location of the minimum of the base flow velocity on the centerline, for the case for which the growth rate was maximum. For example, first row of figure 5.1 shows the variation of the growth rate with Re for PWM, for different Ar. If we pick a particular Ar, we can find the Re for the maximum growth rate. Our results show that the peak location of the overlap region corresponding to this Re is closest to the location for the minimum in the base flow centerline velocity, compared to the peak locations for other Re. We should note that the minimum of the centerline velocity is the maximum of the reverse flow in the wake bubble. For other Re, the peak location of the overlap region shifts away from the minimum velocity point. This is, perhaps, the reason for a decrease in the growth rate with increase in Re beyond the maximum as shown in figure 5.1. This behaviour was found to hold true across all Ar and H used in the present study. Observations similar to that described above were also made by Kumar & Mittal [75] while investigating the role of convective modes in the far wake oscillations of a circular cylinder. They found that the core of the overlap region corresponding to the fastest growing convective mode comes closest to the minimum point of the centerline velocity of the time-averaged base flow.

What is said in the previous paragraph need not be true in general. The eigenvalue of a mode can be expressed as the integral of the product of the direct mode, the linear operator and the adjoint mode. Therefore, it is the integral which determines the contribution to the eigenvalue. Therefore, a large growth rate may not always be accompanied with the close proximity of the peak, of the overlap region, with the minimum velocity point. In fact, such correlations were not seen for SWM and TWM. These modes have more than one peak. So, we have a choice to make. The most sensitive peak for the fastest growing mode is not always the closest to the minimum velocity point.

As mentioned earlier, our aim here is to investigate the role of the individual modes in the development of the unsteady flow. We therefore suppress all other modes except the one which we want to study. We use a slip-plate on the wake centerline to effect passive control. Though a slip-plate is a hypothetical plate (having zero thickness and allows the flow to slip on its surface), it is advantageous to use it. First, it does not alter the steady base flow. And second, it has no boundary layer of its own. This allows minimum interference with the flow while suppressing a mode. However, plates of finite length produce effects which need not be always expected from the sensitivity analysis. Sometimes it is found that the length and location of a plate suitable to suppress a particular mode causes another mode, which is stable, to become unstable. This complicates the entire analysis. The sensitivity study presented above is unable to provide this information because it tells only about PWM, SWM and TWM. And, we do not know apriori which of the stable modes can become unstable on putting a plate on the centerline. We therefore need to carry out stability analysis with finite plates. Sensitivity study presented above would in this light be considered as study with infinitesimal plates. In the next chapter we discuss the effect of the length and location of slip-plates on the growth rate and frequency of the modes.

Indian Institute of Technology Guwahati

Chapter 7

Dynamics and control of the wake modes

In this chapter we investigate the role of the unstable eigenmodes in the development of the unsteady flow and seek connection of the structures in the flow with those present in the modes. We first conduct the linear stability analysis of the steady base flow with plates which are very small. Then, we determine the location of the plates for which the individual modes or their combination are suppressed. Finally, we determine the flow that would develop when the individual modes or their combinations are allowed to grow. We conduct this study for $Re = 150$ flow past a circular cylinder and $Re = 180$ flow past an elliptic cylinder ($Ar = 0.25$).

Towards the end of the last chapter, we concluded that the structural sensitivity results are not enough to understand the flow behaviour when a plate of finite length, even though small, is placed in the flow field. This is not unexpected as the analysis assumes the perturbations to be infinitesimal. In this chapter, we show that the linear stability computation with small slip-plates placed on the wake centerline is more suited for the present study and gives more information than the structural sensitivity analysis. A slip-plate is a hypothetical plate which allows the flow to slip along its surface and prevents the flow normal to it. Serson *et al.* [72] discussed the advantages of using the slip boundary condition over the no-slip boundary condition. They showed that the effect of the boundary condition is restricted to a thin boundary layer near the plate and the slip-wall boundary condition is also able to capture most of the flow physics. They encouraged the use

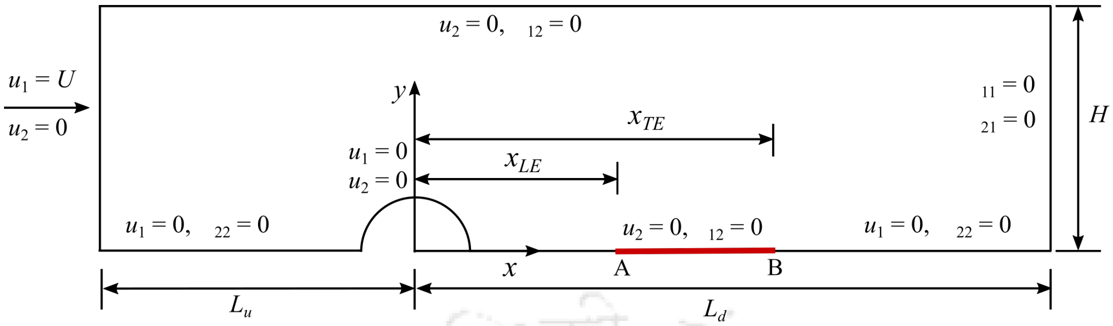

Figure 7.1: Flow past a half-cylinder: domain description and boundary conditions. L_u and L_d are the locations of the upstream and downstream boundaries, H the half-width of the domain, AB the slip-plate, x_{LE} the location of the leading edge and x_{TE} the location of the trailing edge. All distances are measured from the centre of the cylinder.

of slip-wall boundary conditions for the fact that it reduces the computational cost of the simulations.

7.1 The computational domain and boundary conditions

We take advantage of the fact that the eigenmodes discussed in this study possess symmetry about the wake centerline (see figure 5.7). We, therefore, use half of the domain to carry out the computations. This reduces the computational cost. The description of the half-cylinder computational domain and the boundary conditions used in the present study are shown in figure 7.1. L_u and L_d denote the distance of the upstream and the downstream boundaries, respectively, from the centre of the cylinder. H (domain half-width) is the distance between the upper boundary and the centerline. The upstream and downstream boundaries are located sufficiently far from the cylinder and have no significant influence on the overall flow field. In all computations, the value of L_u, L_d and H are 200, 700 and 100, respectively.

The boundary conditions used to compute the steady flow and conduct the linear stability analysis using the half-cylinder domain are as follows. For steady flow computations, a free-stream value is assigned to the velocity at the upstream boundary.

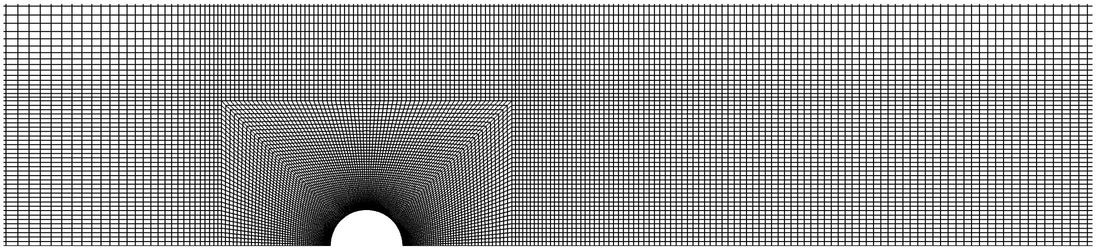

Figure 7.2: A closed up view of the finite element mesh used for flow past a half-cylinder. The mesh resolution of the half-cylinder is same as mesh M1 of full cylinder.

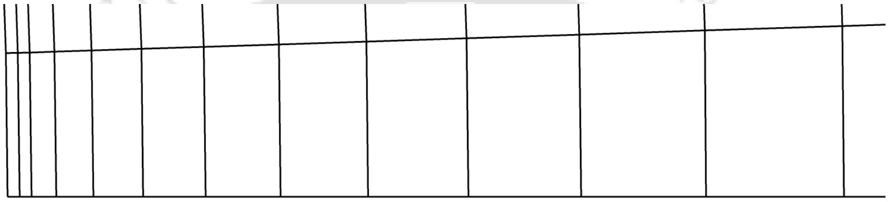

Figure 7.3: Zoom in view of the finite element mesh depicting the increasing trend of the element size.

At the downstream boundary, a Neumann-type boundary condition for the velocity is specified that corresponds to stress-free conditions. On the upper and lower (centerline) boundaries, the component of velocity normal to and the component of stress vector along these boundaries are prescribed a zero value. The cylinder surface is a no-slip boundary. The boundary conditions for the linear stability computation are the same except at the inflow boundary and on the centerline. At the inflow boundary, the velocity components are set to zero. Except on the plate where we have zero shear stress and no cross flow, everywhere else on the centerline (see figure 7.1) normal stress and streamwise velocity are set to zero. These boundary conditions allow computation of the modes which have symmetry opposite to that of the base flow. Since the modes in this study already possess this symmetry, we are able to obtain them with the half-cylinder domain.

All the unsteady computations with plate have been performed with the full cylinder. The time step size, $\Delta t = 0.01$, is used for computing the unsteady flow. The initial conditions used for computing the unsteady flow are mentioned during the discussion.

The finite element mesh used for computations with the half-cylinder has the same resolution as the mesh M1 used for the full cylinder (see figure 7.2). The half-cylinder mesh has 125193 nodes and 123827 quadrilateral elements. In this chapter, the slip-plate dimension is kept same as the element size. The zoom-in view of the finite element mesh along the centerline (see figure 7.3) shows the increasing trend of element size when we move away from the cylinder.

7.2 Mode suppression in $Re = 150$ flow past a circular cylinder

In this section, we first present the linear stability results obtained with plate(s) which are very small and are placed on the wake centerline. Later, we use these results to obtain the length and location of the plates which selectively suppress one or more of the unstable modes. A small plate causes minor change in the growth rate and frequency of the modes. By determining the growth rate of the linear modes, obtained from the linear stability analysis with the plate(s) located at different points on the centerline, we find the region which is most sensitive, and also, we come to know whether we expect a decrease or an increase in the growth rate there. In addition, we discover locations where putting a plate can cause some of the stable modes to become unstable. Appearance of the new modes (which are otherwise stable) was seen for $Re = 180$, $Ar = 0.25$. We present these results in the later sections.

Figure 7.4 presents the linear stability results for $Re = 150$ flow past a circular cylinder. The length of the slip-plate is equal to the size of a single finite element (see figure 7.3) and is not same at all locations because the element size increases as we move away from the cylinder. This however is not a cause of concern as the plate lengths are small (between 0.002 and 0.2953). The growth rate and St curve presented in the figure show a non-monotonic variation with the leading edge location (x_{LE}) of the slip-plate. The growth rate of the modes without plate is shown as a dashed line. For PWM, the growth rate curve has a significantly large trough with its minimum at a location close to $x_{LE} = 12$. This indicates that a plate placed in this region is most effective in suppressing PWM. Here we have a close match with the results discussed in the previous section where the peak of the overlap region for PWM (see figure 6.3) was found to be at $x = 11.95$. The St curve shows

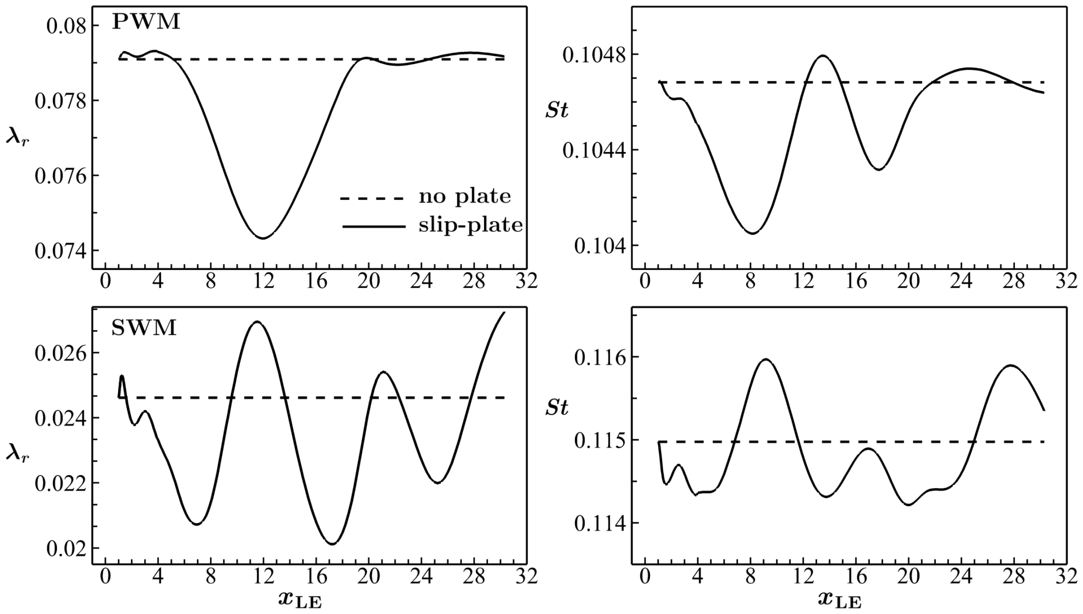

Figure 7.4: Variation of the growth rate (left) and St (right) for PWM (top) and SWM (bottom) with the leading edge location (x_{LE}) of slip-plate for $Re = 150$ flow past a circular cylinder.

significant oscillations with x_{LE}. We should note that the changes in the growth rate and St are actually very small. However, compared to the changes observed at other locations these are referred as ”significant”. For SWM, the oscillation in the growth rate curve is significant. The locations of the three out of four minima in figure 7.4 matches closely with the peak locations in the overlap region of SWM (see figure 6.3) mentioned in the previous section. The lowest point on the curve is at $x_{LE} = 17.11$ which is close to the location ($x = 17.78$) of the most sensitive peak. The presence of multiple minima points allows us to use more than one plate, if needed, to suppress the eigenmode. At this point a question may be asked: if there is a close agreement with the sensitivity results presented earlier, what is the necessity for conducting this laborious task? As mentioned earlier, the real necessity of the present analysis is realized when we find a few stable modes becoming unstable after putting the plate.

Based on the growth rate curve of PWM and SWM shown in figure 7.4, we select four different LE locations to suppress one of the eigenmodes or both. The locations are $x_{LE} = 6.02$, 9.15, 12.24 and 16.03. For each of the chosen x_{LE}, we study the

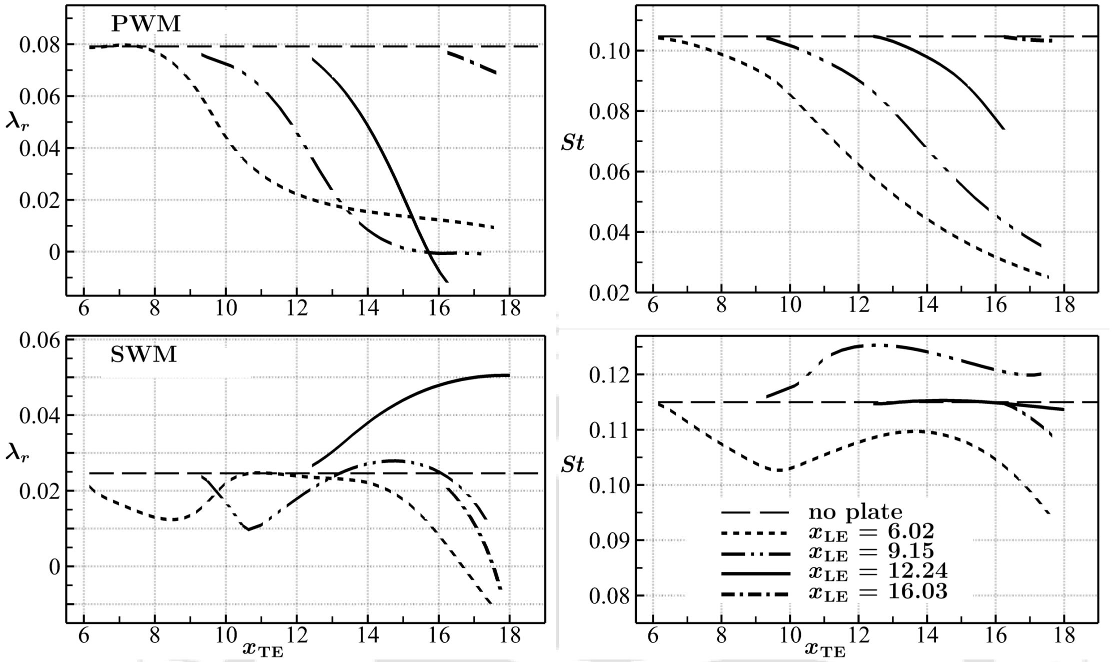

Figure 7.5: Variation of the growth rate (left) and St (right) for PWM (top) and SWM (bottom) with the trailing edge location (x_{TE}) of slip-plate for Re = 150 flow past a circular cylinder.

effect of the increase in plate length on the modes. Figure 7.5 displays the variation of the growth rate and St of PWM and SWM with the trailing edge location (x_{TE}) of the slip-plate. It is observed that for x_{LE} = 6.02, 9.15 and 12.24, the growth rate of PWM decreases with increase in plate length and eventually becomes negative. The plate lengths for which the growth rate of the PWM becomes negative are 14.80, 6.45 and 3.57, respectively. The plate length is calculated as $x_{TE} - x_{LE}$. Amongst the cases presented, the plate length required to suppress PWM is smallest for x_{LE} = 12.24. This is because, the plate is close to the location of the minimum of the growth rate curve for PWM shown in figure 7.4. For the plate lengths chosen, growth rate of SWM remains positive for x_{LE} = 9.15 and 12.24. It eventually becomes negative for x_{LE} = 6.02 and 16.03. For x_{LE} = 12.24, the growth rate increases with increase in plate length. This is counter intuitive. However, it can be explained from figure 7.4. At x_{LE} = 12.24, the growth rate is higher than the no plate line. Hence, increasing the plate length causes increase in the growth rate of SWM. For x_{LE} = 16.03, the plate length required to suppress SWM is only 1.75.

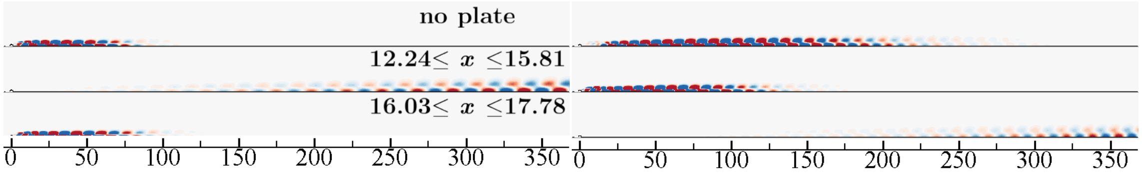

Figure 7.6: Vorticity field for PWM (left) and SWM (right) obtained with a slip-plate on the centerline for $Re = 150$ flow past a circular cylinder. Variable x shows the region on the centerline where the plate is present. The vorticity fields shown here are plotted in the range -0.001 to 0.001.

This is because, $x_{LE} = 16.03$ is close to the minimum of the growth rate curve of SWM shown in figure 7.4. St decreases monotonically for PWM, whereas for SWM, there is a nonmonotonic decrease for all LE locations except for $x_{LE} = 16.03$.

As expected, we have been able to obtain the length and location of the plate for which the modes are selectively suppressed. Results presented in figure 7.5 show that for $x_{LE} = 16.03$ and plate length 1.75, SWM is suppressed while PWM remains unstable. If we use this plate, we can study the effect of PWM exclusively in the unsteady flow. For $x_{LE} = 12.24$ and plate length 3.57, PWM is suppressed and SWM remains unstable. Hence, with this plate, we can study the role of SWM in the unsteady flow. For $x_{LE} = 6.02$ and plate length 14.80, both eigenmodes are suppressed simultaneously. The flow is expected to become steady.

Figure 7.6 shows a comparison of the structure of PWM and SWM obtained from the linear stability analysis with slip-plates having (x_{LE}, length) = (12.24, 3.57) and (16.03, 1.75) with those obtained without plate. Only upper half of the domain is used for computation. The condition specified on the centerline of the domain is no normal stress and zero streamwise component of velocity, except on the plate where we have zero shear stress and no cross flow.

For plate with (x_{LE}, length) = (12.24, 3.57), PWM is suppressed while SWM grows in strength. Figure 7.6 shows that PWM recedes downstream and the extent to which it spreads in the downstream direction also increases. We have noticed similar behaviour for weaker modes in the previous chapter 5 where the linear stability results are presented. The vortical structures in the mode become larger in size corresponding to a decrease in St. SWM, on the other hand, comes close to the cylinder and the extent to which it spreads in the wake reduces. This is again similar to the behaviour observed earlier for the stronger modes. For plate with

(x_{LE}, length) = (16.03, 1.75), SWM is suppressed. We see that the mode recedes downstream as well as the extent to which it spreads in the wake increases. The size of the vortical structure also increases with a corresponding decrease in St. PWM, on the other hand, shows very little change.

7.3 Role of PWM and SWM in $Re = 150$ flow past a circular cylinder

We now compute the flow which evolves if only one of the mode is allowed to grow. This would enable us to assess the role of each mode in the flow evolution and also allow us to see the resulting fully developed flow. In order to compute the flow with one of the modes suppressed, we place the plate at the appropriate location on the centerline. For example, if we want the evolution with SWM suppressed, plate with (x_{LE}, length) = (16.03, 1.75) is used. The resulting fully developed flow is represented as $\mathrm{SWM}_{\mathrm{SP}}$. It should be noted that this flow is a result of the growth of PWM. Similarly, for the evolution with PWM suppressed, plate with (x_{LE}, length) = (12.24, 3.57) is used. The resulting fully developed flow is represented as $\mathrm{PWM}_{\mathrm{SP}}$ and is the result of the growth of SWM. We compute $\mathrm{PWM}_{\mathrm{SP}}$, $\mathrm{SWM}_{\mathrm{SP}}$ and flow past a circular cylinder without plate. The initial condition used for $\mathrm{PWM}_{\mathrm{SP}}$ is the sum of the steady flow and SWM which we obtain from the corresponding linear stability analysis. Similarly, the initial condition for $\mathrm{SWM}_{\mathrm{SP}}$ is the sum of the steady flow and PWM which we obtain from the corresponding linear stability analysis. For flow without plate, we begin the computation with potential flow solution.

Figure 7.7 shows the time history of C_D and C_L for four different cases. These are flow without plate, $\mathrm{SWM}_{\mathrm{SP}}$, $\mathrm{PWM}_{\mathrm{SP}}$ and the steady flow obtained by suppressing both the modes. Since we begin the computation with one of the eigenmodes (having small amplitude), the initial evolution is expected to be linear. This is confirmed from the oscillation frequency computed with fast Fourier transform (FFT) of C_L versus time data. For $\mathrm{SWM}_{\mathrm{SP}}$, the initial flow frequency is found to be 0.104, which is equal to the frequency of PWM. This ensures the presence of only PWM in the flow. Similarly, for $\mathrm{PWM}_{\mathrm{SP}}$, the initial flow frequency is found to be 0.115, which is same as the frequency of SWM. This confirms that initially, this flow contains only SWM. As the flow evolves, and the nonlinear effect becomes prominent, vortex

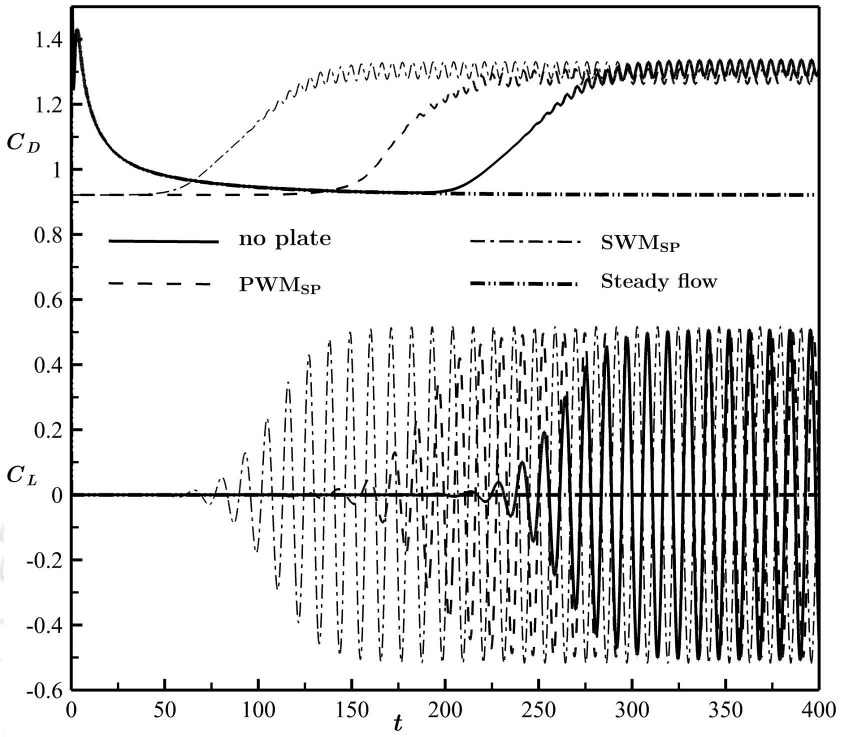

Figure 7.7: Time histories of the lift and drag coefficients for PWM$_{SP}$, SWM$_{SP}$, flow without plate and the steady flow for Re = 150, Ar = 1.0 and H = 100.

shedding frequency increases significantly. Another observation which can be made from figure 7.7 is that the nonlinear effects kick in early for SWM$_{SP}$ because of the higher growth rate of PWM.

In table 7.1, the characteristics of the fully developed SWM$_{SP}$ and PWM$_{SP}$ are compared with flow without plate and also with the steady flow obtained by suppressing both the modes. Also, a comparison of the flow without plate is presented with the results reported in the literature. $\overline{C_D}$, $C_{D'}$ and $C_{L'}$ represent the mean C_D, amplitude of the fluctuating components of C_D and C_L data, respectively. It is observed that the values reported for flow without plate are in close agreement with the ones reported by Kumar & Mittal [75]. We further notice that, compared to PWM$_{SP}$, the values obtained for SWM$_{SP}$ are closer to the corresponding values for flow without plate. The near wake of SWM$_{SP}$ oscillates with frequency 0.1829 which is same (up to four decimal places) as the frequency for flow without plate. For PWM$_{SP}$, the near wake is found to oscillate with frequency 0.1795. It seems that if only PWM were present, flow features would resemble the no plate case more

Table 7.1: Mean drag coefficient ($\overline{C_D}$), amplitude of the fluctuating part of the drag ($C_{D'}$) and lift ($C_{L'}$) coefficients and Strouhal number (St) for PWM$_{\mathrm{SP}}$, SWM$_{\mathrm{SP}}$, flow without plate and the steady flow (obtained by suppressing PWM and SWM) for $Re = 150$, $Ar = 1.0$ and $H = 100$. Results from studies published earlier are also presented.

Studies	Mode suppressed	$\overline{C_D}$	$C_{D'}$	$C_{L'}$	St
Zhang *et al.* [96]	–	1.410	–	0.403	0.192
Liu *et al.* [97]	–	1.334	0.030	0.530	0.182
Kumar & Mittal [75]	–	1.313	0.026	0.518	0.182
no plate	–	1.3126	0.0250	0.5090	0.1829
$12.24 \leq x \leq 15.81$	PWM	1.2860	0.0234	0.4994	0.1795
$16.03 \leq x \leq 17.78$	SWM	1.3054	0.0260	0.5175	0.1829
$6.02 \leq x \leq 20.83$	PWM & SWM	0.9215	0	0	–

closely than the flow with only SWM. In other words, PWM alone, perhaps, can evolve into the same von Kármán vortex street which we get for the flow without plate. This is because PWM dominates the evolution for flow without plate.

Figure 7.8 displays the vorticity field of the fully developed flow for four different cases. Unlike that for flow without plate, for PWM$_{\mathrm{SP}}$, von Kármán vortices appear down to a considerable distance in the wake. This is because SWM extends to a much longer distance compared to PWM. For SWM$_{\mathrm{SP}}$, the extent of the vortex street is shorter. This is further confirmed from the cross-stream velocity oscillations on the centerline shown in figure 7.9. The cross-stream velocity for SWM$_{\mathrm{SP}}$ decays faster compared to PWM$_{\mathrm{SP}}$.

Figure 7.10 shows the frequency spectra of cross-steam velocity and the amplitude decay of the von Kármán vortex shedding frequency with the downstream distance. We can notice the presence of peaks at the prominent flow frequencies mentioned earlier. It is observed that the peaks decrease in height as we move away from the cylinder. In the far wake, the broadband of frequencies appears, which shows the presence of secondary vortex street in the flow. Figure 7.10 (d) shows a

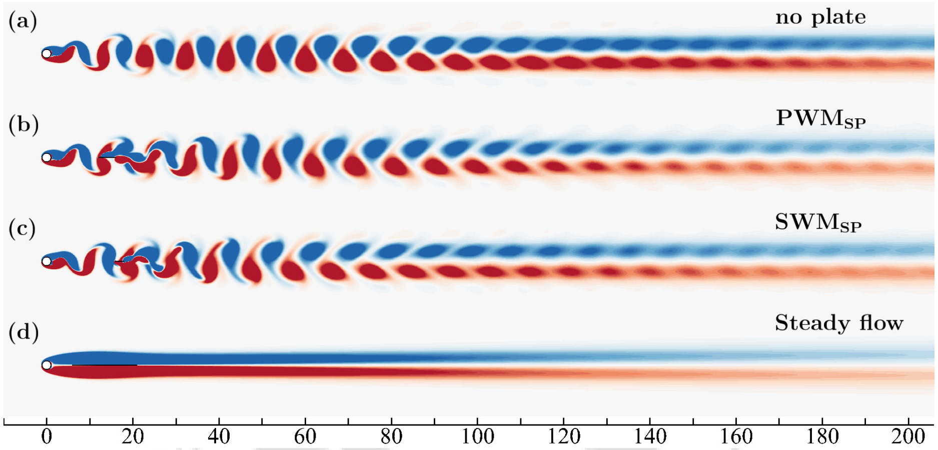

Figure 7.8: Vorticity field of the fully developed unsteady flow past a cylinder for $Re = 150$ and $H = 100$ for (a) flow without plate (PWM & SWM are unstable), (b) PWM$_{SP}$, (c) SWM$_{SP}$, (d) steady flow obtained by suppressing PWM & SWM.

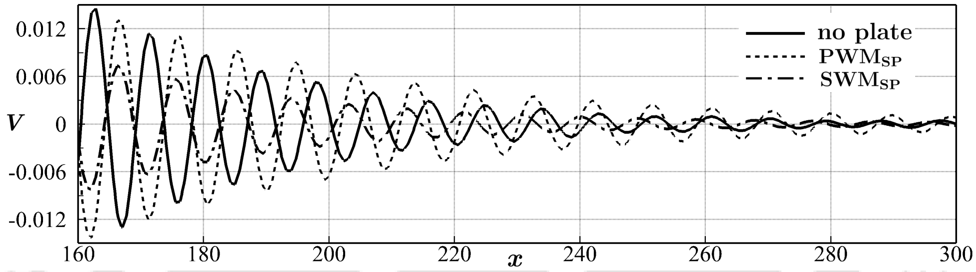

Figure 7.9: Cross-stream velocity variation on the centerline for $Re = 150$ flow past a circular cylinder.

comparison of the decay rate for the three different flows. For flow without plate, the decay rate is 0.0233 decades/D. This is in good agreement with that reported by Kumar & Mittal [75], which is 0.0235 decades/D. For SWM$_{SP}$, the decay rate is 0.0221 decades/D, which is close to that for flow without plate. The decay rate for PWM$_{SP}$ is 0.0191 decades/D. The straight line depicting the amplitude decay crosses the 10^{-3} value at $x \sim 489$ for flow without plate. For SWM$_{SP}$ it crosses at $x \sim 486$. The decay rate for PWM$_{SP}$ is smaller and so the crossover point is at $x \sim 573$. This again shows that the oscillations in PWM$_{SP}$ extend to a larger distance downstream.

The results presented above conclusively establish that PWM and SWM lead to slightly different fully developed flows. The oscillation frequency and the extent of

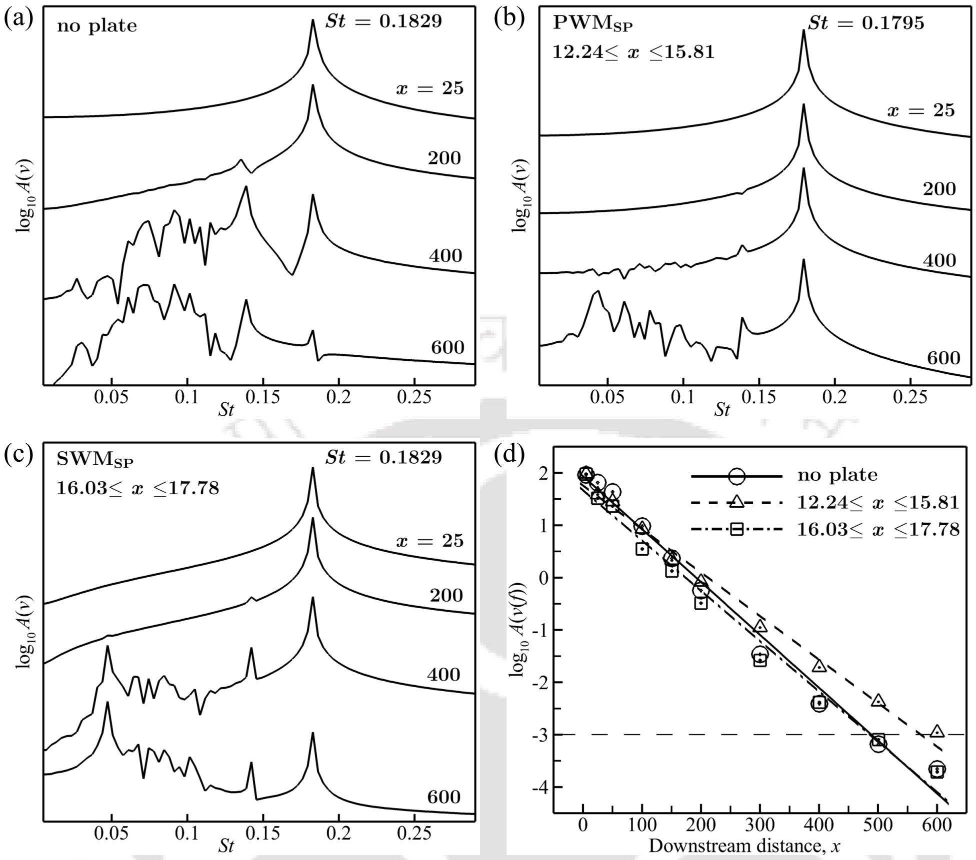

Figure 7.10: Frequency spectra of the cross-stream velocity for $Re = 150$ flow past a circular cylinder at various locations along the wake centerline: (a) no plate, (b) $\mathrm{PWM_{SP}}$, (c) $\mathrm{SWM_{SP}}$, (d) streamwise variation of the amplitude of the wake oscillation corresponding to the three cases.

the vortex street in the wake, due to these modes, are not same. In the next section we present the case where PWM, SWM and TWM are all unstable. The natural question regarding the possible flow features which would develop, when either of these modes or their combination is allowed to grow, is addressed.

7.4 $Re = 180$ flow past $Ar = 0.25$ cylinder

Flow past an elliptic cylinder with $Ar = 0.25$ at $Re = 180$ is associated with three unstable eigenmodes. Here, we study the effect of these modes in the fully developed flow. As before, we first conduct the linear stability analysis of steady base flow with

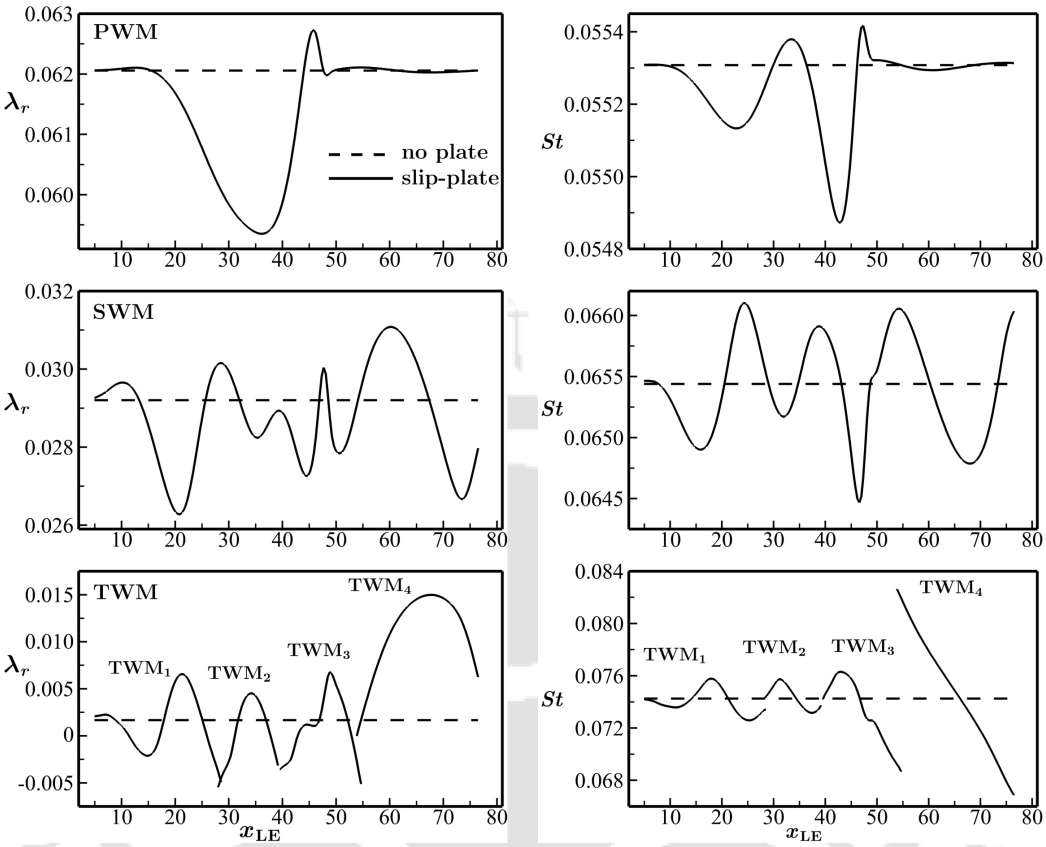

Figure 7.11: $Re = 180$ flow past an elliptic cylinder with $Ar = 0.25$: variation of the growth rate (left) and St (right) for PWM (top), SWM (middle) and TWM (TWM$_1$, TWM$_2$, TWM$_3$ and TWM$_4$; bottom), with respect to the leading edge location (x_{LE}) of slip-plates of one element size (minimum length = 0.113, maximum length = 0.473) placed on the wake centerline.

a slip-plate of the size of one element placed at various locations on the centerline. Figure 7.11 shows the variation of the growth rate and the Strouhal number of the eigenmodes with different LE location of the slip-plate. The growth rate curve of the eigenmodes varies nonmonotonically with the location of the slip-plate. The horizontal dashed line shown in the figure represents the value obtained without plate. For PWM, we see a relatively large trough with the minimum at x_{LE} = 36.19, which is inside the overlap region of PWM given by the structural sensitivity study (see figure 6.2). For SWM, it is found that the growth rate curve has multiple minima which lie at x_{LE} = 20.84, 35.22, 44.39, 50.73 and 73.67. Placing one or more of the slip-plates at the locations of minima would help us in suppressing the mode. In the growth rate curve of TWM we find, unlike PWM and SWM, several kinks. If we look at the corresponding points on the St curve, we find that there are sudden jumps. This is possible if we have modes other than TWM becoming unstable due to the presence of the slip-plate. We have marked these as TWM$_1$, TWM$_2$, TWM$_3$ and TWM$_4$. At the location of the kinks we notice the cross-over of curves from adjacent modes. Appearance of such kinks/cross-over points is not possible if the curve corresponds to the same mode throughout. We further note that TWM$_1$ is same as TWM. This can be verified from the extremely small change in the growth rate and St for x_{LE} close to the cylinder surface. Close to the cylinder surface, the slip-plates have very small length. This causes very small change in the growth rate and St of the modes.

From the present study it is interesting to find that there are modes in the flow which become unstable on putting a slip-plate at certain locations on the centerline. This is counter intuitive. We could not have guessed this from the structural sensitivity study presented earlier. This is because, the sensitivity study was done only for the unstable modes. One may think of computing some of the rightmost stable modes and carry out the structural sensitivity analysis to find those which could become unstable on putting a plate on the centerline. However, we do not know apriori which of the stable modes can become unstable unless we compute a large number of them, which is quite challenging for large matrix systems.

The structure of the modes presented in figure 7.11 are shown in figure 7.12. The leftmost column shows the structure of PWM along with the length and location of the single element plates used in figure 7.11. The middle column shows the structure of SWM. The rightmost column shows the structure of TWM, TWM$_1$, TWM$_2$, TWM$_3$ and TWM$_4$. As mentioned earlier, TWM is same as TWM$_1$. The modal structure of TWM$_1$, TWM$_2$ and TWM$_3$ are very much similar to each other. TWM$_4$ seems slightly different. It is actually stronger than the others and therefore appears close to the cylinder.

We now place one or more slip-plates on the centerline to suppress PWM, SWM, TWM individually or their combination. For example, in order to suppress PWM, we can place a plate of suitable length about $x = 36.19$, which is the minimum point in its growth rate curve. From figure 7.11 we see that for any x_{LE} there are at the most three unstable modes. After investigating several possibilities regarding the length and location of slip-plate(s) required to suppress the eigenmodes, we

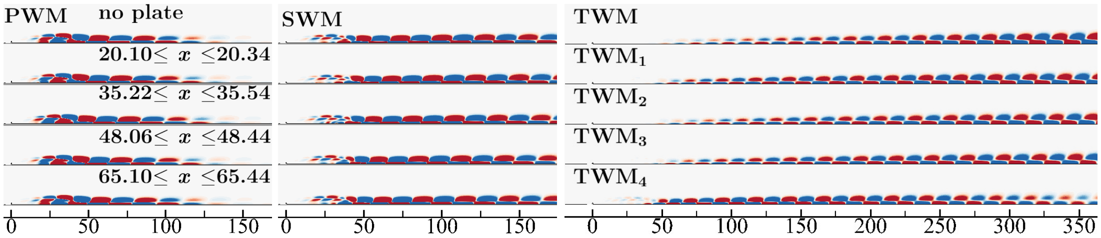

Figure 7.12: Vorticity field for PWM (left), SWM (middle) and TWM (TWM_1, TWM_2, TWM_3 and TWM_4; right) corresponding to figure 7.11. The dimensions of the single element plate used are also presented in the figure.

identify a few cases. The choice made depends on the mode(s) which we wish to suppress. Their details are given in table 7.2. While presenting the data in this table we use the term "suppressed" only for the modes which are unstable without the introduction of the plate and become stable when we insert the plate. Obviously, these are PWM, SWM and TWM or TWM_1. Other modes which become unstable on putting the plate at different locations on the centerline are TWM_2, TWM_3 and TWM_4. Unless stated otherwise these modes are to be considered stable. First case in table 7.2 corresponds to the suppression of PWM. We have used a plate with (LE, TE) = (34.9, 43.67). It turns out that, with this plate, TWM is also suppressed. SWM remains unstable. Interestingly, TWM_2 becomes unstable; TWM_3 and TWM_4 remain stable. This is consistent with the growth rate curve shown in figure 7.11. We can see that if we take a small plate with $x_{LE} = 34.9$, TWM_2 becomes unstable. On increasing the plate length we trace the growth rate curve (not shown here) till $x_{TE} = 43.67$ and thus arrive at the conclusion. Similarly, we make conclusions about other cases shown in table 7.2. When we have multiple plates, we increase the plate length of the first plate till it reaches the desired length. Then, we increase the length of the second plate, and so on. In this way, we are able to trace and identify the modes which are unstable/stable. We may note from table 7.2 that the fourth case also corresponds to the suppression of PWM and TWM. Here, however, we manage to allow the growth of only SWM. In the fifth case we suppress SWM and TWM and allow the growth of only PWM. From our calculations it was not possible to determine the plate length and location for which TWM is the only unstable mode. Table 7.3 shows the growth rate and Strouhal number of the modes which are unstable for the cases shown in table 7.2.

Table 7.2: $Re = 180$ flow past an elliptic cylinder with $Ar = 0.25$: details of the region occupied by the slip-plate(s) on the wake centerline and the modes suppressed in the corresponding cases. np is number of plate(s) used.

Case	Modes suppressed	Unstable modes	np	plate location
1	PWM & TWM	SWM & TWM$_2$	1	$34.90 \leq x \leq 43.67$
2	SWM	PWM & TWM	2	$20.59 \leq x \leq 24.66$, $43.67 \leq x \leq 48.44$
3	TWM	PWM & SWM	1	$28.54 \leq x \leq 28.83$
4	PWM & TWM	SWM	6	$12.99 \leq x \leq 14.17$, $16.03 \leq x \leq 20.10$, $22.07 \leq x \leq 26.01$, $28.25 \leq x \leq 30.29$, $33.01 \leq x \leq 48.44$, $53.85 \leq x \leq 55.45$
5	SWM & TWM	PWM	5	$14.98 \leq x \leq 17.78$, $20.59 \leq x \leq 24.66$, $39.84 \leq x \leq 41.56$, $43.67 \leq x \leq 48.44$, $53.85 \leq x \leq 56.25$
6	PWM & SWM	TWM$_3$	5	$12.99 \leq x \leq 14.17$, $16.03 \leq x \leq 20.10$, $22.07 \leq x \leq 27.12$, $28.25 \leq x \leq 32.09$, $33.01 \leq x \leq 48.44$
7	PWM, SWM & TWM	–	1	$10.13 \leq x \leq 69.99$

Flow at $Re = 180$ for $Ar = 0.25$ is highly nonlinear and the shedding pattern in the wake cannot be directly related to the unstable modes in the flow. We therefore

Table 7.3: Growth rate (λ_r) and St of the unstable eigenmodes for various cases shown in Table 7.2. OUM represents the other unstable mode.

	Case 0, none (no plate)		Case 1, $\mathrm{PWM_{SP}}$ & $\mathrm{TWM_{SP}}$	
	λ_r	St	λ_r	St
PWM	0.06205	0.05530	–	–
SWM	0.02920	0.06543	0.03292	0.05829
OUM	0.00167	0.07425 (TWM)	0.02331	0.07088 ($\mathrm{TWM_2}$)
	Case 2, $\mathrm{SWM_{SP}}$		Case 3, $\mathrm{TWM_{SP}}$	
	λ_r	St	λ_r	St
PWM	0.06124	0.05016	0.06006	0.05525
SWM	–	–	0.03015	0.06552
OUM	0.03064	0.07933 (TWM)	–	–
	Case 4, $\mathrm{PWM_{SP}}$ & $\mathrm{TWM_{SP}}$		Case 5, $\mathrm{SWM_{SP}}$ & $\mathrm{TWM_{SP}}$	
	λ_r	St	λ_r	St
PWM	–	–	0.05583	0.04800
SWM	0.00728	0.04394	–	–
OUM	–	–	–	–
	Case 6, $\mathrm{PWM_{SP}}$ & $\mathrm{SWM_{SP}}$		Case 7, $\mathrm{PWM_{SP}}$, $\mathrm{SWM_{SP}}$ & $\mathrm{TWM_{SP}}$	
	λ_r	St	λ_r	St
PWM	–	–	–	–
SWM	–	–	–	–
OUM	0.00395	0.08778 ($\mathrm{TWM_3}$)	–	–

Indian Institute of Technology Guwahati

look for similarity during the evolution of small perturbation. The evolution of small disturbances is linear and so we relate the disturbance field and the oscillation frequency with the mode structure and mode frequency, respectively. For example, in the fourth case presented in table 7.2, PWM and TWM are suppressed. Only SWM is unstable. Figure 7.13 compares the disturbance field obtained from the

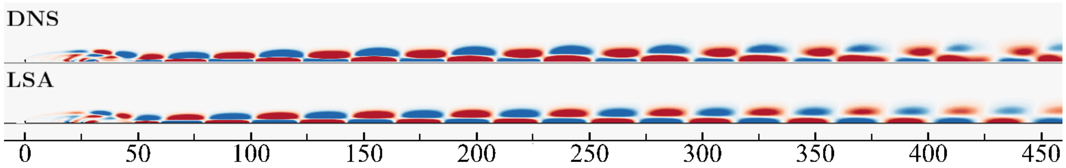

Figure 7.13: Comparison of the vorticity distribution of disturbance field obtained from unsteady computations (top) at t = 1350 with SWM obtained from the linear stability analysis (bottom) for case 4 shown in table 7.2.

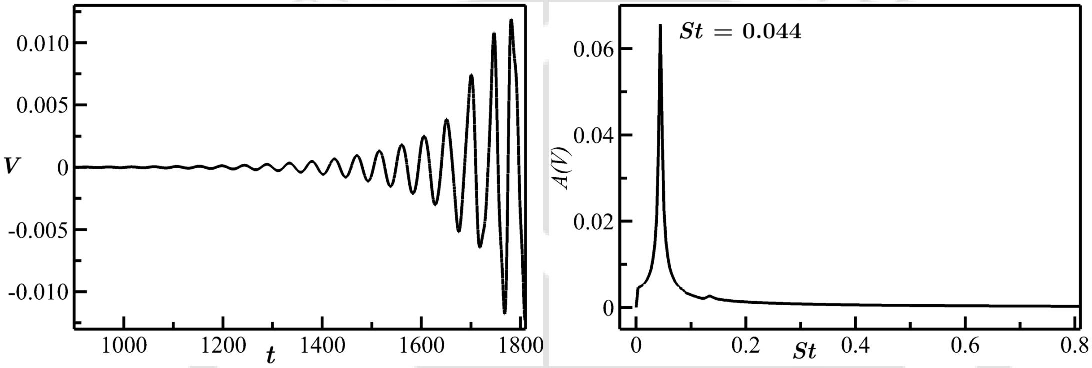

Figure 7.14: Time history (left) of the cross-stream component of velocity (sampled at $x = 5$, $y = 0$) and the corresponding frequency spectra (right; calculated from the data between t = 1000 and 1600) for case 4 shown in table 7.2.

initial evolution computed via unsteady computations with SWM obtained from LSA. There is great similarity in the vortical structures present in both the fields. The time history of the cross-stream velocity at coordinate (5, 0) and the oscillation frequency obtained from FFT of the same are shown in figure 7.14. The initial exponential growth of the velocity amplitude can be clearly seen. The St obtained from FFT is 0.044, very close to the St obtained from LSA for the corresponding case in table 7.3. The subsequent evolution to the nonlinear regime is the consequence of the growth of SWM. Figure 7.15 shows the flow field for the fully developed flow in this case. SWM referred to here has a much smaller growth rate and a smaller frequency compared to the SWM for flow without plate. However, since several plates have been used to isolate SWM, we do not expect the fully developed flow shown here to have features similar to that for the fully developed flow which is the consequence of the growth of only SWM (for flow without plate) with all other

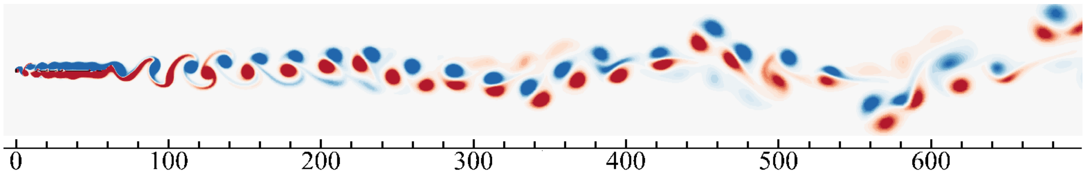

Figure 7.15: Vorticity field for the fully developed unsteady flow corresponding to case 4 shown in table 7.2.

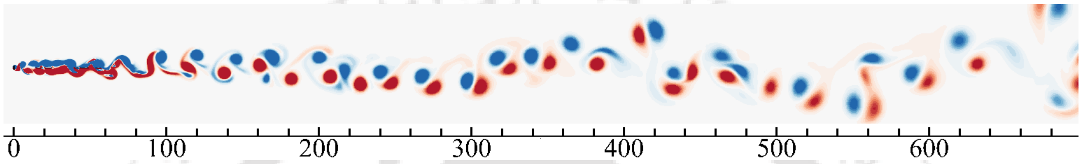

Figure 7.16: Vorticity field for the fully developed unsteady flow corresponding to case 5 shown in table 7.2.

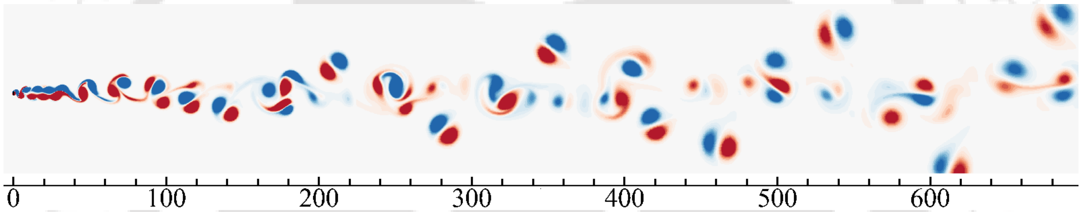

Figure 7.17: Vorticity field for the fully developed flow without plate at $Re = 180$.

modes absent.

We examine the fifth case from table 7.2 in a similar way as we did for the fourth case. Here, PWM is the only unstable mode. As seen previously, for the linear evolution, there is a good agreement of the mode structure and mode frequency with the structure of the disturbance field and its oscillation frequency, respectively. The fully developed flow is shown in figure 7.16.

Since in the fifth case only PWM is present, one may expect the flow to have some similarity with flow without plate. However, because of the presence of several plates things are different. Figure 7.17 shows the fully developed flow when there is no plate present in the field. The vortical structures seem to be larger and the oscillations stronger, compared to that in the flow shown in figure 7.16. FFT analysis of case 5 and flow without plate also do not show any agreement. The primary wake frequency for case 5 corresponds to $St = 0.1587$ whereas, the same for flow without plate is

0.1638. There are other dominant frequencies which are not close for the two flows. The amplitude decay trends of these frequencies in the wake are different. In fact, from figures 7.15 and 7.16, we see that flows in case 4 and case 5 appear close to each other. We therefore conclude that for flows where nonlinearity is not so prominent-the oscillation amplitudes are small, as found for $Re = 150$ flow past a circular cylinder-the above exercise could be useful in analysing the role of individual modes in the fully developed unsteady flow. However, when the nonlinearity is strong-the oscillation amplitude is large and the shedding pattern is complex-establishing a connection of the linear modes with the unsteady flow becomes difficult.

Indian Institute of Technology Guwahati

Chapter 8

Conclusions and scope for future work

In this thesis we conduct an analysis of two-dimensional steady flow past elliptic cylinders via linear stability analysis. A comprehensive investigation of the flow behaviour is carried out by varying the flow Reynolds number, the cylinder aspect ratio (Ar) and the domain width (H). Results are presented for $Re \leq 200$, $0.01 \leq Ar \leq 1.0$ and $10 \leq H \leq 100$. The governing flow equations have been solved using the stabilized finite element formulation. In certain cases, unsteady computations have been carried out to complement the stability results. The linear stability study is extended to investigate the sensitivity characteristics of the linear modes using slip-plates placed on the wake centerline. These results are utilized to link the behaviour of the unstable modes with the development of the nonlinear flow.

8.1 Conclusions

The main characteristics of the steady flow, like the bubble length, bubble width, separation Reynolds number, separation angle, drag coefficient, coefficients of the front and rear stagnation pressure, and the maximum vorticity on the cylinder surface have been computed. It is found from the present study that the wake bubble length and width increase monotonically with increase in Re/decrease in Ar. The strength of the vorticity in the shear layer originating from the top and bottom surface of the cylinder increases with the increase in Re/decrease in Ar. As a result,

Indian Institute of Technology

the bubble elongates and grows wider. We find an overall decrease in the bubble length and width with the decrease in the domain size. For $Re \leq 60$, the decrease is nonmonotonic with H, while it is monotonic for $Re > 60$. Though the critical Re, which separates the nonmonotonic and the monotonic change with H, depends on the Ar of the cylinder, a general estimate is presented here. The nonmonotonic variation is explained based on the dual effect of the blockage. First, when the side boundaries come close, the flow accelerates and the cylinder sees a relatively higher Re flow. Therefore, the bubble length and width increase. When the side boundaries are sufficiently close to the cylinder, the no-cross-flow condition compresses the bubble. As a result, the bubble length and width decrease. At higher Re, the wake bubble grows enough to ”feel” the presence of the side boundaries (no-penetration condition). Hence, there is a monotonic decrease with decrease in H. For the largest domain ($H = 100$), our curve fit equations for $Ar = 1.0$ show a linear variation of bubble length with Re. The variation deviates away from its linear nature as we decrease Ar and comes close to linearity as the blockage is increased. For $Ar = 1.0$ and $H = 100$, the bubble width increases linearly with $Re^{0.5}$. As we decrease the aspect ratio, the degree (in $Re^{0.5}$) of the curve fit equations increases.

The Reynolds number at the onset of flow separation from the cylinder surface has been determined. It is found that Re_S monotonically decreases with decrease in Ar. The variation of Re_S with H depends on Ar. For $0.5 \leq Ar \leq 1.0$, Re_S decreases monotonically with decrease in H. A non-monotonic variation with H is observed for $0.125 \leq Ar \leq 0.375$. For $0.01 \leq Ar \leq 0.0625$, Re_S monotonically increases with decrease in H. An explanation of the nonmonotonic variation is offered based on the dual role of the side boundaries.

The flow separation angle is found to monotonically increase with increase in Re/decrease in Ar. The variation with H depends on Ar. For $Ar = 1.0$ and 0.75, nonmonotonic variation is observed. For smaller Ar, θ_S increases monotonically with decrease in H. The curve fit equations are obtained for the largest domain size. It is found that θ_s varies linearly with $Re^{-0.1}$.

The pressure distribution on the cylinder surface is obtained for all cases studied. A smooth variation of C_P with θ is observed for $0.375 \leq Ar \leq 1.0$. For $0.01 \leq Ar \leq 0.25$, C_P is more or less constant except around $\theta = 90°$, where a spike with a dip to a large negative value is observed. Further, it is found that C_{p0} monotonically decreases with increase in Re/decrease in Ar. The C_{pb}, however, increases monotonically with increase in Re. With increase in Ar, the rear stagnation pressure increases at low Re and decreases at higher Re. These trends remain consistent for all H. With decrease in H, C_{p0} shows a monotonic increase while C_{pb} shows the opposite trend.

From our computations we observe that for each Ar, C_D and its components C_{Dp} and C_{Df}, monotonically decreases with increase in Re. For constant Re, C_{Dp} increases and C_{Df} decreases with decrease in Ar. Since, C_{Dp} dominates C_{Df}, C_D increases with decrease in Ar. For $H = 100$, the least-square fit to the drag coefficient data depicts a linear dependence on $Re^{-0.4}$ for C_{Dp} and a linear dependence on $Re^{-0.5}$ for C_D. C_{Df} is obtained as a linear function of $Re^{-0.6}$ for $0.25 \leq Ar \leq 1.0$ and as a linear function of $Re^{-0.8}$ for $0.01 \leq Ar \leq 0.125$. With decrease in H, C_D increases monotonically for all Re and Ar. The degree of polynomial in the curve fit equation for C_D versus $Re^{-0.5}$, increases with decrease in H.

The antisymmetric distribution of surface vorticity about the base point ($\theta = 180°$) is observed irrespective of change in Re, Ar and H. For $0.125 \leq Ar \leq 1.0$, a smooth variation of vorticity is observed, while for $0.01 \leq Ar \leq 0.0625$, a sharp increase in vorticity appears close to the cylinder shoulder ($\theta = 90°$). The magnitude of the maximum vorticity on the surface of the cylinder increases with increase in Re/decrease in Ar/decrease in H. For $H = 100$ and $0.25 \leq Ar \leq 1.0$, ω_{max} data is best represented as a linear function of $Re^{0.35}$, while the same for $0.01 \leq Ar \leq 0.125$ is represented as a second degree polynomial in $Re^{0.35}$. Least square fit for ω_{max} data for $Ar = 1.0$ is also presented for different domain size.

Linear stability analysis of steady flow past elliptic cylinders with varying aspect ratio has been conducted to get the unstable eigenmodes (PWM, SWM & TWM), their growth rates and the corresponding St. It is observed that these modes show a non-monotonic variation of growth rate with Re for low Ar cylinders. Low Ar cylinders exhibit higher growth rate at lower Re. As a result, the critical Reynolds number for the onset of vortex shedding decreases for smaller Ar. For PWM, the variation of St with Re is nonmonotonic for higher Ar. For SWM and TWM, St decreases monotonically with Re for all Ar. The trend in the variation of the growth rate with Re, for each Ar, remains the same for all domains, except the one with $H = 10$. In contrast, St shows the same trend for all H.

An interesting correlation exists between the structure of the eigenmodes and their growth rate and St. Modes which have larger growth rate reach close to the cylinder surface and have comparatively shorter length in the wake. Additionally, the size of the vortical structures present in a mode is large if its St is small and vice-versa. The difference in the structure of PWM, SWM and TWM amongst themselves and with change in Ar, Re and H can thus be related to the corresponding change in their growth rate and St.

The critical Re and the corresponding St for the onset of instability is reported for each Ar and H. For $Ar = 1.0$, the Re_c for PWM shows a non-monotonic variation with blockage similar to that reported by Kumar & Mittal [64]. However, for $Ar <$ 1.0, Re_c for PWM monotonically decreases with blockage. This possibly happens because the shear layer becomes stronger, as we decrease Ar, causing the flow to become more unstable. For SWM, Re_c increases with increase in blockage for Ar down to 0.5. Below this Ar, the Re_c variation with blockage is non-monotonic. For TWM, we see a non-monotonic variation of Re_c with blockage for all Ar. St_c however, shows a monotonic increase with blockage for all the modes, for each Ar.

In order to determine the region important for control/suppression of the modes we first conduct structural sensitivity study and then linear stability analysis with small slip-plates placed at several locations on the centerline. We identify the peak in the overlap region of the direct and the adjoint modes as the location most suitable for effecting control. We conduct this study for $Re = 150$ flow past a circular cylinder and $Re = 180$ flow past an elliptic cylinder ($Ar = 0.25$). In both cases, we find a single peak in the overlap region of PWM and more than one peaks in the respective overlap regions for SWM and TWM. An interesting observation regarding the peak location was made from our study. For PWM, the peak location of the overlap region is closest to the location of the minimum of the base flow centerline velocity, for the Re, for which the growth rate is maximum. For other Re values, the peak location of the overlap region shifts away from the minimum velocity point. An explanation for the variation of the growth rate of PWM with Re is proposed based on this observation. However, similar trend was not seen for SWM and TWM.

The results from linear stability analysis of flow past a circular cylinder at Re $= 150$ with slip-plates provide us the information regarding the plates which would suppress either PWM or SWM, or both. For plate with $x_{LE} = 12.24$ and length $=$ 3.57, only PWM is suppressed ($\mathrm{PWM_{SP}}$) while plate with $x_{LE} = 16.03$ and length $=$ 1.75 suppresses only SWM ($\mathrm{SWM_{SP}}$). Unsteady flows ($\mathrm{PWM_{SP}}$ and $\mathrm{SWM_{SP}}$) with the initial condition taken as the steady flow superimposed with the corresponding unstable mode are computed. Thus, the initial evolution happens to be linear and the oscillation frequency obtained from the FFT of C_L versus time data agrees with the oscillation frequency of the mode. Subsequent evolution to the fully developed flow results in significant change in the oscillation frequency. The near wake of $\mathrm{SWM}_{\mathrm{SP}}$ oscillates with frequency 0.1829 which is same (up to four decimal places) as the frequency for flow without plate. For $\mathrm{PWM}_{\mathrm{SP}}$, the near wake frequency is 0.1795. Computation of the time averaged C_D, amplitude of the fluctuating components of C_D and C_L show that the values obtained for $\mathrm{SWM}_{\mathrm{SP}}$ are closer to the corresponding values for flow without plate. The vortex street structure and their extent in the wake, the frequency spectra of the cross-stream component of velocity at various locations in the wake and the decay rate (with respect to downstream distance) of the spectral amplitude, all, demonstrate the fact that, compared to $\mathrm{PWM}_{\mathrm{SP}}$, $\mathrm{SWM}_{\mathrm{SP}}$ better resembles flow past a cylinder without plate. We therefore conclude that if only PWM were present, flow would evolve into the same von Kármán vortex street which we get for flow without plate. On the other hand, if only SWM were present, the evolution would result in a slightly different fully developed flow.

A similar analysis for $Re = 180$ flow past an elliptic cylinder with $Ar = 0.25$ is conducted. Results from linear stability analysis with slip-plate of single element size show that for PWM, the minimum of the growth rate lies at $x_{LE} = 36.19$. For SWM, the growth rate curve has multiple minima which lie at $x_{LE} = 20.84$, 35.22, 44.39, 50.73 and 73.67. The growth rate versus plate location curve of TWM has several kinks/cross-over points and at the corresponding points in the St curve there are sudden jumps. This indicates that several modes which are stable become unstable on putting the plate. We therefore mark the modes as TWM_1, TWM_2, TWM_3 and TWM_4. The growth rate curve shows that TWM and TWM_1 are the same mode. Structural sensitivity analysis conducted for PWM, SWM and TWM cannot reveal the possibility of new modes becoming unstable. This is the advantage of the analysis with plates. The trend in the growth rate curve suggests the possibility of putting one or more slip-plates at appropriate locations on the centerline to suppress one or more of the PWM, SWM and TWM. After looking for several possibilities, we identify seven different choices regarding the locations and the corresponding lengths of the plates. Out of these, in three cases we find only one unstable mode. From our calculations it was not possible to determine the plate length and location for which TWM is the only unstable mode. We conduct unsteady computations for the case in which only PWM or only SWM is unstable. For obtaining SWM, we put six plates at appropriate locations on the centerline. The initial evolution of the perturbation happens to be linear and the oscillation frequency in the flow matches with the oscillation frequency of SWM (obtained by suppressing other modes). However, this is very different from the oscillation frequency of SWM obtained for flow past cylinder without plate. For the case when only PWM is unstable and other modes are suppressed, five plates are used. Here again, the linear evolution agrees with the characteristics of PWM obtained for flow with plate, not with the characteristics of PWM obtained for flow without plate. For this reason, the fully developed nonlinear flow obtained when only PWM is unstable is very different from the fully developed flow computed without plate. We therefore conclude that when the nonlinear effects are weak, i.e., when the oscillation amplitudes are small and shedding pattern is relatively simple, the fully developed flow characteristics could be linked to the features of the linear modes.

8.2 Scope for future work

The results presented in this thesis indicate several possible leads along which one can further extend the investigations. The literature available on steady flow past a circular cylinder (Fornberg [2], Gajjar & Ajjam [3], Mishra *et al.* [56]) and our experience with the present work on elliptic cylinders suggests that, at higher Re and very high blockage ratio, one may find more interesting flow behaviour with elliptic cylinders. For example, for flow past a circular cylinder, the bubble width shows nonlinear variation with Re up to Re = 300 and increases linearly thereafter (Fornberg [2]). At a very high blockage ratio = 0.9, the bubble length shows nonlinear variation with Re (Mishra *et al.* [56]). One may therefore expect unusual trends, of similar kind, to appear in flow past elliptic cylinders at high Re and high blockage ratios.

In linear stability results, we find that the critical Re for the unstable eigenmodes decreases with an increase in blockage. For Ar = 1.0, TWM remains stable up to Re = 200 and blockage ratio = 0.1. It is also observed that the growth rate and St of the eigenmodes show different trends at higher blockage. Therefore, one may extend this work beyond blockage ratio equal to 0.1 and expect to find new results regarding the stability properties of the eigenmodes in the wake of elliptic cylinders. One may also think of ways, other than those adopted in the present work, by which TWM could be isolated, i.e., using which only TWM grows and all other modes remain suppressed. We could then obtain the flow which develops due to the growth of only TWM.

References

[1] Sen S., Mittal S., and Biswas G. (2009) 'Steady separated flow past a circular cylinder at low Reynolds numbers', *J. Fluid Mech.*, vol. 620, pp. 89–119.

[2] Fornberg B. (1991) 'Steady incompressible flow past a row of circular cylinders', *J. Fluid Mech.*, vol. 225, pp. 655–671.

[3] Gajjar J.S.B. and Azzam N.A. (2004) 'Numerical solution of the Navier–Stokes equations for the flow in a cylinder cascade', *J. Fluid Mech.*, vol. 520, pp. 51–82.

[4] Thompson M.C., Radi A., Rao A., Sheridan J., and Hourigan K. (2014) 'Low-Reynolds-number wakes of elliptical cylinders: from the circular cylinder to the normal flat plate', *J. Fluid Mech.*, vol. 751, pp. 570–600.

[5] Sahin M. and Owens R.G. (2004) 'A numerical investigation of wall effects up to high blockage ratios on two-dimensional flow past a confined circular cylinder', *Phys. Fluids*, vol. 16, pp. 1305–1320.

[6] Mathis C., Provansal M., and Boyer L. (1984) 'The Bénard-von Kármán instability: an experimental study near the threshold', *J. Phys. Lett.*, vol. 45, pp. 483–491.

[7] Sreenivasan K.R., Strykowski P.J., and Olinger D.J., 'Hopf bifurcation, Landau equation, and vortex shedding behind circular cylinders', in 'Forum on unsteady flow separation', vol. 1 (ASME New York, 1987), pp. 1–13.

[8] Drazin P.G. and Reid W.H., *Hydrodynamic stability* (Cambridge university press, 2004).

[9] Schmid P.J. and Henningson D.S., *Stability and Transition in Shear Flows* (Springer, 2001).

[10] Monkewitz P.A. (1988) ‘The absolute and convective nature of instability in two-dimensional wakes at low Reynolds numbers’, *Phys. Fluids*, vol. 31, pp. 999–1006.

[11] Pier B. (2002) ‘On the frequency selection of finite-amplitude vortex shedding in the cylinder wake’, *J. Fluid Mech.*, vol. 458, pp. 407–417.

[12] Noack B.R. and Eckelmann H. (1994) ‘A global stability analysis of the steady and periodic cylinder wake’, *J. Fluid Mech.*, vol. 270, pp. 297–330.

[13] Theofilis V. (2011) ‘Global linear instability’, *Annu. Rev. Fluid Mech.*, vol. 43, pp. 319–352.

[14] Giannetti F. and Luchini P. (2007) ‘Structural sensitivity of the first instability of the cylinder wake’, *J. Fluid Mech.*, vol. 581, pp. 167–197.

[15] Marquet O., Sipp D., and Jacquin L. (2008) ‘Sensitivity analysis and passive control of cylinder flow’, *J. Fluid Mech.*, vol. 615, pp. 221–252.

[16] Choi H., Jeon W.P., and Kim J. (2008) ‘Control of flow over a bluff body’, *Annu. Rev. Fluid Mech.*, vol. 40, pp. 113–139.

[17] Strykowski P.J. and Sreenivasan K.R. (1990) ‘On the formation and suppression of vortex ‘shedding’at low Reynolds numbers’, *J. Fluid Mech.*, vol. 218, pp. 71–107.

[18] Taneda S. (1956) ‘Experimental investigation of the wakes behind cylinders and plates at low Reynolds numbers’, *J. Phys. Soc. Jpn*, vol. 11, pp. 302–307.

[19] Gerrard J. (1966) ‘The mechanics of the formation region of vortices behind bluff bodies’, *J. Fluid Mech.*, vol. 25(02), pp. 401–413.

[20] Coutanceau M. and Bouard R. (1977) ‘Experimental determination of the main features of the viscous flow in the wake of a circular cylinder in uniform translation. part 1. steady flow’, *J. Fluid Mech.*, vol. 79, pp. 231–256.

[21] Williamson C.H.K. (1996) ‘Vortex dynamics in the cylinder wake’, *Annu. Rev. Fluid Mech*, vol. 28, pp. 477–539.

[22] Zdravkovich M.M. (1997) ‘Flow around circular cylinders; vol. i fundamentals’, *J. Fluid Mech.*, vol. 350, pp. 377–378.

[23] Jain P.C. and Rao K.S. (1969) ‘Numerical solution of unsteady viscous incompressible fluid flow past a circular cylinder’, *Phys. Fluids*, vol. 12(12), pp. II–57.

[24] Dennis S.C.R. and Chang G.Z. (1970) ‘Numerical solutions for steady flow past a circular cylinder at Reynolds numbers up to 100’, *J. Fluid Mech.*, vol. 42(03), pp. 471–489.

[25] Fornberg B. (1980) ‘A numerical study of steady viscous flow past a circular cylinder’, *J. Fluid Mech.*, vol. 98, pp. 819–855.

[26] Dennis S.C.R. and Chang G.Z. (1969) ‘Numerical integration of the Navier-Stokes equations for steady two-dimensional flow’, *Phys. Fluids*, vol. 12(12), pp. II–88.

[27] D’Alessio S.J.D. and Dennis S.C.R. (1994) ‘A vorticity model for viscous flow past a cylinder’, *Comput. Fluids*, vol. 23, pp. 279–293.

[28] Dennis S.C.R. and Young P.J.S. (2003) ‘Steady flow past an elliptic cylinder inclined to the stream’, *J. Eng. Math.*, vol. 47, pp. 101–120.

[29] Faruquee Z., Ting D.S.K., Fartaj A., Barron R.M., and Carriveau R. (2007) ‘The effects of axis ratio on laminar fluid flow around an elliptical cylinder’, *Int. J. Heat Fluid Flow*, vol. 28, pp. 1178–1189.

[30] Sivakumar P., Bharti R.P., and Chhabra R.P. (2007) ‘Steady flow of power-law fluids across an unconfined elliptical cylinder’, *Chem. Eng. Sci.*, vol. 62, pp. 1682–1702.

[31] Sen S., Mittal S., and Biswas G. (2011) ‘Flow past a square cylinder at low Reynolds numbers’, *Int. J. Numer. Methods Fluids*, vol. 67, pp. 1160–1174.

[32] Sen S., Mittal S., and Biswas G. (2012) ‘Steady separated flow past elliptic cylinders using a stabilized finite-element method’, *Comput. Model Eng. Sci.*, vol. 86, pp. 1–27.

[33] Paul I., Prakash K.A., and Vengadesan S. (2014) ‘Onset of laminar separation and vortex shedding in flow past unconfined elliptic cylinders’, *Phys. Fluids*, vol. 26, p. 023601.

[34] Sen S. (2020) ‘Surface pressure and viscous forces on inclined elliptic cylinders in steady flow’, *Sādhanā*, vol. 45(1), pp. 1–18.

[35] Tomotika S. and Aoi T. (1953) ‘The steady flow of a viscous fluid past an elliptic cylinder and a flat plate at small Reynolds numbers’, *Q. J. Mech. Appl. Math.*, vol. 6, pp. 290–312.

[36] Yamada H. (1954) ‘On the slow motion of viscous liquid past a circular cylinder’, *Rep. Res. Inst. Appl. Mech. Kyushu Univ*, vol. 3, pp. 11–23.

[37] Underwood R.L. (1969) ‘Calculation of incompressible flow past a circular cylinder at moderate Reynolds numbers’, *J. Fluid Mech.*, vol. 37, pp. 95–114.

[38] Smith F. (1979) ‘Laminar flow of an incompressible fluid past a bluff body: the separation, reattachment, eddy properties and drag’, *J. Fluid Mech.*, vol. 92(1), pp. 171–205.

[39] Chernyshenko S.I. (1988) ‘The asymptotic form of the stationary separated circumfluence of a body at high Reynolds numbers’, *J. Appl. Math. Mech.*, vol. 52(6), pp. 746–753.

[40] Chernyshenko S.I. and Castro I.P. (1993) ‘High-Reynolds-number asymptotics of the steady flow through a row of bluff bodies’, *J. Fluid Mech.*, vol. 257, pp. 421–449.

[41] Chernyshenko S. (1998) ‘Asymptotic theory of global separation’, *Appl. Mech. Rev.*, vol. 51, pp. 523–535.

[42] Hasimoto H. (1953) ‘On the flow of a viscous fluid past an inclined elliptic cylinder at small Reynolds numbers’, *J. Phys. Soc. Jpn.*, vol. 8, pp. 653–661.

[43] Imai I. (1954) ‘A new method of solving Oseen’s equations and its application to the flow past an inclined elliptic cylinder’, *Proc. R. Soc. London, Ser. A*, vol. 224, pp. 141–160.

[44] Takaisi Y. (1958) ‘The wall-effect upon the forces experienced by an elliptic cylinder in a viscous liquid.’, *J. Phys. Soc. Jpn.*, vol. 13(5), pp. 496–506.

[45] Tamada K.O., Miura H., and Miyagi T. (1983) ‘Low-Reynolds-number flow past a cylindrical body’, *J. Fluid Mech.*, vol. 132, pp. 445–455.

[46] Shintani K., Umemura A., and Takano A. (1983) 'Low-Reynolds-number flow past an elliptic cylinder', *J. Fluid Mech.*, vol. 136, pp. 277–289.

[47] Fornberg B. and Elcrat A.R. (2014) 'Some observations regarding steady laminar flows past bluff bodies', *Philos. Trans. R. Soc., Math. Phys. Eng. Sci.*, vol. 372, p. 20130353.

[48] Fornberg B. (1985) 'Steady viscous flow past a circular cylinder up to Reynolds number 600', *J. Comput. Phys.*, vol. 61, pp. 297–320.

[49] Smith F.T. (1985) 'A structure for laminar flow past a bluff body at high Reynolds number', *J. Fluid Mech.*, vol. 155, pp. 175–191.

[50] Peregrine D.H. (1985) 'A note on the steady high-Reynolds-number flow about a circular cylinder', *J. Fluid Mech.*, vol. 157, pp. 493–500.

[51] Yoon H.S., Yin J., Choi C., Balachandar S., and Ha M.Y. (2016) 'Bifurcation of laminar flow around an elliptic cylinder at incidence for low Reynolds numbers', *Prog. Comput. Fluid Dyn.*, vol. 16, pp. 163–178.

[52] Shi X., Alam M., and Bai H. (2020) 'Wakes of elliptical cylinders at low Reynolds number', *Int. J. Heat Fluid Flow*, vol. 82, p. 108553.

[53] Kumar D. and Sahu A.K. (2022) 'Non-Newtonian fluid flow over a rotating elliptic cylinder in laminar flow regime', *Eur. J. Mech. B*, vol. 93, pp. 117–136.

[54] Anagnostopoulos P., Iliadis G., and Richardson S. (1996) 'Numerical study of the blockage effects on viscous flow past a circular cylinder', *Int. J. Numer. Methods Fluids*, vol. 22, pp. 1061–1074.

[55] Singha S. and Sinhamahapatra K.P. (2010) 'Flow past a circular cylinder between parallel walls at low Reynolds numbers', *Ocean Eng.*, vol. 37, pp. 757–769.

[56] Mishra S.K., Sen S., and Verma A. (2021) 'Steady flow past a circular cylinder under large blockage', *Eur. J. Mech. B:Fluids*, vol. 87, pp. 135–150.

[57] Jackson C.P. (1987) 'A finite-element study of the onset of vortex shedding in flow past variously shaped bodies', *J. Fluid Mech.*, vol. 182, pp. 23–45.

[58] Zebib A. (1987) 'Stability of viscous flow past a circular cylinder', *J. Eng. Math.*, vol. 21, pp. 155–165.

[59] Morzyński M., Afanasiev K., and Thiele F. (1999) ‘Solution of the eigenvalue problems resulting from global non-parallel flow stability analysis’, *Comput. Methods Appl. Mech. Eng.*, vol. 169, pp. 161–176.

[60] Barkley D. and Henderson R.D. (1996) ‘Three-dimensional floquet stability analysis of the wake of a circular cylinder’, *J. Fluid Mech.*, vol. 322, pp. 215–241.

[61] Boppana V.B.L. and Gajjar J.S.B. (2011) ‘Onset of global instability in the flow past a circular cylinder cascade’, *J. Fluid Mech.*, vol. 668, pp. 304–334.

[62] Verma A. and Mittal S. (2011) ‘A new unstable mode in the wake of a circular cylinder’, *Phys. Fluids*, vol. 23, p. 121701.

[63] Chen J.H., Pritchard W.G., and Tavener S.J. (1995) ‘Bifurcation for flow past a cylinder between parallel planes’, *J. Fluid Mech.*, vol. 284, pp. 23–41.

[64] Kumar B. and Mittal S. (2006) ‘Effect of blockage on critical parameters for flow past a circular cylinder’, *Intl J. Numer. Methods Fluids*, vol. 50, pp. 987–1001.

[65] Mittal S. and Kumar B. (2003) ‘Flow past a rotating cylinder’, *J. Fluid Mech.*, vol. 476, pp. 303–334.

[66] Kumar B. and Mittal S. (2006) ‘Prediction of the critical Reynolds number for flow past a circular cylinder’, *Comput. Methods Appl. Mech. Eng.*, vol. 195, pp. 6046–6058.

[67] Mittal S. and Raghuvanshi A. (2001) ‘Control of vortex shedding behind circular cylinder for flows at low Reynolds numbers’, *Intl. J. Numer. Meth. Fluids*, vol. 35, pp. 421–447.

[68] Roshko A. (1955) ‘On the wake and drag of bluff bodies’, *J. Aero. Sci.*, vol. 22, pp. 124–132.

[69] Lin S.Y. and Wu T.M. (1994) ‘Flow control simulations around a circular cylinder by a finite volume scheme’, *Numer. Heat Transfer, Part A*, vol. 26, pp. 301–319.

[70] Ozono S. (1999) ‘Flow control of vortex shedding by a short splitter plate asymmetrically arranged downstream of a cylinder’, *Phys. Fluids*, vol. 11, pp. 2928–2934.

[71] Mittal S. (2003) ‘Effect of a ’slip’ splitter plate on vortex shedding from a cylinder’, *Phys. Fluids*, vol. 15, pp. 817–820.

[72] Serson D., Meneghini J.R., Carmo B.S., Volpe E.V., and Gioria R.S. (2014) ‘Wake transition in the flow around a circular cylinder with a splitter plate’, *J. Fluid Mech.*, vol. 755, pp. 582–602.

[73] Soumya S. and Prakash K.A. (2017) ‘Effect of splitter plate on passive control and drag reduction for fluid flow past an elliptic cylinder’, *Ocean Eng.*, vol. 141, pp. 351–374.

[74] Chomaz J.M. (2005) ‘Global instabilities in spatially developing flows: non-normality and nonlinearity’, *Annu. Rev. Fluid Mech.*, vol. 37, pp. 357–392.

[75] Kumar B. and Mittal S. (2012) ‘On the origin of the secondary vortex street’, *J. Fluid Mech.*, vol. 711, pp. 641–666.

[76] Hughes T.J.R. and Brooks A.N., ‘A multidimensional upwind scheme with no crosswind diffusion’, in T.J.R. Hughes, (Editor) ‘Finite Element Methods for Convection Dominated Flows’, (ASME, 1979), pp. 19–35.

[77] Brooks A.N. and Hughes T.J.R. (1982) ‘Streamline upwind/Petrov-Galerkin formulations for convection dominated flows with particular emphasis on the incompressible Navier-Stokes equations’, *Comput. Methods Appl. Mech. Eng.*, vol. 32, pp. 199–259.

[78] Tezduyar T.E., Mittal S., Ray S.E., and Shih R. (1992) ‘Incompressible flow computations with stabilized bilinear and linear equal-order-interpolation velocity-pressure elements’, *Comput. Methods Appl. Mech. Eng.*, vol. 95, pp. 221–242.

[79] Mittal S. (2000) ‘On the performance of high aspect ratio elements for incompressible flows’, *Comput. Methods Appl. Mech. Eng.*, vol. 188, pp. 269–287.

[80] Hughes T.J.R., Franca L.P., and Balestra M. (1986) ‘A new finite element formulation for computational fluid dynamics: V. circumventing the Babuška-Brezzi condition: a stable Petrov-Galerkin formulation of the Stokes problem accommodating equal-order interpolations’, *Comput. Methods Appl. Mech. Eng.*, vol. 59, pp. 85–99.

[81] Mittal S., Kottaram J.J., and Kumar B. (2008) 'Onset of shear layer instability in flow past a cylinder', *Phys. Fluids*, vol. 20, p. 054102.

[82] Mittal S. (2008) 'Global linear stability analysis of time-averaged flows', *Intl. J. Numer. Meth. Fluids*, vol. 58, pp. 111–118.

[83] Mittal S. (2008) 'Linear stability analysis of time-averaged flow past a cylinder', *Comput. Model. Eng. Sci.*, vol. 27, pp. 63–78.

[84] Kumar B., Kottaram J.J., Singh A.K., and Mittal S. (2009) 'Global stability of flow past a cylinder with centreline symmetry', *J. Fluid Mech.*, vol. 632, pp. 273–300.

[85] Mittal S. (2009) 'Onset of mixing layer instability in flow past a plate', *Intl J. Numer. Meth. Fluids*, vol. 59, pp. 1035–1049.

[86] Mittal S. and Kumar B. (2007) 'A stabilized finite element method for global analysis of convective instabilities in nonparallel flows', *Phys. Fluids*, vol. 19, p. 088105.

[87] Stewart G.W. and Miller J.H., 'Methods of simultaneous iteration for calculating eigenvectors of matrices', in J.H.H. Miller, (Editor) 'Topics in Numerical Analysis II', (Academic, 1975), pp. 169–185.

[88] Erturk E. and Gokcol O. (2018) 'Numerical solutions of steady incompressible flow around a circular cylinder up to Reynolds number 500', *Int. J. Mech. Eng.*, vol. 9(10), pp. 1368–1378.

[89] Son J.S. and Hanratty T.J. (1969) 'Numerical solution for the flow around a cylinder at Reynolds numbers of 40, 200 and 500', *J. Fluid Mech.*, vol. 35(2), pp. 369–386.

[90] Collins W. and Dennis S. (1973) 'Flow past an impulsively started circular cylinder', *J. Fluid Mech.*, vol. 60(01), pp. 105–127.

[91] Patel V.A. (1976) 'Time-dependent solutions of the viscous incompressible flow past a circular cylinder by the method of series truncation', *Comput. Fluids*, vol. 4(1), pp. 13–27.

[92] Srinivasan K. (2005) ‘On a separation criterion for symmetric elliptic bluff body flows’, *arXiv preprint physics/0511250*.

[93] Wu M.H., Wen C.Y., Yen R.H., Weng M.C., and Wang A.B. (2004) ‘Experimental and numerical study of the separation angle for flow around a circular cylinder at low Reynolds number’, *J. Fluid Mech.*, vol. 515, pp. 233–260.

[94] Johnson S.A., Thompson M.C., and Hourigan K., ‘Flow past elliptical cylinders at low Reynolds numbers’, in ‘Proceedings of 14th Australian Fluid Mechanics Conference, Adelaide’, (2001), pp. 343–346.

[95] Barkley D. (2006) ‘Linear analysis of the cylinder wake mean flow’, *Europhys. Lett.*, vol. 75, p. 750.

[96] Zhang H.Q., Fey U., Noack B.R., König M., and Eckelmann H. (1995) ‘On the transition of the cylinder wake’, *Phys. Fluids*, vol. 7, pp. 779–794.

[97] Liu C., Zheng X., and Sung C.H. (1998) ‘Preconditioned multigrid methods for unsteady incompressible flows’, *J. Comput. Phys.*, vol. 139, pp. 35–57.

Indian Institute of Technology Guwahati